Extensive longevity and DNA virus-driven adaptation in nearctic *Myotis* bats

Juan M Vazquez[1,18], M. Elise Lauterbur[2,3,18], Saba Mottaghinia[4], Melanie Bucci[2], Devaughn Fraser[5,6], Genavieve Gray-Sandoval[2], Léa Gaucherand[7], Zeinab R Haidar[8,9], Melissa Han[10], William Kohler[10], Tanya M. Lama[11], Amandine Le Corf[4], Clara Loyer[4], Sarah Maesen[4], Dakota McMillan[1,12], Stacy Li[1,13], Johnathan Lo[13], Carine Rey[4], Samantha LR Capel[6], Michael Singer[14], Kathleen Slocum[15], William Thomas[16], Janet Debelak Tyburec[17], Sarah Villa[14], Richard Miller[10], Michael Buchalski[5], Jose Pablo Vazquez-Medina[1], Sébastien Pfeffer[7], Lucie Etienne[4,19]*, David Enard[2,19,20]**, Peter H Sudmant[1,13,19,20,21]***

Affiliations:

1. Department of Integrative Biology, University of California, Berkeley, Berkeley, CA USA
2. Department of Ecology and Evolutionary Biology, University of Arizona, Tucson, AZ USA
3. Current affiliation: Department of Biology, University of Vermont, Burlington, VT USA
4. Centre International de Recherche en Infectiologie (CIRI), Inserm U1111, UCBL1, CNRS UMR5308, Ecole Normale Supérieure ENS de Lyon, Université de Lyon, Lyon, France
5. Wildlife Genetics Research Unit, Wildlife Health Laboratory, California Department of Fish and Wildlife, Sacramento, CA, United States
6. Current affiliation: Wildlife Diversity Program, Wildlife Division, Connecticut Department of Energy and Environmental Protection, Burlington, CT, United States
7. Université de Strasbourg, Architecture et Réactivité de l'ARN, Institut de Biologie Moléculaire et Cellulaire du CNRS, Strasbourg, France.
8. Department of Biology, California State Polytechnic University, Humboldt, Arcata, CA USA
9. Current affiliation: Western EcoSystems Technology Inc, Cheyenne, WY USA
10. Department of Pathology and Clinical Laboratories, University of Michigan, Ann Arbor, MI USA
11. Department of Biological Sciences, Smith College, Northampton, MA USA
12. Department of Science and Biotechnology, Berkeley City College, Berkeley, CA USA
13. Center for Computational Biology, University of California, Berkeley, Berkeley, CA USA
14. Department of Molecular and Cellular Biology, University of California, Berkeley, Berkeley, CA USA
15. Bat Conservation International, Austin, TX USA
16. Department of Ecology and Evolution, Stony Brook University, Stony Brook NY USA
17. Bat Survey Solutions, LLC, Tucson, AZ USA
18. These authors contributed equally
19. Senior author
20. These authors contributed equally
21. Lead contact

* Correspondence: lucie.etienne@ens-lyon.fr

** Correspondence: denard@arizona.edu
*** Correspondence: psudmant@berkeley.edu

Abstract

The genus *Myotis* is one of the largest clades of bats, and exhibits some of the most extreme variation in lifespans among mammals alongside unique adaptations to viral tolerance and immune defense. To study the evolution of longevity-associated traits and infectious disease, we generated near-complete genome assemblies and cell lines for 8 closely related species of *Myotis*. Using genome-wide screens of positive selection, analyses of structural variation, and functional experiments in primary cell lines, we identify new patterns of adaptation contributing to longevity, cancer resistance, and viral interactions in bats. We find that *Myotis* bats have some of the most significant variation in cancer risk across mammals and demonstrate a unique DNA damage response in primary cells of the long-lived *M. lucifugus*. We also find evidence of abundant adaptation in response to DNA viruses - but not RNA viruses - in *Myotis* and other bats in sharp contrast with other mammals, potentially contributing to the role of bats as reservoirs of zoonoses. Together, our results demonstrate how genomics and primary cells derived from diverse taxa uncover the molecular bases of extreme adaptations in non-model organisms.

Keywords

Aging, Bats, Cancer, Evolutionary Biology, Functional Genomics, Immunity, Infectious Disease

Introduction

Bats (order *Chiroptera*) represent approximately 20% of all known mammalian species and are one of the most phenotypically diverse clades of mammals[1,2]. Since their emergence 60 million years ago[3–5], many bat lineages have independently evolved a wide variety of life history strategies and phenotypic traits, including exceptional changes in longevity, viral tolerance, and immune defense[6–11]. Such systems, in which shared traits have evolved *de novo* multiple times, are powerful resources for dissecting the genetic basis of phenotypes. Rigorous approaches to studying these traits, however, depend on high-quality, well-annotated genomes to test evolutionary and genomic hypotheses, and on experimental functional systems to validate these hypotheses.

The largest genus of bats - *Myotis* - is estimated to have emerged approximately 33 million years ago[12,13], and encompasses over 139 described species spanning six continents and a wide range of ecological niches[1,12–14]. *Myotis* species demonstrate some of the most extreme variation in lifespan amongst mammals[6,15–18], including a six-fold difference in lifespan between the longest-lived species (*M. brandtii*, 42 years[15,19], **Figure 1A**) and the shortest-lived species (*M. nigricans*, 7 yrs[15,20]) which diverged approximately 10.6 million years ago[5,14,21,22]. In addition, *Myotis* species have been used as systems for investigating virus tolerance and other pathogen resistance[23–25] associated with the expansion and

contraction of antiviral defenses[26–29], which have contributed to bats' ecological role as zoonotic reservoirs[10,11,30–33].

The origin, evolution, and functional basis of these phenotypes can be studied experimentally in model organisms as well as via comparative evolutionary methods. The power of comparative evolutionary studies is constrained by several factors including incomplete phylogenetic coverage; poor temporal resolution; the quality and composition of gene annotations; and availability of functional data and tools for validation. Rapidly evolving genes, such as those associated with adaptations to pathogens [34–36], present particular challenges for homology and alignment based methods. Similarly, poor phenotypic resolution and long divergence times between study species hinders the power of statistical approaches to identify patterns of selection and diversification[37–40]. Meanwhile, model organism-based approaches contribute a different, complementary perspective and provide the power of functional analyses; however, these studies can suffer from issues related to the suitability and diversity of the model species' genotype and phenotype.

While studies on the genetic basis of longevity in short-lived model organisms have been crucial for identifying and dissecting several key aging pathways, comparative studies of exceptionally long-lived organisms have uncovered novel genes and pleiotropic effects governing lifespan[36,41–53]. The comparative approach, however, has historically been hindered by limitations in available genomic resources and genetic tools for study. Similarly, studies of infectious disease response are common and powerful in model organisms, but the lack of diversity and inbred lines limits their scope. Bats in particular present an important case study in, and opportunity to study, variation in virus adaptation strategies due to bats' role as zoonotic reservoirs and their specific resistance to viruses[36,54]. While previous studies have shown unique infectious disease adaptations in bats, including loss of important inflammatory genes and expansions of and adaptation in some immune gene families[54–56], they are typically hampered by the breadth and number of species analyzed, and only rarely functionally validate results from genomic analyses.

Here we combined comparative and functional approaches in *Myotis* to uncover strong genomic and functional evidence of adaptation to both aging-related and infectious diseases. We present for the first time a robust quantification of relative intrinsic cancer risk across mammals, finding that *Myotis* are overrepresented at the extreme of increased cancer risk. Consistent with this observation, we identified pervasive selection of genes in longevity- and cancer-related processes, especially in lineages which have undergone the greatest changes in lifespan. Furthermore, we found strong evidence of adaptation in response to DNA viruses in Myotis and other bats. Genome-wide enrichment of adaptation being driven by DNA viruses is unique to bats in comparison with other large groups of mammals. Finally, using near-complete assemblies, we identified structural variations encompassing stress response, immunity, and inflammation genes, including a trans-species copy number polymorphism of protein kinase R (PKR). Together, our results suggest that pleiotropy and co-evolution of traits in *Myotis* has played a key role in the evolution of exceptional longevity and infectious disease resistance.

Results

High quality chromosome-level assemblies of 8 *Myotis* bat species

To study how lifespan and viral response have evolved in *Myotis*, we collected skin punches and derived primary cell lines from several North American ("Nearctic")[21] species (**Figure 1A,C),** including from one of the longest-lived mammals, *Myotis lucifugus*[15]. Using these cell lines and flash frozen tissues we generated *de novo* haplotype-resolved, chromosome-scale genome assemblies for eight species (**Figure 1A**) using a combination of long-read PacBio HiFi sequencing and HiC scaffolding. These genomes are highly contiguous, with an average of 98.6% of nucleotides assembled into 22-23 syntenic chromosome-scale scaffolds corresponding to the published karyotype[57] with an average QV of 66. These genomes have among the lowest auNG scores of any *Chiroptera* genome published to date (**Figure 1A, E**; **Table S1**). Across all 8 genomes, each autosome has been completely assembled telomere-to-telomere (T2T) in at least one species (**Figure 1E**). Within assemblies, 29%-70% of chromosomes are fully assembled with an average of less than one gap per chromosome (**Table S1**). When comparing the assemblies of species generated from tissue samples versus primary cell lines, we found that they were broadly comparable and structurally similar. However, genomes assembled from cell lines had slightly improved statistics likely attributable to the increased quality and molecular weight of extracted DNA (**Figure 1A, D, E; Table S1**).

Genomes were annotated using well-established pipelines[36] leveraging multiple lines of evidence, including short-read RNAseq, gene prediction (AUGUSTUS-CGP[58], GeneMark-ES[59]; gene projections[60], TOGA[61]); and homology (miniprot[62]). In total, we identified an average of 27,536 protein coding genes per species. We benchmarked our annotations using BUSCO[63,64] (V5.4.3) mammalian ortholog sets indicating these annotations are 98.2%-98.5% complete (**Figure 1C**). We also annotated a recent assembly of *Myotis yumanensis*[65] for inclusion in downstream analyses. Overall, these fully annotated genomes represent some of the most contiguous mammalian assemblies to date.

Resolving the phylogeny and the evolution of body size and lifespan in nearctic *Myotis*

The phylogenetic relationships within *Myotis* have been the subject of much debate, with a number of conflicting phylogenies described in the literature based on different choices of genetic markers[14,66–69]. To resolve the phylogeny of Nearctic *Myotis*, we identified single copy orthologs of 17,509 protein genes present in 536 mammalian genomes resulting in 30.6M aligned nucleotides. These alignments were used to build a maximum likelihood tree of *Eutheria*. The *Chiroptera* sub-clade was then time-calibrated using available fossil-based node calibrations (**Figure 1B**; **Figure S1**; **Table S2**). Our results conclusively recapitulate known sister species pairs including *M. lucifugus* and *M. occultus*; *M. yumansis and M. velifer*; and *M. evotis* and *M. thysanodes*. Our proposed phylogeny resolves the complex relationship between these sister taxa, with 100% bootstrap support at all nodes throughout *Chiroptera*.

Using our resolved Nearctic *Myotis* phylogeny, we re-examined the evolution of body size and lifespan in *Chiroptera*. In mammals and other metazoans, there is a strong allometric scaling (positive correlation with body size) of lifespan. Bats have been noted as an exception to this rule: they are exceptionally long-lived for their body size[17,18,70], and this exceptional longevity has evolved *de novo* multiple times[6,70,71]. However, these observations have not been tested using phylogenetically corrected statistics leveraging well-resolved phylogenies. To test the hypothesis of non-allometric scaling of lifespan in bats, we modeled the evolution of body size and lifespan across a supertree of over 1000 placental mammals (*Eutheria*)[67] (**Figure 2**; **Table S2**). In agreement with previous studies in vertebrates[7,17,44,50,72–80], changes in body size are pervasive across mammals, with extreme changes seen in whales (*Cetacea*)[78,79], elephantids (*Proboscidea*)[42,44,72], and in sloths and armadillos (*Xenarthra*)[73,80–82] (**Figure 2A**; **Table S2**). Within bats, major changes in body size are only observed at the root of the lineage and within *Yinpterochrioptera* (megabats including genera *Pteropus, Eidolon, Megaderma,* and *Rhinolophus*). Outside of these clades, only minor changes in body size were observed (**Figure 2A**). The evolution of lifespan across mammals mirrors the evolution of body size; branches with large increases in body size (e.g. *Cetacea* ancestor, *Primate* ancestor) have also experienced large increases in lifespan (**Figure 2B)**, leading to an overall positive association between lifespan and body size (**Figure S2A**). However, despite little change in body size in bats (**Figure 2A, C**), we observed some of the largest changes in lifespan across mammals towards the tips of the tree (**Figure 2B, D**), consistent with the theory of multiple independent increases in lifespan across bats. This is especially true in *Myotis*, where we saw many of the fastest increases in lifespan, including for *Myotis grisescens* (4.15x increase, 100th percentile), *Myotis brandtii* (2.25x increase, 100th percentile), *Myotis lucifugus* (1.56x, 98th percentile), *Myotis myotis* (1.1x increase, 79nd percentile), and the *Myotis* common ancestor (1.26x increase, 92rd percentile) (**Figure 2D; Figure S2C; Table S2**). We next used phylogenetically-corrected generalized linear models and ANCOVA to study the relationship between body size and lifespan across mammals. While we find that non-bat mammals experience a 0.159% increase in lifespan per 1% increase in body size on average, bats experience a 0.223% increase in lifespan years per 1% increase in body size; these rates were not significantly different, however, suggesting that lifespan allometry is conserved in bats after accounting for phylogeny (**Figure S2E-F**; pANCOVA, p=0.29).

Rapid changes in body size and lifespan can have major implications for the evolution of cancer risk and resistance across mammals. The lifetime cancer risk of an individual is modeled as the product of body size (i.e. the number of cells within an individual), lifespan, and a constant representing the intrinsic cancer risk per cell per unit time. Within species, lifetime cancer risk scales linearly with body size, and with lifespan by a power-law of exponent 6[83–86]. In contrast to this *within*-species relationship, there is no significant correlation between body size, lifespan, and cancer risk *across* species[86–89] - a phenomenon known as Peto's Paradox. The observation of similar lifetime cancer incidence rates across mammals[73,89,90] suggests that species with more cells or longer lifespans have adapted to reduce their cancer risks (i.e. increased cancer resistance) (**Figure 2E**).

We hypothesized that the very rapid evolution of increased lifespan in *Myotis* would thus result in a dramatic increase in their expected cancer risk compared to other mammals. This can be quantified by the Reduced Intrinsic Cancer Risk per cell (RICR) between an extant mammal and its most recent ancestor, calculated as the $\log_2$ ratio of body size and lifespan between the two nodes (**Figure 2E**)[44,86]. Decreases in RICR correspond to an increase in the expected cancer risk. We used estimates of body size and lifespan across *Eutheria* to quantify changes in (RICR) across placental mammals (**Figure 2F**)[44].

188 Bats overall were slightly overrepresented in the bottom 10% of RICR with an odds ratio of 1.15,
189 highlighting the impact of rapid lifespan evolution on cancer risk. The longest-lived *Myotis* (*M. grisescens*,
190 39 yrs & 1st pct; *M. brandtii*, 42 yrs & 2nd percentile; *M. lucifugus*, 36 yrs & 4th pct) and their most recent
191 common ancestors (*lucifugus-occultus*, ~26 yrs & 8th pct; *Myotis* common ancestor, ~22 yrs & 14th pct)
192 demonstrated some of the most pronounced decreases in RICR among mammals (**Figure 2F; Figure**
193 **S2D; Table S2**). Similar to other extreme cases of body size and lifespan in vertebrates[44,46,50,52,73,91–94],
194 the pronounced changes in RICR seen in *Myotis* imply an extraordinarily strong selective pressure to
195 evolve cancer resistance mechanisms at multiple points across *Chiroptera* in general, and within *Myotis*
196 in particular.

197 Evolutionary signatures of cancer resistance in *Myotis*

198 We next set out to identify genes under positive selection across our phylogeny of Nearctic *Myotis*.
199 We used aBSREL[95] to test for branch-specific positive selection among 15,734 single-copy orthologous
200 genes identified in 536 mammalian genomes. We found that on average, 22.7% of genes were under
201 selection across the 9 nearctic *Myotis* species and their internal branches after multiple testing correction
202 at FDR<=5%; and 5.23% of genes were significant and had omega values above 1, signaling positive
203 selection (**Table S3**). These genes were enriched for several pathways involved in immunity, cancer, and
204 aging (**Table S3**). Many of these genes lie at the intersection of these two processes, including members
205 of the Cluster of Differentiation (CD) family, Serpin family, insulin signaling pathway, redox repair, and
206 iron storage (**Figure 3A; Table S3**), suggesting possible pleiotropic influences on genes under selection.

207 To test this, we quantified the contribution of genes under selection to pathways associated with
208 the hallmark of cancer[96–98] by measuring the proportion of cancer-associated pathways overrepresented
209 among genes under selection throughout the phylogeny (**Figure 3A; insets**). Many nodes within nearctic
210 *Myotis* were enriched for cancer hallmark pathways, especially at the recent ancestors of the longest-
211 lived species (e.g. *M. lucifugus, M. occultus*; **Figure 3A**). Testing the overall contribution of genes that
212 have undergone selection in each species since the common *Myotis* ancestor, we observed significant
213 enrichments in the representation of cancer-associated pathways only in species lineages with reductions
214 in RICR (*M. lucifugus*, *M. occultus, M. evotis, M. thysanodes, M. yumanensis;* **Figure 3B**). This suggests
215 that while genes under selection in nearctic *Myotis* frequently contribute to cancer-associated pathways,
216 cancer resistance has only driven consistent selection in the longest-lived lineages with the greatest
217 increases in cancer risk.

218 We also observed that many key genes involved in ferroptosis - specifically in iron transport,
219 glutathione metabolism, and lipid peroxidation - were under both positive and negative selection at
220 multiple instances throughout the phylogeny (**Table S3**). Many of these genes were recurrently under
221 selection in each species' lineage, such as with ferritin (both heavy and light chains) at three distinct
222 points in the evolutionary history of *M. yumanensis*. Genes under selection in iron transport are
223 specifically involved in the regulation of free iron in the cell, specifically in the export and reduction of the
224 free radical catalyst Fe^{2+} (ferroportin, *HMOX1*) and the import, storage, and maintenance of Fe^{3+} (ferritin
225 and transferrin receptors 1 and 2). Additionally, we observe selective signatures in glutathione
226 metabolism and oxidative stress response including: *SLC3A2* and *SLC7A11*, a heterodimer pair
227 facilitating cystine import and glutamate export; glutathione synthetase; and glutathione peroxidase 3

228 (*GPX3*). Finally, we observed a pattern of selection in genes involved in synthesizing and maintaining
229 key polyunsaturated fatty acids involved in ferroptosis, including *LPCAT3*, *ALOX15*, and *PRDX5*.

230 To test for intensified and relaxed selection in genes in long-lived or short-lived *Myotis*, we ran
231 RELAX[99] on 12,438 genes present across 11 *Myotis* species, identifying 263 genes under intensified
232 selection (k>1) and 101 genes under relaxed selection (k≤1) after multiple testing correction (p_{adj}≤0.05).
233 Among genes of note showing significant intensified selection were *USP9X* (an X-linked ubiquitin
234 protease associated with cancer and T cell development[100,101], k=48.6); *CDK16* (an oncogenic cyclin-
235 dependent kinase that regulates autophagy[102,103], k=44.9); and *FGFR2* (a cell growth receptor associated
236 with human cancers that is also a viral interacting protein[104,105], k=26.1) (**Figure S3B; Table S4)**.
237 Performing a gene set enrichment analysis for the 364 significant genes, we find a strong association
238 among genes under intensified selection with FGF2 signaling, chromatin remodeling, and pathways
239 associated with both retroviruses and coronaviruses (**Figure S3C; Table S4**). Finally, using
240 RERConverge[106], we investigated how genes' evolutionary rates correlated with the evolution of body
241 size, lifespan, or the first two principal components of body size and lifespan across *Myotis*, and found a
242 number of genes enriched in pathways associated with innate immunity, gamete production, and various
243 metabolic processes, consistent with our other results (**Figure S3D-E; Table S4**).

244 The longest-lived bat in our study, *M. lucifugus*, had an overrepresentation of pathways
245 specifically associated with DNA double-strand break (DSB) repair when looking at both lineage-wide
246 and node-specific enrichments in positive selection using the Reactome database[107] (**Figure 3C; Table**
247 **S3**). This includes 35 out of 65 genes in the high-fidelity Homologous Recombination Repair pathway,
248 and 21/37 members of the Homology-Directed Repair via Single Strand Annealing (**Figure 3C; Table**
249 **S3**). These results suggest that *M. lucifugus* might have an enhanced response to DNA DSBs relative to
250 other bats. To test this hypothesis, we assessed the tolerance of *M. lucifugus* to neocarzinostatin, a
251 potent radiomimetic agent that induces DNA double-strand breaks (**Figure 3D**), compared to *M. evotis*,
252 three non-*Myotis* bats (*Eidolon helvum, Pteropus rodrigensis,* and *Rousettus lanosus*), and humans. At
253 low doses of neocarzinostatin, *M. lucifugus* was the only species tested showing sensitivity to
254 neocarzinostatin after 24 hours, with a drop in viability and concomitant increase in apoptosis. At high
255 doses, *M. lucifugus* had the highest level of apoptosis and the greatest drop in viability of all the bats
256 tested, although all bats were more resistant to DNA damage than humans. This is consistent with other
257 long-lived species, including elephants[42,43,90], naked mole rats[51], and bowhead whales[46,108], where
258 longevity and RICR are associated with an increased ability to clear out damaged cells. Together, these
259 results support the hypothesis that *M. lucifugus* has evolved an enhanced DNA double-strand break
260 response as predicted by genes exhibiting signatures of positive selection in this species.

261 Adaptation to DNA viruses

262 Amongst genes under selection, a substantial portion were involved with immunity, including
263 members of the immunoglobulin and Cluster of Differentiation gene families. These genes exhibited some of
264 the highest evolutionary rates (ω) in our dataset, suggesting that they are under strong selection in *Myotis* (**Table**
265 **S3; Table S4**). Because immune pathways are only one aspect of host viral adaptation[109], we tested for
266 adaptive signatures in virus-interacting proteins (VIPs) in *Myotis* and other bats. VIPs are host proteins
267 that physically interact with viral proteins (e.g. *CD45*, **Figure 4A**), and can be proviral (contributing to viral

268 infection, e.g. viral receptors), antiviral (protective against viral infection, e.g. interferons), or both
269 depending on infection stage and virus type. Previous studies investigating positive selection across
270 mammals have found an enrichment for adaptation among a set of 5,528 manually curated VIPs, defined
271 as host proteins that have at least one experimentally verified physical interaction with a viral protein,
272 RNA, or DNA[109].

273 By calculating an enrichment score from the ratio of positive selection in VIPs compared to their
274 matched control genes using BUSTED-MH[110], we found that, like other mammals, *Myotis* show an
275 enrichment for adaptation at VIPs (**Figure 4B; Table S5**). Physical host-virus interactions may not always
276 result in fitness effects in the host. We therefore repeated our analysis using a gene set restricted to VIPs
277 with experimental evidence of specific pro- or anti-viral effects, and thus with a stronger expectation of
278 fitness effects. We observed an even stronger significant elevation in the ratio of positive selection in
279 these proviral and antiviral VIPs (**Figure 4C; Table S5**), but no elevation in this ratio in other VIPs (**Figure**
280 **4D; Table S5**). This is consistent with the expectation of viral interaction as the cause of enrichment of
281 positive selection in VIPs in bats[111]. We repeated this analysis using a dataset of 47 publicly-available
282 non-*Myotis* bat genomes, and confirmed these same patterns across bats more broadly, even when
283 excluding *Myotis* genomes (**Figure 4B** inset).

284 Previous work has suggested that bats may have different physiological responses to DNA and
285 RNA viruses[112]. To determine if this was reflected in genomic VIP adaptation, we compared the
286 enrichment of positive selection in VIPs that interact only with DNA viruses (DNA VIPs) to those that
287 interact only with RNA viruses (RNA VIPs). Remarkably, we found that VIP adaptation in *Myotis* and
288 other bats is driven by selection in DNA VIPs (**Figure 4E** and inset). This is in marked contrast to the
289 observed pattern in RNA VIPs, which show no evidence of enrichment in adaptation (**Figure 4F** and
290 inset). Note that this difference between DNA and RNA VIPs cannot be explained by a difference in the
291 conservation of VIP status between the two. The vast majority of VIPs were discovered between human
292 proteins and viruses that infect humans [111], and a concern could then be that those proteins that are RNA
293 VIPs in humans have evolved faster than DNA VIPs in bats, ultimately resulting in the more frequent loss
294 of their VIP status in bats. We can however exclude this possibility, since DNA and RNA VIPs have very
295 similar average dN/dS ratios (Myotis, 0.2 vs. 0.18 respectively; non-Myotis bats, 0.163 vs. 0.153
296 respectively).

297 In contrast to what we observe in bats, VIP adaptation in humans is driven by positive selection
298 in RNA - and not DNA - VIPs[109,113]. To investigate if DNA VIP-driven adaptation in bats is exceptional
299 among mammals, we replicated these analyses across four other large mammalian orders that are well
300 represented among publicly-available mammalian genomes: *Primates*, *Glires*, *Eeungulata*, and
301 *Carnivora*. We found that while other mammalian orders show a mix of adaptation enrichments in both
302 RNA and DNA VIPs, none show an absence of genome-wide enrichment of adaptation in RNA VIPs as
303 observed in bats (**Figure S4**). These results highlight that bats, including *Myotis*, may have faced greater
304 selective pressures from DNA viruses than from RNA viruses, in contrast to other mammals.

305 Evolution of structural variation within constrained karyotypes

306 With only six known exceptions, all *Myotis* species with cytological data have a conserved
307 karyotype (60+ *Myotis spp.*: 2n = 44[114–118]; *M. annectans*: 2n = 46[116]; *M. laniger*: 2n = 48[117]; *M. bechsteinii*:

308 2n = 42[119]; *M. daubentoni*: 2n = 42[120]; *M. davidii*: 2n = 46 [121]; *M. macrodactylus*: 2n = 44/45[122,123]). This
309 conserved *Myotis* karyotype, shared among species spread across six continents[1,2], consists of three
310 large autosomes and one small metacentric autosome; 17 small telocentric autosomes; and metacentric
311 X and Y chromosomes [57,124]. Consistent with this broad cytological conservation, we find large scale
312 synteny across the Nearctic *Myotis* in this study. However, structural variants (SVs) including inversions,
313 duplications, and translocations are relatively common within chromosomes, especially in putative
314 centromeric regions (**Figure 5A, B**).

315 We used SyRI[125] to identify SVs across pairwise alignments of Nearctic *Myotis* genomes relative
316 to the outgroup *M. myotis* and identified 6,813 - 8,013 SVs per genome. Most of these events were small,
317 with 97 - 99% of events under 10Kb. In the three large autosomes, which constitute ~30% of each
318 genome, we cataloged an average of 509 SVs (**Table S6**). In contrast, in the small autosomes,
319 constituting ~65% of each genome, we observed an average of 316 events, highlighting the distinct
320 structural evolution between these chromosome types (**Table S6**). However, large (≥10Kb) duplications,
321 large inverted duplications, and large inverted translocations were more common on small autosomes
322 compared to the large autosomes (**Table S6**).

323 We also quantified the distribution of transposable elements (TEs) across chromosomes.
324 Surprisingly, LINE elements were significantly enriched around the centromeres of all chromosomes,
325 both metacentric and telocentric (**Figure 5B**); while this is rare in mammals, it has been recently
326 described as a feature of Phyllostomid genomes[126]. In many cases, particularly in the 3 large metacentric
327 chromosomes, LINE elements appear to have displaced other TEs. Rolling circle and SINE elements
328 were particularly depleted concomitant with LINE enrichment. In contrast, SINE elements were enriched
329 at telomeres. The concentration of segmental duplications is significantly correlated with TE density in
330 each species (linear regression, $p < 0.01$; **Figure 5B; Figure S5J**) highlighting the possible importance
331 of TEs in facilitating structural evolution.

332 One particularly striking example of structural evolution we identified is a ~20-Mb block at the
333 subtelomeric end of chromosome V15 undergoing frequent and recurrent inversions and translocations
334 in nearctic *Myotis* (**Figure 5A**). This region spans several immune-related genes including multiple
335 members of interleukin signaling pathways, including IL-1 and IL-36. A 10Mb portion of this block was
336 recently identified as a potential target of recent selection by adaptive introgression[69]. We identified
337 between 2-3 major (8+ kb) blocks in this region exhibiting inversions between Nearctic *Myotis*, which
338 correspond to similarly sized regions in the outgroup *M. myotis* (**Figure 5A; Table S5**). Additionally, we
339 noted a depletion of DNA transposable elements at the boundaries of each inversion (**Figure 5B**),
340 particularly for rolling circle (RC) and SINE elements. Both of these elements can catalyze large-scale
341 structural rearrangements via DNA damage repair and homologous recombination, respectively[127–131].

342 Gene duplications and losses can be drivers of evolution via dosage modification[132,133], sub- and
343 neofunctionalization[134,135], regulatory network remodeling[136], and other processes[132]. We quantified gene
344 gains and losses across *Myotis* relative to their single-copy human orthologs. Using CAFE[137], we found
345 38 gene families underwent significant expansions or contractions in at least one nearctic *Myotis* species
346 (**Figure 5C**). However, gain and loss rates varied substantially across branches of the *Myotis* phylogeny.
347 The terminal *M. auriculus* and *M. velifer* branches had ~4-fold more significant gene family expansions
348 (37 and 35 families, respectively; **Figure 5C**) than other *Myotis* branches. In contrast, the terminal *M.*

349 *californicus* and *M. yumanensis* branches had ~2-fold more significant contractions (24 and 23 families,
350 respectively; **Figure 5C**) than other *Myotis* branches. We observe significant overrepresentation of
351 pathways at FDR<=10% in only 4 gene sets: gene families that underwent significant expansions in *M.*
352 *auriculus, M. velifer,* and *M. volans*; and genes that underwent significant contractions in *M. lucifugus*
353 (**Figure S5A-H**). Many of these pathways were shared between all sets, including pathways involved in
354 translation regulation; ROBO receptors and neuronal development; selenoprotein and selenocystine
355 metabolism; and influenza life cycle (**Figure S5A-H**).

356 Given that many of the genes in these pathways are VIPs, we used the method of Huang et al
357 (2023)[48] to test if VIP genes in particular underwent significant copy number changes relative to non-VIP
358 genes. We found that while the birth-death rate of VIP genes is similar to that of other genes ($p = 0.071$),
359 together VIP genes are significantly more likely to have undergone expansions and/or contractions on at
360 least one branch of the *Myotis* family ($p < 0.001$; **Figure S5I-J**). This suggests that there is variation in
361 gene family birth rates across species, but that VIPs are more dynamic across the Nearctic *Myotis* as a
362 whole than other types of genes.

363 To further explore the functional impact of gene duplications we ranked genes by their maximum
364 copy number across all genomes. We found that the gene families with the highest copy numbers were
365 concentrated in pathways associated with cancer, aging, immunity, and olfaction (**Figure 5D**). One
366 striking case is *FBXO31*, with ~2.4x more copies on average than the next most duplicated gene in *Myotis*
367 (20-48 copies). FBXO31 is a SCF (SKP1-cullin-F-box) protein ligase involved in cell cycle regulation and
368 DNA damage response, consisting of two functional domains: a F-Box domain and a CDK binding
369 domain[138], and has previously been speculated as a driver of longevity in *Myotis*[93]. Quantifying *FBXO31*
370 copy number across over 500 mammals using reciprocal best-hit BLAT, we found that this gene was
371 more highly duplicated in *Myotis* than in any other mammal genome (**Figure 5E)**. Furthermore, while
372 there were additional partial matches of non-canonical copies of *FBXO31* in non-*Myotis* species, all
373 copies identified in *Myotis* are full-length genes with functional domains. To model the evolution of gene
374 copy number, we used GeneRax[139] to reconcile the gene tree and species tree. GeneRax infers a gene
375 family tree under scenarios of gene duplication and loss, taking into account the species tree. We found
376 support for an original 14 duplications in the common ancestor of Nearctic *Myotis*, with subsequent gains
377 and losses in each lineage (**Figure 5F**). These results highlight a massively expanded gene family in
378 *Myotis* with potential consequences for the regulation of stress response and other processes.

379 An actively segregating, trans-species copy number polymorphism of 380 the antiviral factor Protein Kinase R, PKR

381 Our highly contiguous genome assemblies provide a unique opportunity to understand the
382 evolutionary and functional dynamics of structural variation in adaptation. To illustrate this, we explored
383 the antiviral innate immune Protein Kinase R (*PKR*/*EIF2AK2*), an interferon-stimulated gene with
384 adaptive duplications unique to *Myotis*[28]. Among our Neartic *Myotis* genome assemblies, we resolved the
385 structure of the two known structural haplotypes: H1, containing a single copy of *PKR* (*PKR2*); and H2,
386 containing two tandemly duplicated copies of *PKR* (*PKR1* and *PKR2*; **Figure 6A**). We also identified a
387 third haplotype - H3 - with three tandem duplicates of *PKR* (*PKR1*, *PKR2*, and a third copy). While 7 out
388 of 9 *Myotis* species carried duplicated haplotypes (H2 in 6 species, H3 in *M. californicus*), to our surprise,

389 5 of these cases were heterozygous for the duplicated haplotype: (i.e. H1/H2 or H1/H3; **Figure 6B**).
390 Furthermore, two *Myotis* individuals (*lucifugus* and *evotis*) only encoded for *PKR1* (i.e. H1/H1; **Figure**
391 **6B**). To determine the evolutionary history of the duplicates, we used GeneRax[139] to construct a tree from
392 alignments of all *PKR* gene copies across Neartic *Myotis*, using *Pipistrellus pygmaeus* as a non-*Myotis*
393 outgroup (**Figure 6C**). Our results suggest that *PKR2* is the ancestral copy of *PKR*, and that *PKR1*
394 originated from a single duplication event at the root of *Myotis*. Intriguingly, we observed that in the
395 heterozygous species, both *PKR1* and *PKR2* on the duplicated haplotype clustered with other duplicated
396 haplotypes, resulting in species tree violations for the ancestral copy, *PKR2* (**Figure 6C**). These results
397 highlight that both the duplicated and unduplicated haplotypes have likely been segregating for over 30
398 million years, representing an ancient trans-species polymorphism.

399 PKR is a stress response and innate immune factor that interacts with viral or inverted Alu repeats
400 dsRNAs via its dsRNA binding motifs (dsRBMs), leading to PKR auto-phosphorylation and
401 dimerization[140,141]. Upon activation, PKR can then phosphorylate various molecules leading to protein
402 translation shutdown and restriction of viral replication[140,141]. While the independent functional impacts of
403 PKR1 and PKR2 were previously investigated[28], the effects of co-expressing both copies remain
404 unknown. This is important because their final effects may be additive, synergistic or dominant negative,
405 providing clues into why the *PKR* duplication is polymorphic both within and between *Myotis* species. We
406 therefore investigated the functional impact of the duplicates' co-expression on steady state protein
407 levels, homo/hetero-dimer formation, cell viability, protein translation shutdown and antiviral restriction
408 (**Figure 6D-G**). We used PKR-KO Hela cells transfected with either *Myotis myotis* or *Myotis velifer* PKR1,
409 PKR2, and PKR1+2. We found that the coexpression of *Myotis* Flag-PKR1 and Flag-PKR2 did not affect
410 their protein expression levels (**Figure S6A**). Interestingly, co-immunoprecipitation (coIP) experiments
411 show that *Myotis myotis* PKR1 and PKR2 do not interact (i.e. no heterodimers), even though *Myotis*
412 *myotis* PKR1 can dimerize (**Figure 6D, Figure S6B**). Furthermore, coexpression of PKR1 and PKR2 led
413 to a simple additive effect in their translation shutdown activity (**Figure 6E**), suggesting that neither copy
414 is dominant negative. Using non-toxic doses of *Myotis* PKRs in the context of VSV-GFP (Vesicular
415 stomatitis virus encoding a GFP reporter[142]) infections, we found that, although PKR1 and PKR2 are both
416 antiviral[28], the coexpression of PKR1 and PKR2 is not beneficial against VSV (**Figure 6F**). Similar results
417 were found with an unrelated virus, SINV-GFP (Sindbis virus encoding a GFP reporter) (**Figure S6C**).
418 Finally, because duplicated haplotypes may lead to increased doses of PKR in *Myotis* cells, we tested
419 PKR impact on cell viability. We found that at low doses none of the *Myotis* PKRs affected cell viability.
420 However, higher doses of PKRs led to more cell toxicity, potentially resulting in a tradeoff (**Figure 6G**).
421 Altogether, this may explain why PKR is rarely duplicated in mammals, and why both single- and duplicate
422 haplotypes of the loci are segregating across several *Myotis* species. These genomic and functional
423 results highlight the impact of an unfixed gene duplicate which may play a role in adaptation to viral
424 infections.

Discussion

A functionally empowered approach to comparative genomics

Bats are widely known for their long lifespan, cancer resistance, and viral tolerance[6,10,11,36,70,89,143–145]. As highly complex and pleiotropic processes, the genes and mechanisms underlying these phenotypes can be challenging to identify. Comparative approaches to identify the genetic bases of these traits are constrained by the availability of high-quality genomes, annotations, and functional resources for validation. These challenges are exacerbated in the case of rapidly-evolving phenotypes, such as host-pathogen interactions.

Here we outline an approach that enables functional comparative biology by generating cell lines from wing punches of wild caught bats for genome assembly, comparative genomics, and functional follow up. Cell lines are generated from minimally-invasive biopsies collected in the field thus avoiding disturbing natural populations. Given the high density of bat species concentrated at single locations world-wide[146,147] it is feasible to collect wing punches from a large number of individuals across a wide phylogenetic range; these wing punches can be used to generate cell lines and sequencing libraries for reference genomes in a matter of weeks. This is an important advance, not only for efforts to expand genetic resources across the tree of life[148–150], but for conservation genomics. As our approach can generate genomic resources from minimal material gathered via non-lethal sampling, it is well-suited for the study of rare or endangered species for which acquiring sufficient amounts of material can be challenging.

Evolution of lifespan and cancer risk in a new phylogenetic context

The evolution of body size and lifespan across mammals - and the rapid evolution of lifespan in *Yinpterochiroptera* in particular - has major implications for the co-evolution of cancer risk and resistance. While models of body size evolution are well-studied in mammals[7,44,72,74] the evolution of lifespan is less well understood. By explicitly modeling the evolution of lifespan separately from body size, we recapitulate the extant relationship between body size and lifespan across mammals in evolutionary time. Contrary to prior work, we show that bats exhibit relaxed allometric scaling of lifespan comparable to other mammals. However, *Myotis* demonstrates an increased rate of change in lifespan given body size compared to other mammals. This altered scaling of longevity in *Myotis* has dramatic consequences for their intrinsic, per-cell cancer risk and for the evolution of tumor-suppressor genes and pathways. While cancer risk scales linearly with body size, it scales over time as a power law of 6[83,86,87]. Meanwhile, while mammalian body sizes span a 10^6 range of masses, they only span a 10^2 range of lifespans[16,151]. Unlike other systems where the evolution of cancer resistance has been driven by rapid changes in body size[42–44,50,91,94], the body size of *Myotis* has not significantly changed since their common ancestor. Instead, the rapid and repeated changes in lifespan across an order of magnitude in *Myotis* lead to some of the most significant changes in intrinsic cancer risk seen across mammals.

We found a number of genes under selection across multiple longevity-associated pathways, consistent with the pleiotropic nature of the aging process. These include members of canonical longevity pathways such as mTOR-IGF signaling, DNA damage repair, oxidative stress, and the senescence-

associated secretory phenotype. We additionally identified selection in various pathways that have likely emerged as a result of the unique biology of bats, including genes at the intersection of immunity and senescence, such as Serapin-family genes; genes in metabolic pathways including amino acid metabolism; and pervasive selection observed in the ferroptosis pathway, which sits at the intersection of bats' extreme oxidative challenges, metabolic demands, immune function, and cancer resistance. By quantifying the relative contributions of genes under selection to cancer-related pathways at each node, we found significant enrichment of these processes across the phylogeny, especially at nodes undergoing the greatest changes in lifespan and cancer risk.

While the implications of an increased cancer risk are clear, the implications of decreases in relative cancer risk are less so. As expected by Peto's Paradox, we observe an overrepresentation of cancer-related pathways among genes under selection at nodes experiencing high increases in relative cancer risk, consistent with patterns observed in other vertebrates[44,46,50,52,73,91–94]. However, we also observed an enrichment in cancer-related pathway representation among genes under selection in nodes with significant decreases in cancer risk (e.g: *M. thysanodes, M. velifer*). This combination of low intrinsic cancer risk alongside the persistence of cancer-related adaptations, has been observed previously in sloths and armadillos[73]. Intriguingly, these species demonstrate some of the lowest known rates of cancer among mammals. While no reports or studies of neoplasia rates have been published in *Myotis*, the use of *in vitro* models of carcinogenesis provides a promising avenue for comparative studies of cancer resistance under controlled conditions. In agreement with our results, *in vitro* and xenograft transplant models have shown that cells of long-lived bats, including *M. lucifugus,* are more resistant to carcinogenesis than shorter-lived bats and other mammals[145]. Such studies provide a reliable route for the experimental validation of the evolution of cancer resistance in species where *in vivo* work would otherwise prove ethically or practically intractable.

Viral adaptation and immunity

The nature of viral tolerance and infectious disease adaptation in bats has major implications for understanding their role as zoonotic reservoirs and mechanisms of infectious disease adaptation. Here we focus on Virus Interacting Proteins (VIPs) that influence viral response and contain vital information about the nature of host adaptation to viruses[109]. By integrating comparative analyses of VIP adaptation, VIP and immune gene family expansion and contraction, and functional experiments, we show that virus adaptation in bats is mostly driven by DNA viruses, as opposed to RNA viruses; we recapitulate and expand on previous results related to positive selection in immune genes and immune gene family expansion, contraction, and loss; and demonstrate complex patterns of structural variation, including a segregating duplication of protein kinase R (PKR), a major protein involved in the antiviral innate immune system, that has functional relevance in its activity against viruses.

The remarkable dominance of adaptation in response to DNA viruses in bats is in contrast with viral adaptation in humans and other primates, which is driven by RNA viruses[113,152]; and in other mammals, in which virus adaptation is driven by a combination of DNA and RNA viruses. Most zoonoses, including those hosted by bats, are RNA viruses[10], making this especially important in understanding the dynamics of emerging infectious diseases. This novel finding complements previous observations that bats are more likely than other mammals to asymptomatically harbor RNA viruses, while being more susceptible themselves to other pathogens, such as fungi[112]. This suggests multiple, non-exclusive,

504 possibilities. First, bats may have some other form of response to RNA viruses that sufficiently reduces
505 the fitness effect of these viruses such that the associated VIPs did not adapt as strongly. Second, our
506 result does not imply that bats have not adapted to RNA viruses, rather that adaptation to RNA viruses
507 does not exceed the genomic baseline adaptation, while adaptation to DNA viruses does. Indeed, bats
508 are known to mount adaptive immune responses to some RNA viruses and the strength of their immune
509 response can have complex interactions with hibernation and reproduction[10]. It has been previously
510 suggested that bats may rely more strongly on adaptive immunity in response to RNA viruses than to
511 other pathogens[112], though evolutionary functional analyses have also found evidence of innate immune
512 adaptation to RNA viruses, including *RTP4* to flaviviruses[153] and *OAS1* to SARS-COVs[154]. This is
513 consistent with our findings of positive selection and gene family expansion in adaptive immune proteins.

514 While previous work has shown associations between gene family size and certain phenotypic
515 traits in bats[36,54,155,156], confirmation of functional effects of copy number is rare. By resolving individual
516 haplotypes in these nine *Myotis* species, we were able to confirm a single duplication event at the origin
517 of *Myotis PKR1* and *PKR2*. We further demonstrate functional implications of copy number variation in
518 Protein kinase R, as previously shown in functional evolutionary studies (eg. Jacquet et al. 2022). These
519 results are especially interesting in the light of other studies that have found trans-species polymorphisms
520 related to immune genes[157]. This further illustrates the importance of high-quality genome assemblies
521 and annotations, to distinguish copy number variation between haplotypes, as well as between functional
522 copies and pseudogenes[158].

523 The role of agonistic pleiotropy in driving adaptations in bats

524 Multiple hypotheses have been proposed to connect the unique physiology and ecology of bats
525 with the evolution of remarkable adaptations such as viral infection tolerance, stress tolerance, and
526 exceptional longevity[143]. Hypothesized drivers of disease resistance and longevity evolution in bats
527 include the evolution of flight (e.g. "flight as fever" hypothesis[159], though this hypothesis has recently been
528 critiqued[160]), the disposable soma hypothesis[161]; metabolic state[162]; torpor[6]; and other adaptations to
529 specific environments[9,156,163,164]. Additionally, many studies have highlighted the intersection of one or
530 more of these traits, including a relationship between hibernation and both longevity[6] and disease
531 resistance[112]. Our results are consistent with an *agonistic* pleiotropy hypothesis, wherein genetic
532 adaptations for many specific traits (e.g. physiological stress to flight, hibernation, DNA virus innate
533 immunity) may prove beneficial to other seemingly-unrelated traits (e.g. cancer resistance, cellular
534 homeostasis, longevity).

535 Consistent with this, many of the genes and pathways highlighted in this study have been found
536 to play vital roles across physiological traits in bats and other species. For example, two genes under
537 selection in neartic *Myotis* - *FTH1* and *IGFN1* - have been implicated in functional studies as key
538 hibernation genes[165–167], viral interacting proteins[168–171], and as pro-longevity genes[172–174]. Similarly, many
539 DNA VIPs such as *BRCA1/2* and *POLG* represent core DNA maintenance genes essential for cancer
540 resistance and longevity[51,175–181]; the existence of active DNA transposable elements such as *Helitron* in
541 *Myotis* may provide another selective pressure on DNA repair genes[182]. Beyond individual genes, many
542 of the overarching pathways under selection in *Myotis*, such as those associated with inflammation,
543 senescence, and ferroptosis lie directly at the intersection of aging-related immune
544 processes[36,54,56,75,167,172,183–188]. While these results suggest the possibility that traits such as cancer risk,

545 cellular homeostasis, and antiviral response have evolved in tandem due to pleiotropic selection at
546 overlapping points in bats' evolutionary histories, further functional validation will be required to
547 disentangle the functional impacts of these genetic changes and disambiguate the drivers of selection.

548 Acknowledgements

549 PacBio HiFi sequencing was done by the DNA Technologies and Expression Analysis Cores at the UC
550 Davis Genome Center, supported by NIH Shared Instrumentation Grant 1S10OD010786-01. This
551 material is based in part upon High Performance Computing (HPC) resources supported by the University
552 of Arizona TRIF, UITS, and Research, Innovation, and Impact (RII) and maintained by the UArizona
553 Research Technologies department. This research used the Savio computational cluster resource
554 provided by the Berkeley Research Computing program at the University of California, Berkeley
555 (supported by the UC Berkeley Chancellor, Vice Chancellor for Research, and Chief Information Officer).
556 Computations were performed, in part, on the Vermont Advanced Computing Core. We thank the
557 members of the LP2L team (CIRI) for helpful discussions.

558 MEL was funded by NSF PRFB #2010884, and a Dovetail Tree of Life Grant. JMV was funded by NSF
559 PRFB #2109915 and NIH NIA T32AG000266. DE was funded by NIH NIGMS MIRA grant
560 5R35GM142677. PHS was funded by NIH NIGMS grant R35GM142916 and by the Vallee Scholars
561 Award. LE was funded by a grant from the Agence Nationale de la Recherche (ANR, #ANR-202-CE15-
562 0020-01 to LE) and by the CNRS. LE and DE were further funded by a grant from the Joint Call for
563 Proposals between the CNRS and the University of Arizona (International Research Center, IRC, 2021-
564 2024). LE, DE, PHS and SP were further funded by the International Research Project (IRP) RAPIDvBAT
565 from the CNRS, the University of Arizona and the University of California, Berkeley.

566 Image attributions for the bat photos featured in Figure 1: J. Scott Altenbach (*M. thysanodes, M. velifer*);
567 Rick & Nora Bowers (*M. occultus*); U.S. National Park Service (*M. auriculus*); Frank Carey (*M.*
568 *californicus*); Michael Durham (*M. evotis*); J. N. Stuart (*M. volans*); and SMBishop & the Wikimedia
569 Foundation (*M. lucifugus*).

570 Author Contributions:

571 Conceptualization, J.M.V., M.E.L., D.E., P.H.S., L.E., D.F., M.B.; Methodology, J.M.V., M.E.L.,
572 D.E., P.H.S., L.E., G.G.S.; Software, J.M.V., M.E.L., D.E., P.H.S., L.E., T.M.L.; Validation,
573 J.M.V., M.E.L., D.E., P.H.S., L.E., J.P.V.M.; Formal Analysis, J.M.V., M.E.L., D.E., P.H.S., L.E.,
574 S.M., A.L.C., D.M., S.V.; Investigation, J.M.V., M.E.L., S.M., M.B., D.F., G.G.S., L.G., Z.R.H.,
575 M.H., W.K., T.M.L., A.L.C., C.L. S.M., D.M., S.L., J.L., C.R., S.L.R.C., M.S., K.S., W.T., J.D.T.,
576 S.V., R.M., M.B., J.P.V.M., S.P., L.E., D.E., P.H.S.; Resources, J.M.V., M.E.L., D.E., P.H.S.,
577 L.E., M.B., D.F., G.G.S., L.G., Z.R.H., M.H., W.K., T.M.L., A.L.C., S.M., D.M., S.L., J.L., C.R.,
578 S.L.R.C., M.S., K.S., W.T., J.D.T., S.V., R.M., M.B.; Data Curation, J.M.V., M.E.L., S.M., M.B.,
579 D.F., G.G.S., L.G., Z.R.H., M.H., W.K., T.M.L., A.L.C., S.M., D.M., S.L., J.L., C.R., S.L.R.C.,
580 M.S., K.S., W.T., J.D.T., S.V., R.M., M.B., J.P.V.M., S.P., L.E., D.E., P.H.S.; Writing - Original
581 Draft, J.M.V., M.E.L., D.E., P.H.S., L.E., S.M., J.L.; Writing - Review & Editing, J.M.V., M.E.L.,

S.M., M.B., D.F., G.G.S., L.G., Z.R.H., M.H., W.K., T.M.L., A.L.C., S.M., D.M., S.L., J.L., C.R., S.L.R.C., M.S., K.S., W.T., J.D.T., S.V., R.M., M.B., J.P.V.M., S.P., L.E., D.E., P.H.S.; Visualization, J.M.V., M.E.L., D.E., P.H.S., L.E., S.M., A.L.C.; Supervision, J.M.V., M.E.L., D.E., P.H.S., L.E.; Project Administration, J.M.V., M.E.L., D.E., P.H.S., L.E.; Funding Acquisition, J.M.V., M.E.L., D.E., P.H.S., L.E.

Declaration of Interests:

The authors declare no competing interests.

References

1. Wilson, D.E., and Reeder, D.M. (2005). Mammal Species of the World: A Taxonomic and Geographic Reference (JHU Press).

2. Simmons, N.B., and Cirranello, A.L. Bat Species of the World: A Taxonomic and Geographic Database. https://batnames.org/.

3. Teeling, E.C., Hedges, S.B., and Kumar, S. (2009). Bats (Chiroptera). The timetree of life, 499–503.

4. Rietbergen, T.B., Ostende, L.W. van den H., Aase, A., Jones, M.F., Medeiros, E.D., and Simmons, N.B. (2023). The Oldest Known Bat Skeletons and Their Implications for Eocene Chiropteran Diversification. PLoS One *18*, e0283505. https://doi.org/10.1371/journal.pone.0283505.

5. Kumar, S., Stecher, G., Suleski, M., and Hedges, S.B. (2017). TimeTree: A Resource for Timelines, Timetrees, and Divergence Times. Mol. Biol. Evol. *34*, 1812–1819. https://doi.org/10.1093/molbev/msx116.

6. Wilkinson, G.S., and Adams, D.M. (2019). Recurrent Evolution of Extreme Longevity in Bats. Biol. Lett. *15*, 20180860. https://doi.org/10.1098/rsbl.2018.0860.

7. Moyers Arévalo, R.L., Amador, L.I., Almeida, F.C., and Giannini, N.P. (2020). Evolution of Body Mass in Bats: Insights from a Large Supermatrix Phylogeny. J. Mamm. Evol. *27*, 123–138. https://doi.org/10.1007/s10914-018-9447-8.

8. Datzmann, T., von Helversen, O., and Mayer, F. (2010). Evolution of Nectarivory in Phyllostomid Bats (Phyllostomidae Gray, 1825, Chiroptera: Mammalia). BMC Evol. Biol. *10*, 165. https://doi.org/10.1186/1471-2148-10-165.

9. Camacho, J., Bernal-Rivera, A., Peña, V., Morales-Sosa, P., Robb, S., Russell, J., Yi, K., Wang, Y., Tsuchiya, D., Murillo-García, O.E., et al. (2023). Sugar assimilation underlying dietary evolution of Neotropical bats. bioRxiv, 2023.07.02.547432. https://doi.org/10.1101/2023.07.02.547432.

10. Hayman, D.T.S., Bowen, R.A., Cryan, P.M., McCracken, G.F., O'Shea, T.J., Peel, A.J., Gilbert, A., Webb, C.T., and Wood, J.L.N. (2013). Ecology of zoonotic infectious diseases in

bats: current knowledge and future directions. Zoonoses Public Health *60*, 2–21. https://doi.org/10.1111/zph.12000.

11. Irving, A.T., Ahn, M., Goh, G., Anderson, D.E., and Wang, L.-F. (2021). Lessons from the host defences of bats, a unique viral reservoir. Nature *589*, 363–370. https://doi.org/10.1038/s41586-020-03128-0.

12. Morales, A.E., Ruedi, M., Field, K., and Carstens, B.C. (2019). Diversification rates have no effect on the convergent evolution of foraging strategies in the most speciose genus of bats, Myotis. Evolution *73*, 2263–2280. https://doi.org/10.1111/evo.13849.

13. Gunnell, G.F., Smith, R., and Smith, T. (2017). 33 million year old Myotis (Chiroptera, Vespertilionidae) and the rapid global radiation of modern bats. PLoS One *12*, e0172621. https://doi.org/10.1371/journal.pone.0172621.

14. Ruedi, M., Stadelmann, B., Gager, Y., Douzery, E.J.P., Francis, C.M., Lin, L.-K., Guillén-Servent, A., and Cibois, A. (2013). Molecular Phylogenetic Reconstructions Identify East Asia as the Cradle for the Evolution of the Cosmopolitan Genus Myotis (Mammalia, Chiroptera). Mol. Phylogenet. Evol. *69*, 437–449. https://doi.org/10.1016/j.ympev.2013.08.011.

15. Tacutu, R., Craig, T., Budovsky, A., Wuttke, D., Lehmann, G., Taranukha, D., Costa, J., Fraifeld, V.E., and de Magalhães, J.P. (2013). Human Ageing Genomic Resources: Integrated Databases and Tools for the Biology and Genetics of Ageing. Nucleic Acids Res. *41*, D1027–D1033. https://doi.org/10.1093/nar/gks1155.

16. Jones, K.E., Bielby, J., Cardillo, M., Fritz, S.A., O'Dell, J., Orme, C.D.L., Safi, K., Sechrest, W., Boakes, E.H., Carbone, C., et al. (2009). PanTHERIA: A Species-Level Database of Life History, Ecology, and Geography of Extant and Recently Extinct Mammals. Ecology *90*, 2648–2648. https://doi.org/10.1890/08-1494.1.

17. Austad, S.N. (2010). Methusaleh's Zoo: How Nature Provides Us with Clues for Extending Human Health Span. J. Comp. Pathol. *142*, S10–S21. https://doi.org/10.1016/j.jcpa.2009.10.024.

18. Austad, S.N., and Fischer, K.E. (1991). Mammalian Aging, Metabolism, and Ecology: Evidence from the Bats and Marsupials. J. Gerontol. *46*, B47–B53. https://doi.org/10.1093/geronj/46.2.b47.

19. Podlutsky, A.J., Khritankov, A.M., Ovodov, N.D., and Austad, S.N. (2005). A new field record for bat longevity. J. Gerontol. A Biol. Sci. Med. Sci. *60*, 1366–1368. https://doi.org/10.1093/gerona/60.11.1366.

20. Wilson, D.E., and Tyson, E.L. (1970). Longevity Records for Artibeus Jamaicensis and Myotis Nigricans. J. Mammal. *51*, 203. https://doi.org/10.2307/1378570.

21. Stadelmann, B., Lin, L.-K., Kunz, T.H., and Ruedi, M. (2007). Molecular Phylogeny of New World \emphMyotis (Chiroptera, Vespertilionidae) Inferred from Mitochondrial and Nuclear DNA Genes. Mol. Phylogenet. Evol. *43*, 32–48. https://doi.org/10.1016/j.ympev.2006.06.019.

22. Agnarsson, I., Zambrana-Torrelio, C.M., Flores-Saldana, N.P., and May-Collado, L.J.

657 (2011). A time-calibrated species-level phylogeny of bats (Chiroptera, Mammalia). PLoS
658 Curr. *3*, RRN1212. https://doi.org/10.1371/currents.RRN1212.

659 23. Seltmann, A., Troxell, S.A., Schad, J., Fritze, M., Bailey, L.D., Voigt, C.C., and Czirják, G.Á.
660 (2022). Author Correction: Differences in acute phase response to bacterial, fungal and
661 viral antigens in greater mouse-eared bats (Myotis myotis). Sci. Rep. *12*, 21144.
662 https://doi.org/10.1038/s41598-022-25685-2.

663 24. Armero, A., Li, R., Bienes, K.M., Chen, X., Li, J., Xu, S., Chen, Y., Hughes, A.C., Berthet,
664 N., and Wong, G. (2022). Myotis fimbriatus virome, a window to virus diversity and
665 evolution in the genus Myotis. Viruses *14*, 1899. https://doi.org/10.3390/v14091899.

666 25. He, X., Korytář, T., Zhu, Y., Pikula, J., Bandouchova, H., Zukal, J., and Köllner, B. (2014).
667 Establishment of Myotis Myotis Cell Lines - Model for Investigation of Host-Pathogen
668 Interaction in a Natural Host for Emerging Viruses. PLoS One *9*, e109795.
669 https://doi.org/10.1371/journal.pone.0109795.

670 26. Hayward, J.A., Tachedjian, M., Johnson, A., Irving, A.T., Gordon, T.B., Cui, J., Nicolas, A.,
671 Smith, I., Boyd, V., Marsh, G.A., et al. (2022). Unique Evolution of Antiviral Tetherin in Bats.
672 J. Virol. *96*, e0115222. https://doi.org/10.1128/jvi.01152-22.

673 27. Fernandes, A.P., Águeda-Pinto, A., Pinheiro, A., Rebelo, H., and Esteves, P.J. (2022).
674 Evolution of TRIM5 and TRIM22 in Bats Reveals a Complex Duplication Process. Viruses
675 *14*. https://doi.org/10.3390/v14020345.

676 28. Jacquet, S., Culbertson, M., Zhang, C., El Filali, A., De La Myre Mory, C., Pons, J.-B.,
677 Filippi-Codaccioni, O., Lauterbur, M.E., Ngoubangoye, B., Duhayer, J., et al. (2022).
678 Adaptive duplication and genetic diversification of protein kinase R contribute to the
679 specificity of bat-virus interactions. Sci Adv *8*, eadd7540.
680 https://doi.org/10.1126/sciadv.add7540.

681 29. Jacquet, S., Pontier, D., and Etienne, L. (2020). Rapid Evolution of HERC6 and Duplication
682 of a Chimeric HERC5/6 Gene in Rodents and Bats Suggest an Overlooked Role of HERCs
683 in Mammalian Immunity. Front. Immunol. *11*, 605270.
684 https://doi.org/10.3389/fimmu.2020.605270.

685 30. Chomel, B., Stuckey, M., Boulouis, H., and Aguilar Setién, Á. (2014). Bat-Related
686 Zoonoses. Zoonoses - Infections Affecting Humans and Animals, 697–714.
687 https://doi.org/10.1007/978-94-017-9457-2_28.

688 31. Guth, S., Mollentze, N., Renault, K., Streicker, D.G., Visher, E., Boots, M., and Brook, C.E.
689 (2022). Bats host the most virulent-but not the most dangerous-zoonotic viruses. Proc. Natl.
690 Acad. Sci. U. S. A. *119*, e2113628119. https://doi.org/10.1073/pnas.2113628119.

691 32. Williams, E.P., Spruill-Harrell, B.M., Taylor, M.K., Lee, J., Nywening, A.V., Yang, Z.,
692 Nichols, J.H., Camp, J.V., Owen, R.D., and Jonsson, C.B. (2021). Common themes in
693 zoonotic spillover and disease emergence: Lessons learned from bat- and rodent-borne
694 RNA viruses. Viruses *13*, 1509. https://doi.org/10.3390/v13081509.

695 33. Mollentze, N., and Streicker, D.G. (2020). Viral zoonotic risk is homogenous among
696 taxonomic orders of mammalian and avian reservoir hosts. Proc. Natl. Acad. Sci. U. S. A.
697 *117*, 9423–9430. https://doi.org/10.1073/pnas.1919176117.

698 34. Tenthorey, J.L., Emerman, M., and Malik, H.S. (2022). Evolutionary Landscapes of Host-
699 Virus Arms Races. Annu. Rev. Immunol. *40*, 271–294. https://doi.org/10.1146/annurev-
700 immunol-072621-084422.

701 35. Klunk, J., Vilgalys, T.P., Demeure, C.E., Cheng, X., Shiratori, M., Madej, J., Beau, R., Elli,
702 D., Patino, M.I., Redfern, R., et al. (2022). Evolution of immune genes is associated with
703 the Black Death. Nature *611*, 312–319. https://doi.org/10.1038/s41586-022-05349-x.

704 36. Jebb, D., Huang, Z., Pippel, M., Hughes, G.M., Lavrichenko, K., Devanna, P., Winkler, S.,
705 Jermiin, L.S., Skirmuntt, E.C., Katzourakis, A., et al. (2020). Six reference-quality genomes
706 reveal evolution of bat adaptations. Nature *583*, 578–584. https://doi.org/10.1038/s41586-
707 020-2486-3.

708 37. Mynard, P., Algar, A.C., Lancaster, L.T., Bocedi, G., Fahri, F., Gubry-Rangin, C.,
709 Lupiyaningdyah, P., Nangoy, M., Osborne, O.G., Papadopulos, A.S.T., et al. (2023). Impact
710 of phylogenetic tree completeness and mis-specification of sampling fractions on trait
711 dependent diversification models. Syst. Biol. *72*, 106–119.
712 https://doi.org/10.1093/sysbio/syad001.

713 38. Garamszegi, L.Z., and Møller, A.P. (2010). Effects of sample size and intraspecific variation
714 in phylogenetic comparative studies: a meta-analytic review. Biol. Rev. Camb. Philos. Soc.
715 *85*, 797–805. https://doi.org/10.1111/j.1469-185X.2010.00126.x.

716 39. Garamszegi, L.Z. ed. (2014). Modern Phylogenetic Comparative Methods and Their
717 Application in Evolutionary Biology: Concepts and Practice (Springer)
718 https://doi.org/10.1007/978-3-662-43550-2.

719 40. Nabhan, A.R., and Sarkar, I.N. (2012). The impact of taxon sampling on phylogenetic
720 inference: a review of two decades of controversy. Brief. Bioinform. *13*, 122–134.
721 https://doi.org/10.1093/bib/bbr014.

722 41. Kolora, S.R.R., Owens, G.L., Vazquez, J.M., Stubbs, A., Chatla, K., Jainese, C., Seeto, K.,
723 McCrea, M., Sandel, M.W., Vianna, J.A., et al. (2021). Origins and Evolution of Extreme
724 Life Span in Pacific Ocean Rockfishes. Science *374*, 842–847.
725 https://doi.org/10.1126/science.abg5332.

726 42. Sulak, M., Fong, L., Mika, K., Chigurupati, S., Yon, L., Mongan, N.P., Emes, R.D., and
727 Lynch, V.J. (2016). Correction: TP53 copy number expansion is associated with the
728 evolution of increased body size and an enhanced DNA damage response in elephants.
729 Elife *5*. https://doi.org/10.7554/eLife.24307.

730 43. Vazquez, J.M., Sulak, M., Chigurupati, S., and Lynch, V.J. (2018). A Zombie LIF Gene in
731 Elephants Is Upregulated by TP53 to Induce Apoptosis in Response to DNA Damage. Cell
732 Rep. *24*, 1765–1776. https://doi.org/10.1016/j.celrep.2018.07.042.

733 44. Vazquez, J.M., and Lynch, V.J. (2021). Pervasive Duplication of Tumor Suppressors in
734 Afrotherians during the Evolution of Large Bodies and Reduced Cancer Risk. Elife *10*,
735 e65041. https://doi.org/10.7554/eLife.65041.

736 45. Davies, K.T.J., Tsagkogeorga, G., Bennett, N.C., Dávalos, L.M., Faulkes, C.G., and
737 Rossiter, S.J. (2014). Molecular Evolution of Growth Hormone and Insulin-like Growth
738 Factor 1 Receptors in Long-Lived, Small-Bodied Mammals. Gene *549*, 228–236.

739 https://doi.org/10.1016/j.gene.2014.07.061.

740 46. Vazquez, J.M., Kraft, M., and Lynch, V.J. (2022). A CDKN2C retroduplication in Bowhead
741 whales is associated with the evolution of extremely long lifespans and alerted cell cycle
742 dynamics. bioRxiv, 2022.09.07.506958. https://doi.org/10.1101/2022.09.07.506958.

743 47. Foote, A.D., Liu, Y., Thomas, G.W.C., Vinař, T., Alföldi, J., Deng, J., Dugan, S., van Elk,
744 C.E., Hunter, M.E., Joshi, V., et al. (2015). Convergent evolution of the genomes of marine
745 mammals. Nat. Genet. *47*, 272–275. https://doi.org/10.1038/ng.3198.

746 48. Huang, Z., Jiang, C., Gu, J., Uvizl, M., Power, S., Douglas, D., and Kacprzyk, J. (2023).
747 Duplications of Human Longevity-Associated Genes Across Placental Mammals. Genome
748 Biol. Evol. *15*. https://doi.org/10.1093/gbe/evad186.

749 49. Li, S., Vazquez, J.M., and Sudmant, P.H. (2023). The Evolution of Aging and Lifespan.
750 Trends Genet. *0*. https://doi.org/10.1016/j.tig.2023.08.005.

751 50. Glaberman, S., Bulls, S.E., Vazquez, J.M., Chiari, Y., and Lynch, V.J. (2021). Concurrent
752 Evolution of Antiaging Gene Duplications and Cellular Phenotypes in Long-Lived Turtles.
753 Genome Biol. Evol. *13*, evab244. https://doi.org/10.1093/gbe/evab244.

754 51. MacRae, S.L., Croken, M.M., Calder, R.B., Aliper, A., Milholland, B., White, R.R.,
755 Zhavoronkov, A., Gladyshev, V.N., Seluanov, A., Gorbunova, V., et al. (2015). DNA Repair
756 in Species with Extreme Lifespan Differences. Aging *7*, 1171–1184.
757 https://doi.org/10.18632/aging.100866.

758 52. Baines, C., Meitern, R., Kreitsberg, R., and Sepp, T. (2022). Comparative study of the
759 evolution of cancer gene duplications across fish. Evol. Appl. *15*, 1834–1845.
760 https://doi.org/10.1111/eva.13481.

761 53. López-Otín, C., Blasco, M.A., Partridge, L., Serrano, M., and Kroemer, G. (2013). The
762 Hallmarks of Aging. Cell *153*, 1194–1217. https://doi.org/10.1016/j.cell.2013.05.039.

763 54. Moreno Santillán, D.D., Lama, T.M., Gutierrez Guerrero, Y.T., Brown, A.M., Donat, P.,
764 Zhao, H., Rossiter, S.J., Yohe, L.R., Potter, J.H., Teeling, E.C., et al. (2021). Large-scale
765 genome sampling reveals unique immunity and metabolic adaptations in bats. Mol. Ecol.
766 *30*, 6449–6467. https://doi.org/10.1111/mec.16027.

767 55. Scheben, A., Mendivil Ramos, O., Kramer, M., Goodwin, S., Oppenheim, S., Becker, D.J.,
768 Schatz, M.C., Simmons, N.B., Siepel, A., and McCombie, W.R. (2023). Long-Read
769 Sequencing Reveals Rapid Evolution of Immunity- and Cancer-Related Genes in Bats.
770 Genome Biol. Evol. *15*. https://doi.org/10.1093/gbe/evad148.

771 56. Tian, S., Zeng, J., Jiao, H., Zhang, D., Zhang, L., Lei, C.-Q., Rossiter, S.J., and Zhao, H.
772 (2023). Comparative analyses of bat genomes identify distinct evolution of immunity in Old
773 World fruit bats. Sci Adv *9*, eadd0141. https://doi.org/10.1126/sciadv.add0141.

774 57. Sotero-Caio, C.G., Baker, R.J., and Volleth, M. (2017). Chromosomal evolution in
775 Chiroptera. Genes (Basel) *8*. https://doi.org/10.3390/genes8100272.

776 58. Nachtweide, S., and Stanke, M. (2019). Multi-Genome Annotation with AUGUSTUS.
777 Methods Mol. Biol. *1962*, 139–160. https://doi.org/10.1007/978-1-4939-9173-0_8.

59. Lomsadze, A., Ter-Hovhannisyan, V., Chernoff, Y.O., and Borodovsky, M. (2005). Gene identification in novel eukaryotic genomes by self-training algorithm. Nucleic Acids Res. *33*, 6494–6506. https://doi.org/10.1093/nar/gki937.

60. Shumate, A., and Salzberg, S.L. (2021). Liftoff: accurate mapping of gene annotations. Bioinformatics.

61. Kirilenko, B.M., Munegowda, C., Osipova, E., Jebb, D., Sharma, V., Blumer, M., Morales, A.E., Ahmed, A.-W., Kontopoulos, D.-G., Hilgers, L., et al. (2023). Integrating gene annotation with orthology inference at scale. Science *380*, eabn3107. https://doi.org/10.1126/science.abn3107.

62. Li, H. (2023). Protein-to-genome alignment with miniprot. Bioinformatics.

63. Simão, F.A., Waterhouse, R.M., Ioannidis, P., Kriventseva, E.V., and Zdobnov, E.M. (2015). BUSCO: assessing genome assembly and annotation completeness with single-copy orthologs. Bioinformatics *31*, 3210–3212. https://doi.org/10.1093/bioinformatics/btv351.

64. Manni, M., Berkeley, M.R., Seppey, M., and Zdobnov, E.M. (2021). BUSCO: assessing genomic data quality and beyond. Current Protocols *1*.

65. Curti, J., Fraser, D., Escalona, M., Fairbairn, C.W., Sacco, S., Sahasrabudhe, R., Nguyen, O., Seligmann, W., Sudmant, P.H., Toffelmier, E., et al. (2023). A Genome Assembly of the Yuma Myotis Bat, Myotis Yumanensis. J. Hered., esad053. https://doi.org/10.1093/jhered/esad053.

66. Amador, L.I., Moyers Arévalo, R.L., Almeida, F.C., Catalano, S.A., and Giannini, N.P. (2018). Bat Systematics in the Light of Unconstrained Analyses of a Comprehensive Molecular Supermatrix. J. Mamm. Evol. *25*, 37–70. https://doi.org/10.1007/s10914-016-9363-8.

67. Upham, N.S., Esselstyn, J.A., and Jetz, W. (2019). Inferring the mammal tree: Species-level sets of phylogenies for questions in ecology, evolution, and conservation. PLoS Biol. *17*, e3000494. https://doi.org/10.1371/journal.pbio.3000494.

68. Korstian, J.M., Paulat, N.S., Platt, R.N., Stevens, R.D., and Ray, D.A. (2022). SINE-Based Phylogenomics Reveal Extensive Introgression and Incomplete Lineage Sorting in Myotis. Genes *13*, 399. https://doi.org/10.3390/genes13030399.

69. Foley, N.M., Harris, A.J., Bredemeyer, K.R., Ruedi, M., Puechmaille, S.J., Teeling, E.C., Criscitiello, M.F., and Murphy, W.J. (2024). Karyotypic stasis and swarming influenced the evolution of viral tolerance in a species-rich bat radiation. Cell Genom *4*, 100482. https://doi.org/10.1016/j.xgen.2023.100482.

70. Brunet-Rossinni, A.K., and Austad, S.N. (2004). Ageing studies on bats: a review. Biogerontology *5*, 211–222. https://doi.org/10.1023/B:BGEN.0000038022.65024.d8.

71. Wilkinson, G.S., and South, J.M. (2002). Life History, Ecology and Longevity in Bats. Aging Cell *1*, 124–131. https://doi.org/10.1046/j.1474-9728.2002.00020.x.

72. Puttick, M.N., and Thomas, G.H. (2015). Fossils and living taxa agree on patterns of body

817 mass evolution: a case study with Afrotheria. Proc. Biol. Sci. *282*, 20152023.
818 https://doi.org/10.1098/rspb.2015.2023.

819 73. Vazquez, J.M., Pena, M.T., Muhammad, B., Kraft, M., Adams, L.B., and Lynch, V.J. (2022).
820 Parallel Evolution of Reduced Cancer Risk and Tumor Suppressor Duplications in
821 Xenarthra. Elife *11*, e82558. https://doi.org/10.7554/eLife.82558.

822 74. Slater, G.J., Goldbogen, J.A., and Pyenson, N.D. (2017). Independent evolution of baleen
823 whale gigantism linked to Plio-Pleistocene ocean dynamics. Proc. Biol. Sci. *284*.
824 https://doi.org/10.1098/rspb.2017.0546.

825 75. Ricklefs, R.E. (2010). Life-history connections to rates of aging in terrestrial vertebrates.
826 Proc. Natl. Acad. Sci. U. S. A. *107*, 10314–10319.
827 https://doi.org/10.1073/pnas.1005862107.

828 76. Tillquist, R.C., Shoemaker, L.G., Knight, K.B., and Clauset, A. (2016). The evolution of
829 primate body size: Left-skewness, maximum size, and Cope's Rule. bioRxiv, 092866.
830 https://doi.org/10.1101/092866.

831 77. Kuparinen, A., Yeung, E., and Hutchings, J.A. (2023). Correlation between body size and
832 longevity: New analysis and data covering six taxonomic classes of vertebrates. Acta
833 Oecol. (Montrouge) *119*, 103917. https://doi.org/10.1016/j.actao.2023.103917.

834 78. Montgomery, S.H., Geisler, J.H., McGowen, M.R., Fox, C., Marino, L., and Gatesy, J.
835 (2013). The evolutionary history of cetacean brain and body size: Cetacean brain evolution.
836 Evolution *67*, 3339–3353. https://doi.org/10.1111/evo.12197.

837 79. Pyenson, N.D., and Sponberg, S.N. (2011). Reconstructing body size in extinct crown
838 Cetacea (neoceti) using allometry, phylogenetic methods and tests from the fossil record. J.
839 Mamm. Evol. *18*, 269–288. https://doi.org/10.1007/s10914-011-9170-1.

840 80. Delsuc, F., Gibb, G.C., Kuch, M., Billet, G., Hautier, L., Southon, J., Rouillard, J.-M.,
841 Fernicola, J.C., Vizcaíno, S.F., MacPhee, R.D.E., et al. (2016). The phylogenetic affinities
842 of the extinct glyptodonts. Curr. Biol. *26*, R155–R156.
843 https://doi.org/10.1016/j.cub.2016.01.039.

844 81. Argot, C. (2008). Changing Views in Paleontology: The Story of a Giant (Megatherium,
845 Xenarthra). In Mammalian Evolutionary Morphology Vertebrate Paleobiology and
846 Paleoanthropology Series., E. J. Sargis and M. Dagosto, eds. (Springer Netherlands), pp.
847 37–50. https://doi.org/10.1007/978-1-4020-6997-0_3.

848 82. Raj Pant, S., Goswami, A., and Finarelli, J.A. (2014). Complex body size trends in the
849 evolution of sloths (Xenarthra: Pilosa). BMC Evol. Biol. *14*, 184.
850 https://doi.org/10.1186/s12862-014-0184-1.

851 83. Armitage, P. (1985). Multistage Models of Carcinogenesis. Environ. Health Perspect. *63*,
852 195–201. https://doi.org/10.1289/ehp.8563195.

853 84. Armitage, P., and Doll, R. (2004). The Age Distribution of Cancer and a Multi-Stage Theory
854 of Carcinogenesis. Br. J. Cancer *91*, 6602297. https://doi.org/10.1038/sj.bjc.6602297.

855 85. Peto, R., Roe, F.J., Lee, P.N., Levy, L., and Clack, J. (1975). Cancer and ageing in mice

and men. Br. J. Cancer *32*, 411–426. https://doi.org/10.1038/bjc.1975.242.

86. Peto, R. (2015). Quantitative Implications of the Approximate Irrelevance of Mammalian Body Size and Lifespan to Lifelong Cancer Risk. Philos. Trans. R. Soc. Lond. B Biol. Sci. *370*, 20150198. https://doi.org/10.1098/rstb.2015.0198.

87. Nunney, L. (2018). Size Matters: Height, Cell Number and a Person's Risk of Cancer. Proc. R. Soc. B *285*, 20181743. https://doi.org/10.1098/rspb.2018.1743.

88. Caulin, A.F., and Maley, C.C. (2011). Peto's Paradox: evolution's prescription for cancer prevention. Trends Ecol. Evol. *26*, 175–182. https://doi.org/10.1016/j.tree.2011.01.002.

89. Vincze, O., Colchero, F., Lemaître, J.-F., Conde, D.A., Pavard, S., Bieuville, M., Urrutia, A.O., Ujvari, B., Boddy, A.M., Maley, C.C., et al. (2022). Cancer risk across mammals. Nature *601*, 263–267. https://doi.org/10.1038/s41586-021-04224-5.

90. Abegglen, L.M., Caulin, A.F., Chan, A., Lee, K., Robinson, R., Campbell, M.S., Kiso, W.K., Schmitt, D.L., Waddell, P.J., Bhaskara, S., et al. (2015). Potential Mechanisms for Cancer Resistance in Elephants and Comparative Cellular Response to DNA Damage in Humans. JAMA *314*, 1850–1860. https://doi.org/10.1001/jama.2015.13134.

91. Tollis, M., Robbins, J., Webb, A., Kuderna, L.F.K., Caulin, A.F., Garcia, J.D., Bérubé, M., Pourmand, N., Marquès-Bonet, T., O'Connell, M., et al. (2019). Return to the sea, get huge, beat cancer: An analysis of cetacean genomes including an assembly for the humpback whale (Megaptera novaeangliae). Mol. Biol. Evol. *36*, 1746–1763. https://doi.org/10.1093/molbev/msz099.

92. Tollis, M., Schneider-Utaka, A.K., and Maley, C.C. (2020). The evolution of human cancer gene duplications across mammals. Mol. Biol. Evol. *37*, 2875–2886. https://doi.org/10.1093/molbev/msaa125.

93. Caulin, A.F., Graham, T.A., Wang, L.-S., and Maley, C.C. (2015). Solutions to Peto's paradox revealed by mathematical modelling and cross-species cancer gene analysis. Philos. Trans. R. Soc. Lond. B Biol. Sci. *370*, 20140222. https://doi.org/10.1098/rstb.2014.0222.

94. Nair, N.U., Cheng, K., Naddaf, L., Sharon, E., Pal, L.R., Rajagopal, P.S., Unterman, I., Aldape, K., Hannenhalli, S., Day, C.-P., et al. (2022). Cross-species identification of cancer resistance-associated genes that may mediate human cancer risk. Sci. Adv. *8*, eabj7176. https://doi.org/10.1126/sciadv.abj7176.

95. Smith, M.D., Wertheim, J.O., Weaver, S., Murrell, B., Scheffler, K., and Kosakovsky Pond, S.L. (2015). Less is more: an adaptive branch-site random effects model for efficient detection of episodic diversifying selection. Mol. Biol. Evol. *32*, 1342–1353. https://doi.org/10.1093/molbev/msv022.

96. Hanahan, D., and Weinberg, R.A. (2011). Hallmarks of Cancer: The Next Generation. Cell *144*, 646–674. https://doi.org/10.1016/j.cell.2011.02.013.

97. Hanahan, D., and Weinberg, R.A. (2000). The Hallmarks of Cancer. Cell *100*, 57–70. https://doi.org/10.1016/S0092-8674(00)81683-9.

895 98. Hanahan, D. (2022). Hallmarks of Cancer: New Dimensions. Cancer Discov. *12*, 31–46.
896 https://doi.org/10.1158/2159-8290.CD-21-1059.

897 99. Wertheim, J.O., Murrell, B., Smith, M.D., Kosakovsky Pond, S.L., and Scheffler, K. (2015).
898 RELAX: detecting relaxed selection in a phylogenetic framework. Mol. Biol. Evol. *32*, 820–
899 832. https://doi.org/10.1093/molbev/msu400.

900 100. Wang, A., Zhu, F., Liang, R., Li, D., and Li, B. (2019). Regulation of T cell differentiation
901 and function by ubiquitin-specific proteases. Cell. Immunol. *340*, 103922.
902 https://doi.org/10.1016/j.cellimm.2019.103922.

903 101. Meng, Y., Hong, C., Yang, S., Qin, Z., Yang, L., and Huang, Y. (2023). Roles of USP9X in
904 cellular functions and tumorigenesis (Review). Oncol. Lett. *26*, 506.
905 https://doi.org/10.3892/ol.2023.14093.

906 102. Dohmen, M., Krieg, S., Agalaridis, G., Zhu, X., Shehata, S.N., Pfeiffenberger, E., Amelang,
907 J., Bütepage, M., Buerova, E., Pfaff, C.M., et al. (2020). AMPK-dependent activation of the
908 Cyclin Y/CDK16 complex controls autophagy. Nat. Commun. *11*, 1032.
909 https://doi.org/10.1038/s41467-020-14812-0.

910 103. Wang, X., Liu, R., Li, S., Xia, W., Guo, H., Yao, W., Liang, X., Lu, Y., and Zhang, H. (2023).
911 The roles, molecular interactions, and therapeutic value of CDK16 in human cancers.
912 Biomed. Pharmacother. *164*, 114929. https://doi.org/10.1016/j.biopha.2023.114929.

913 104. Katoh, Y., and Katoh, M. (2009). FGFR2-related pathogenesis and FGFR2-targeted
914 therapeutics (Review). Int. J. Mol. Med. *23*, 307–311.
915 https://doi.org/10.3892/ijmm_00000132.

916 105. Wang, K., Lai, C., Li, T., Wang, C., Wang, W., Ni, B., Bai, C., Zhang, S., Han, L., Gu, H., et
917 al. (2018). Basic fibroblast growth factor protects against influenza A virus-induced acute
918 lung injury by recruiting neutrophils. J. Mol. Cell Biol. *10*, 573–585.
919 https://doi.org/10.1093/jmcb/mjx047.

920 106. Kowalczyk, A., Meyer, W.K., Partha, R., Mao, W., Clark, N.L., and Chikina, M. (2019).
921 RERconverge: an R package for associating evolutionary rates with convergent traits.
922 Bioinformatics *35*, 4815–4817. https://doi.org/10.1093/bioinformatics/btz468.

923 107. Milacic, M., Beavers, D., Conley, P., Gong, C., Gillespie, M., Griss, J., Haw, R., Jassal, B.,
924 Matthews, L., May, B., et al. (2024). The reactome pathway knowledgebase 2024. Nucleic
925 Acids Res. *52*, D672–D678. https://doi.org/10.1093/nar/gkad1025.

926 108. Firsanov, D., Zacher, M., Tian, X., Zhao, Y., George, J.C., Sformo, T.L., Tombline, G.,
927 Biashad, S.A., Gilman, A., Hamilton, N., et al. (2023). DNA repair and anti-cancer
928 mechanisms in the longest-living mammal: the bowhead whale. bioRxiv,
929 2023.05.07.539748. https://doi.org/10.1101/2023.05.07.539748.

930 109. Enard, D., Cai, L., Gwennap, C., and Petrov, D.A. (2016). Viruses are a dominant driver of
931 protein adaptation in mammals. Elife *5*. https://doi.org/10.7554/eLife.12469.

932 110. Murrell, B., Weaver, S., Smith, M.D., Wertheim, J.O., Murrell, S., Aylward, A., Eren, K.,
933 Pollner, T., Martin, D.P., Smith, D.M., et al. (2015). Gene-wide identification of episodic
934 selection. Mol. Biol. Evol. *32*, 1365–1371. https://doi.org/10.1093/molbev/msv035.

935 111. Souilmi, Y., Lauterbur, M.E., Tobler, R., Huber, C.D., Johar, A.S., Moradi, S.V., Johnston,
936 W.A., Krogan, N.J., Alexandrov, K., and Enard, D. (2021). An ancient viral epidemic
937 involving host coronavirus interacting genes more than 20,000 years ago in East Asia. Curr.
938 Biol. *31*, 3704. https://doi.org/10.1016/j.cub.2021.07.052.

939 112. Brook, C.E., and Dobson, A.P. (2015). Bats as "special" reservoirs for emerging zoonotic
940 pathogens. Trends Microbiol. *23*, 172–180. https://doi.org/10.1016/j.tim.2014.12.004.

941 113. Enard, D., and Petrov, D.A. (2018). Evidence that RNA Viruses Drove Adaptive
942 Introgression between Neanderthals and Modern Humans. Cell *175*, 360–371.e13.
943 https://doi.org/10.1016/j.cell.2018.08.034.

944 114. Volleth, M. (2012). Variations on a theme: Karyotype comparison in Eurasian Myotis
945 species and implications for phylogeny. Vespertilio *16*, 329–350.

946 115. McBee, K. (1986). Standard karyology of nine species of vespertilionid bats (Chiroptera:
947 Vespertilionidae) from Thailand. Annals of Carnegie Museum *55*, 95–116.

948 116. Bickham, J.W., McBee, K., and Schlitter, D.A. (1986). Chromosomal variation among seven
949 species of Myotis (Chiroptera: Vespertilionidae). J. Mammal. *67*, 746–750.
950 https://doi.org/10.2307/1381139.

951 117. Zhang, W.D. (1984). A study on karyotype of Myotis chinensis and M. laniger Peter. J
952 Anhui Normal Univ *7*, 42–47.

953 118. Zima, J. (1985). Synopsis of karyotypes of vespertilionid bats (Mammalia: Chiroptera). Acta
954 Univ. Carol. Biol *1981*, 311–329.

955 119. Karataş, A., Sözen, M., Özkurt, Ş., and Matur, F. (2007). Karyology of three bat species of
956 the genusMyotis (M. myotis, M. bechsteinii, M. brandtii)(Chiroptera: Vespertilionidae) from
957 Turkey. Zool. Middle East *40*, 5–9. https://doi.org/10.1080/09397140.2007.10638198.

958 120. Bovey, R. (1949). Chromosones of Chiroptera and Insectivora.

959 121. Yi, W.U., and Harada, M. (2006). Karyology of seven species of bats (Mammalia:
960 Chiroptera) from Guangdong, China. Shou Lei Xue Bao *26*, 403.

961 122. Yoshitaka Obara, Takafumi Tomiyasu, and Kazuo Saitoh (1976). CHROMOSOME
962 STUDIES IN THE JAPANESE VESPERTILIONID BATS: I. KARYOTYPIC VARIATIONS IN
963 MYOTIS MACRODACTYLUS TEMMINCK. Jpn. J. Genet. *51*, 201–206.

964 123. Vujošević, M., Rajičić, M., and Blagojević, J. (2018). B Chromosomes in Populations of
965 Mammals Revisited. Genes *9*. https://doi.org/10.3390/genes9100487.

966 124. O'Brien, S.J., Menninger, J.C., and Nash, W.G. (2006). Atlas of Mammalian Chromosomes
967 (John Wiley & Sons).

968 125. Goel, M., Sun, H., Jiao, W.-B., and Schneeberger, K. (2019). SyRI: finding genomic
969 rearrangements and local sequence differences from whole-genome assemblies. Genome
970 Biol. *20*, 277. https://doi.org/10.1186/s13059-019-1911-0.

971 126. de Sotero-Caio, C.G., Cabral-de-Mello, D.C., Calixto, M. da S., Valente, G.T., Martins, C.,
972 Loreto, V., de Souza, M.J., and Santos, N. (2017). Centromeric enrichment of LINE-1

973 retrotransposons and its significance for the chromosome evolution of Phyllostomid bats.
974 Chromosome Res. *25*, 313–325. https://doi.org/10.1007/s10577-017-9565-9.

975 127. Kosek, D., Grabundzija, I., Lei, H., Bilic, I., Wang, H., Jin, Y., Peaslee, G.F., Hickman, A.B.,
976 and Dyda, F. (2021). The large bat Helitron DNA transposase forms a compact monomeric
977 assembly that buries and protects its covalently bound 5'-transposon end. Mol. Cell *81*,
978 4271–4286.e4. https://doi.org/10.1016/j.molcel.2021.07.028.

979 128. Ducani, C., Bernardinelli, G., and Högberg, B. (2014). Rolling circle replication requires
980 single-stranded DNA binding protein to avoid termination and production of double-
981 stranded DNA. Nucleic Acids Res. *42*, 10596–10604. https://doi.org/10.1093/nar/gku737.

982 129. Thomas, J., Phillips, C.D., Baker, R.J., and Pritham, E.J. (2014). Rolling-circle transposons
983 catalyze genomic innovation in a mammalian lineage. Genome Biol. Evol. *6*, 2595–2610.
984 https://doi.org/10.1093/gbe/evu204.

985 130. Balachandran, P., Walawalkar, I.A., Flores, J.I., Dayton, J.N., Audano, P.A., and Beck, C.R.
986 (2022). Transposable element-mediated rearrangements are prevalent in human genomes.
987 Nat. Commun. *13*, 7115. https://doi.org/10.1038/s41467-022-34810-8.

988 131. Ait Saada, A., Guo, W., Costa, A.B., Yang, J., Wang, J., and Lobachev, K.S. (2023). Widely
989 spaced and divergent inverted repeats become a potent source of chromosomal
990 rearrangements in long single-stranded DNA regions. Nucleic Acids Res. *51*, 3722–3734.
991 https://doi.org/10.1093/nar/gkad153.

992 132. Kondrashov, F.A. (2011). Gene Dosage and Duplication. In Evolution after Gene
993 Duplication, K. Dittmar and D. Liberles, eds. (John Wiley & Sons), pp. 57–76.

994 133. Kondrashov, F.A., Rogozin, I.B., Wolf, Y.I., and Koonin, E.V. (2002). Selection in the
995 evolution of gene duplications. Genome Biol. *3*, RESEARCH0008.
996 https://doi.org/10.1186/gb-2002-3-2-research0008.

997 134. Rastogi, S., and Liberles, D.A. (2005). Subfunctionalization of duplicated genes as a
998 transition state to neofunctionalization. BMC Evol. Biol. *5*, 28. https://doi.org/10.1186/1471-
999 2148-5-28.

1000 135. Assis, R., and Bachtrog, D. (2013). Neofunctionalization of young duplicate genes in
1001 Drosophila. Proc. Natl. Acad. Sci. U. S. A. *110*, 17409–17414.
1002 https://doi.org/10.1073/pnas.1313759110.

1003 136. Tirosh, I., and Barkai, N. (2007). Comparative analysis indicates regulatory
1004 neofunctionalization of yeast duplicates. Genome Biol. *8*, R50. https://doi.org/10.1186/gb-
1005 2007-8-4-r50.

1006 137. Mendes, F.K., Vanderpool, D., Fulton, B., and Hahn, M.W. (2021). CAFE 5 models
1007 variation in evolutionary rates among gene families. Bioinformatics *36*, 5516–5518.
1008 https://doi.org/10.1093/bioinformatics/btaa1022.

1009 138. Duan, S., Moro, L., Qu, R., Simoneschi, D., Cho, H., Jiang, S., Zhao, H., Chang, Q., de
1010 Stanchina, E., Arbini, A.A., et al. (2021). Loss of FBXO31-mediated degradation of DUSP6
1011 dysregulates ERK and PI3K-AKT signaling and promotes prostate tumorigenesis. Cell Rep.
1012 *37*, 109870. https://doi.org/10.1016/j.celrep.2021.109870.

1013 139. Morel, B., Kozlov, A.M., Stamatakis, A., and Szöllősi, G.J. (2020). GeneRax: A Tool for
1014 Species-Tree-Aware Maximum Likelihood-Based Gene Family Tree Inference under Gene
1015 Duplication, Transfer, and Loss. Mol. Biol. Evol. *37*, 2763–2774.
1016 https://doi.org/10.1093/molbev/msaa141.

1017 140. Kaufman, R.J. (1999). Double-stranded RNA-activated protein kinase mediates virus-
1018 induced apoptosis: a new role for an old actor. Proc. Natl. Acad. Sci. U. S. A. *96*, 11693–
1019 11695. https://doi.org/10.1073/pnas.96.21.11693.

1020 141. García, M.A., Gil, J., Ventoso, I., Guerra, S., Domingo, E., Rivas, C., and Esteban, M.
1021 (2006). Impact of protein kinase PKR in cell biology: from antiviral to antiproliferative action.
1022 Microbiol. Mol. Biol. Rev. *70*, 1032–1060. https://doi.org/10.1128/MMBR.00027-06.

1023 142. Ostertag, D., Hoblitzell-Ostertag, T.M., and Perrault, J. (2007). Overproduction of double-
1024 stranded RNA in vesicular stomatitis virus-infected cells activates a constitutive cell-type-
1025 specific antiviral response. J. Virol. *81*, 503–513. https://doi.org/10.1128/JVI.01218-06.

1026 143. Lagunas-Rangel, F.A. (2020). Why do bats live so long?—Possible molecular mechanisms.
1027 Biogerontology *21*, 1–11. https://doi.org/10.1007/s10522-019-09840-3.

1028 144. Chionh, Y.T., Cui, J., Koh, J., Mendenhall, I.H., Ng, J.H.J., Low, D., Itahana, K., Irving, A.T.,
1029 and Wang, L.-F. (2019). High basal heat-shock protein expression in bats confers
1030 resistance to cellular heat/oxidative stress. Cell Stress Chaperones *24*, 835–849.
1031 https://doi.org/10.1007/s12192-019-01013-y.

1032 145. Hua, R., Ma, Y.-S., Yang, L., Hao, J.-J., Hua, Q.-Y., Shi, L.-Y., Yao, X.-Q., Zhi, H.-Y., and
1033 Liu, Z. (2024). Experimental evidence for cancer resistance in a bat species. Nat. Commun.
1034 *15*, 1401. https://doi.org/10.1038/s41467-024-45767-1.

1035 146. Peixoto, F.P., Braga, P.H.P., and Mendes, P. (2018). A synthesis of ecological and
1036 evolutionary determinants of bat diversity across spatial scales. BMC Ecol. *18*, 18.
1037 https://doi.org/10.1186/s12898-018-0174-z.

1038 147. USGS (2022). North American Bat Ranges.
1039 http://dds.cr.usgs.gov/pub/data/nationalatlas/bat000p010g_nt00373.tar.gz
1040 http://dds.cr.usgs.gov/pub/data/nationalatlas/bat000p010g_nt00373.tar.gz.

1041 148. Rhie, A., McCarthy, S.A., Fedrigo, O., Damas, J., Formenti, G., Koren, S., Uliano-Silva, M.,
1042 Chow, W., Fungtammasan, A., Kim, J., et al. (2021). Towards complete and error-free
1043 genome assemblies of all vertebrate species. Nature *592*, 737–746.
1044 https://doi.org/10.1038/s41586-021-03451-0.

1045 149. The Darwin Tree of Life Project Consortium (2022). Sequence Locally, Think Globally: The
1046 Darwin Tree of Life Project. Proceedings of the National Academy of Sciences *119*,
1047 e2115642118. https://doi.org/10.1073/pnas.2115642118.

1048 150. Lewin, H.A., Richards, S., Lieberman Aiden, E., Allende, M.L., Archibald, J.M., Bálint, M.,
1049 Barker, K.B., Baumgartner, B., Belov, K., Bertorelle, G., et al. (2022). The Earth
1050 BioGenome Project 2020: Starting the Clock. Proceedings of the National Academy of
1051 Sciences *119*, e2115635118. https://doi.org/10.1073/pnas.2115635118.

1052 151. Tacutu, R., Thornton, D., Johnson, E., Budovsky, A., Barardo, D., Craig, T., Diana, E.,

1053 Lehmann, G., Toren, D., Wang, J., et al. (2018). Human Ageing Genomic Resources: new
1054 and updated databases. Nucleic Acids Res. *46*, D1083–D1090.
1055 https://doi.org/10.1093/nar/gkx1042.

1056 152. Enard, D., and Petrov, D.A. (2020). Ancient RNA virus epidemics through the lens of recent
1057 adaptation in human genomes. Philos. Trans. R. Soc. Lond. B Biol. Sci. *375*, 20190575.
1058 https://doi.org/10.1098/rstb.2019.0575.

1059 153. Boys, I.N., Xu, E., Mar, K.B., De La Cruz-Rivera, P.C., Eitson, J.L., Moon, B., and
1060 Schoggins, J.W. (2020). RTP4 is a potent IFN-inducible anti-flavivirus effector engaged in a
1061 host-virus arms race in bats and other mammals. Cell Host Microbe *28*, 712–723.e9.
1062 https://doi.org/10.1016/j.chom.2020.09.014.

1063 154. Lytras, S., Wickenhagen, A., Sugrue, E., Stewart, D.G., Swingler, S., Sims, A., Jackson
1064 Ireland, H., Davies, E.L., Ludlam, E.M., Li, Z., et al. (2023). Resurrection of 2'-5'-
1065 oligoadenylate synthetase 1 (OAS1) from the ancestor of modern horseshoe bats blocks
1066 SARS-CoV-2 replication. PLoS Biol. *21*, e3002398.
1067 https://doi.org/10.1371/journal.pbio.3002398.

1068 155. Tsagkogeorga, G., Müller, S., Dessimoz, C., and Rossiter, S.J. (2017). Comparative
1069 genomics reveals contraction in olfactory receptor genes in bats. Sci. Rep. *7*, 259.
1070 https://doi.org/10.1038/s41598-017-00132-9.

1071 156. Gutiérrez-Guerrero, Y.T., Ibarra-Laclette, E., Martínez Del Río, C., Barrera-Redondo, J.,
1072 Rebollar, E.A., Ortega, J., León-Paniagua, L., Urrutia, A., Aguirre-Planter, E., and Eguiarte,
1073 L.E. (2020). Genomic consequences of dietary diversification and parallel evolution due to
1074 nectarivory in leaf-nosed bats. Gigascience *9*. https://doi.org/10.1093/gigascience/giaa059.

1075 157. Xie, S.S., Huang, C.H., Reid, M.E., Blancher, A., and Blumenfeld, O.O. (1997). The
1076 glycophorin A gene family in gorillas: structure, expression, and comparison with the human
1077 and chimpanzee homologues. Biochem. Genet. *35*, 59–76.
1078 https://doi.org/10.1023/a:1022212630370.

1079 158. Gustavsson, E.K., Sethi, S., Gao, Y., Brenton, J.W., García-Ruiz, S., Zhang, D., Garza, R.,
1080 Reynolds, R.H., Evans, J.R., Chen, Z., et al. (2024). The annotation of GBA1 has been
1081 concealed by its protein-coding pseudogene GBAP1. Sci. Adv. *10*, eadk1296.
1082 https://doi.org/10.1126/sciadv.adk1296.

1083 159. O'Shea, T.J., Cryan, P.M., Cunningham, A.A., Fooks, A.R., Hayman, D.T.S., Luis, A.D.,
1084 Peel, A.J., Plowright, R.K., and Wood, J.L.N. (2014). Bat flight and zoonotic viruses. Emerg.
1085 Infect. Dis. *20*, 741–745. https://doi.org/10.3201/eid2005.130539.

1086 160. Levesque, D.L., Boyles, J.G., Downs, C.J., and Breit, A.M. (2021). High Body Temperature
1087 is an Unlikely Cause of High Viral Tolerance in Bats. J. Wildl. Dis. *57*, 238–241.
1088 https://doi.org/10.7589/JWD-D-20-00079.

1089 161. Kirkwood, T.B.L. (2017). The disposable soma theory. The evolution of senescence in the
1090 tree of life, 23–39.

1091 162. Toshkova, N., Zhelyzkova, V., Reyes-Ruiz, A., Haerens, E., de Castro Deus, M., Lacombe,
1092 R.V., Lecerf, M., Gonzalez, G., Jouvenet, N., Planchais, C., et al. (2024). Temperature
1093 sensitivity of bat antibodies links metabolic state of bats with antigen-recognition diversity.

1094 Nat. Commun. *15*, 5878. https://doi.org/10.1038/s41467-024-50316-x.

1095 163. Mandl, J.N., Schneider, C., Schneider, D.S., and Baker, M.L. (2018). Going to bat(s) for
1096 studies of disease tolerance. Front. Immunol. *9*, 2112.
1097 https://doi.org/10.3389/fimmu.2018.02112.

1098 164. Pei, G., Balkema-Buschmann, A., and Dorhoi, A. (2024). Disease tolerance as immune
1099 defense strategy in bats: One size fits all? PLoS Pathog. *20*, e1012471.
1100 https://doi.org/10.1371/journal.ppat.1012471.

1101 165. Vermillion, K.L., Anderson, K.J., Hampton, M., and Andrews, M.T. (2015). Gene expression
1102 changes controlling distinct adaptations in the heart and skeletal muscle of a hibernating
1103 mammal. Physiol. Genomics *47*, 58–74.
1104 https://doi.org/10.1152/physiolgenomics.00108.2014.

1105 166. Lam, B., Kajderowicz, K.M., Keys, H.R., Roessler, J.M., Frenkel, E.M., Kirkland, A., Bisht,
1106 P., El-Brolosy, M.A., Jaenisch, R., Bell, G.W., et al. (2024). Multi-species genome-wide
1107 CRISPR screens identify GPX4 as a conserved suppressor of cold-induced cell death.
1108 bioRxivorg, 2024.07.25.605098. https://doi.org/10.1101/2024.07.25.605098.

1109 167. Sone, M., and Yamaguchi, Y. (2024). Cold resistance of mammalian hibernators ~ a matter
1110 of ferroptosis? Front. Physiol. *15*, 1377986. https://doi.org/10.3389/fphys.2024.1377986.

1111 168. Kaelber, J.T., Demogines, A., Harbison, C.E., Allison, A.B., Goodman, L.B., Ortega, A.N.,
1112 Sawyer, S.L., and Parrish, C.R. (2012). Evolutionary reconstructions of the transferrin
1113 receptor of Caniforms supports canine parvovirus being a re-emerged and not a novel
1114 pathogen in dogs. PLoS Pathog. *8*, e1002666.
1115 https://doi.org/10.1371/journal.ppat.1002666.

1116 169. Demogines, A., Abraham, J., Choe, H., Farzan, M., and Sawyer, S.L. (2013). Dual host-
1117 virus arms races shape an essential housekeeping protein. PLoS Biol. *11*, e1001571.
1118 https://doi.org/10.1371/journal.pbio.1001571.

1119 170. Kerr, S.A., Jackson, E.L., Lungu, O.I., Meyer, A.G., Demogines, A., Ellington, A.D.,
1120 Georgiou, G., Wilke, C.O., and Sawyer, S.L. (2015). Computational and functional analysis
1121 of the virus-receptor interface reveals host range trade-offs in New World arenaviruses. J.
1122 Virol. *89*, 11643–11653. https://doi.org/10.1128/JVI.01408-15.

1123 171. Kaur, H., Kalayjian, R., Wu, K., Tassiopoulos, K., Palella, F., Taiwo, B., Bush, W., Hileman,
1124 C., Bedimo, R., Koletar, S., et al. (2022). Associations of L-Ferritin and Tim-1 with frailty
1125 measures in people with HIV: a cross-sectional and longitudinal study. Lancet Healthy
1126 Longev. *3*, S5. https://doi.org/10.1016/s2666-7568(22)00066-6.

1127 172. Kim, J., Jo, Y., Cho, D., and Ryu, D. (2022). L-threonine promotes healthspan by expediting
1128 ferritin-dependent ferroptosis inhibition in C. elegans. Nat. Commun. *13*, 6554.
1129 https://doi.org/10.1038/s41467-022-34265-x.

1130 173. Daghlas, I., and Gill, D. (2021). Genetically predicted iron status and life expectancy. Clin.
1131 Nutr. *40*, 2456–2459. https://doi.org/10.1016/j.clnu.2020.06.025.

1132 174. Perez, K., Ciotlos, S., McGirr, J., Limbad, C., Doi, R., Nederveen, J.P., Nilsson, M.I., Winer,
1133 D.A., Evans, W., Tarnopolsky, M., et al. (2022). Single nuclei profiling identifies cell specific

1134 markers of skeletal muscle aging, frailty, and senescence. Aging (Albany NY) *14*, 9393–
1135 9422. https://doi.org/10.18632/aging.204435.

1136 175. Trifunovic, A., Wredenberg, A., Falkenberg, M., Spelbrink, J.N., Rovio, A.T., Bruder, C.E.,
1137 Bohlooly-Y, M., Gidlöf, S., Oldfors, A., Wibom, R., et al. (2004). Premature ageing in mice
1138 expressing defective mitochondrial DNA polymerase. Nature *429*, 417–423.
1139 https://doi.org/10.1038/nature02517.

1140 176. Van Goethem, G., Dermaut, B., Löfgren, A., Martin, J.J., and Van Broeckhoven, C. (2001).
1141 Mutation of POLG is associated with progressive external ophthalmoplegia characterized
1142 by mtDNA deletions. Nat. Genet. *28*, 211–212. https://doi.org/10.1038/90034.

1143 177. Cao, L., Li, W., Kim, S., Brodie, S.G., and Deng, C.-X. (2003). Senescence, aging, and
1144 malignant transformation mediated by p53 in mice lacking the Brca1 full-length isoform.
1145 Genes Dev. *17*, 201–213. https://doi.org/10.1101/gad.1050003.

1146 178. Vijg, J., Perls, T., Franceschi, C., and van Orsouw, N.J. (2001). BRCA1 gene sequence
1147 variation in centenarians. Ann. N. Y. Acad. Sci. *928*, 85–96. https://doi.org/10.1111/j.1749-
1148 6632.2001.tb05639.x.

1149 179. Fearon, E.R. (1997). Human cancer syndromes: clues to the origin and nature of cancer.
1150 Science *278*, 1043–1050. https://doi.org/10.1126/science.278.5340.1043.

1151 180. Donoho, G., Brenneman, M.A., Cui, T.X., Donoviel, D., Vogel, H., Goodwin, E.H., Chen,
1152 D.J., and Hasty, P. (2003). Deletion of Brca2 exon 27 causes hypersensitivity to DNA
1153 crosslinks, chromosomal instability, and reduced life span in mice. Genes Chromosomes
1154 Cancer *36*, 317–331. https://doi.org/10.1002/gcc.10148.

1155 181. Wooster, R., Bignell, G., Lancaster, J., Swift, S., Seal, S., Mangion, J., Collins, N., Gregory,
1156 S., Gumbs, C., and Micklem, G. (1995). Identification of the breast cancer susceptibility
1157 gene BRCA2. Nature *378*, 789–792. https://doi.org/10.1038/378789a0.

1158 182. Ray, D.A., Feschotte, C., Pagan, H.J.T., Smith, J.D., Pritham, E.J., Arensburger, P.,
1159 Atkinson, P.W., and Craig, N.L. (2008). Multiple Waves of Recent DNA Transposon Activity
1160 in the Bat, Myotis Lucifugus. Genome Res. *18*, 717–728.
1161 https://doi.org/10.1101/gr.071886.107.

1162 183. Sotgia, S., Zinellu, A., Mangoni, A.A., Serra, R., Pintus, G., Caruso, C., Deiana, L., and
1163 Carru, C. (2017). Cellular immune activation in Sardinian middle-aged, older adults and
1164 centenarians. Exp. Gerontol. *99*, 133–137. https://doi.org/10.1016/j.exger.2017.10.005.

1165 184. Lee, K.-A., Flores, R.R., Jang, I.H., Saathoff, A., and Robbins, P.D. (2022). Immune
1166 senescence, immunosenescence and aging. Front. Aging *3*, 900028.
1167 https://doi.org/10.3389/fragi.2022.900028.

1168 185. Yousefzadeh, M.J., Flores, R.R., Zhu, Y., Schmiechen, Z.C., Brooks, R.W., Trussoni, C.E.,
1169 Cui, Y., Angelini, L., Lee, K.-A., McGowan, S.J., et al. (2021). An aged immune system
1170 drives senescence and ageing of solid organs. Nature *594*, 100–105.
1171 https://doi.org/10.1038/s41586-021-03547-7.

1172 186. Lee, C.-S., Chang, C.-H., Chen, C.-Y., Shih, C.-Y., Peng, J.-K., Huang, H.-L., Chen, P.-Y.,
1173 Huang, T.-L., Chen, C.-Y., and Tsai, J.-S. (2022). Upregulation of cluster of differentiation

1174 36 mRNA expression in peripheral blood mononuclear cells correlates with frailty severity in
1175 older adults. J. Cachexia Sarcopenia Muscle *13*, 1948–1955.
1176 https://doi.org/10.1002/jcsm.13003.

1177 187. Kimmel, J.C., Yi, N., Roy, M., Hendrickson, D.G., and Kelley, D.R. (2021). Differentiation
1178 reveals latent features of aging and an energy barrier in murine myogenesis. Cell Rep. *35*,
1179 109046. https://doi.org/10.1016/j.celrep.2021.109046.

1180 188. Tian, Y., Lu, J., Hao, X., Li, H., Zhang, G., Liu, X., Li, X., Zhao, C., Kuang, W., Chen, D., et
1181 al. (2020). FTH1 inhibits ferroptosis through ferritinophagy in the 6-OHDA model of
1182 Parkinson's disease. Neurotherapeutics *17*, 1796–1812. https://doi.org/10.1007/s13311-
1183 020-00929-z.

1184 189. Jonathan Sleeman, Center Director, USGS National Wildlife Health Center (2020). NWHC
1185 Operations During the COVID-19 Pandemic and Information About Coronaviruses in
1186 Wildlife.

1187 190. White-Nose Syndrome Disease Management Working Group National White-Nose
1188 Syndrome Decontamination Protocol.

1189 191. Dudchenko, O., Batra, S.S., Omer, A.D., Nyquist, S.K., Hoeger, M., Durand, N.C., Shamim,
1190 M.S., Machol, I., Lander, E.S., Aiden, A.P., et al. (2017). De novo assembly of the Aedes
1191 aegypti genome using Hi-C yields chromosome-length scaffolds. Science *356*, 92–95.
1192 https://doi.org/10.1126/science.aal3327.

1193 192. Lindblad-Toh, K., Garber, M., Zuk, O., Lin, M.F., Parker, B.J., Washietl, S., Kheradpour, P.,
1194 Ernst, J., Jordan, G., Mauceli, E., et al. (2011). A high-resolution map of human
1195 evolutionary constraint using 29 mammals. Nature *478*, 476–482.
1196 https://doi.org/10.1038/nature10530.

1197 193. Bolger, A.M., Lohse, M., and Usadel, B. (2014). Trimmomatic: a flexible trimmer for Illumina
1198 sequence data. Bioinformatics *30*, 2114–2120.
1199 https://doi.org/10.1093/bioinformatics/btu170.

1200 194. Cheng, H., Concepcion, G.T., Feng, X., Zhang, H., and Li, H. (2021). Haplotype-resolved
1201 de novo assembly using phased assembly graphs with hifiasm. Nat. Methods *18*, 170–175.
1202 https://doi.org/10.1038/s41592-020-01056-5.

1203 195. Cheng, H., Jarvis, E.D., Fedrigo, O., Koepfli, K.-P., Urban, L., Gemmell, N.J., and Li, H.
1204 (2022). Haplotype-resolved assembly of diploid genomes without parental data. Nat.
1205 Biotechnol. *40*, 1332–1335. https://doi.org/10.1038/s41587-022-01261-x.

1206 196. Zhou, C., McCarthy, S.A., and Durbin, R. (2023). YaHS: yet another Hi-C scaffolding tool.
1207 Bioinformatics *39*. https://doi.org/10.1093/bioinformatics/btac808.

1208 197. Li, H., and Durbin, R. (2009). Fast and accurate short read alignment with Burrows-Wheeler
1209 transform. Bioinformatics *25*, 1754–1760. https://doi.org/10.1093/bioinformatics/btp324.

1210 198. Li, H., and Durbin, R. (2010). Fast and accurate long-read alignment with Burrows-Wheeler
1211 transform. Bioinformatics *26*, 589–595. https://doi.org/10.1093/bioinformatics/btp698.

1212 199. Open2C, Abdennur, N., Fudenberg, G., Flyamer, I.M., Galitsyna, A.A., Goloborodko, A.,

1213 Imakaev, M., and Venev, S.V. (2024). Pairtools: From sequencing data to chromosome
1214 contacts. PLoS Comput. Biol. *20*, e1012164. https://doi.org/10.1371/journal.pcbi.1012164.

1215 200. Danecek, P., Bonfield, J.K., Liddle, J., Marshall, J., Ohan, V., Pollard, M.O., Whitwham, A.,
1216 Keane, T., McCarthy, S.A., Davies, R.M., et al. (2021). Twelve years of SAMtools and
1217 BCFtools. Gigascience *10*. https://doi.org/10.1093/gigascience/giab008.

1218 201. Harry, E. (2022). PretextView (Paired REad TEXTure Viewer): A desktop application for
1219 viewing pretext contact maps.

1220 202. Rapid curation GitLab. https://gitlab.com/wtsi-grit/rapid-curation.

1221 203. Uliano-Silva, M., Ferreira, J.G.R.N., Krasheninnikova, K., Darwin Tree of Life Consortium,
1222 Formenti, G., Abueg, L., Torrance, J., Myers, E.W., Durbin, R., Blaxter, M., et al. (2023).
1223 MitoHiFi: a python pipeline for mitochondrial genome assembly from PacBio high fidelity
1224 reads. BMC Bioinformatics *24*, 288. https://doi.org/10.1186/s12859-023-05385-y.

1225 204. Palmer, J.M., and Stajich, J.E. (2023). funannotate: Eukaryotic Genome Annotation
1226 Pipeline (Github).

1227 205. Smit, A.F.A., Hubley, R., and Green, P. (2015). RepeatMasker Open-4.0. 2013--2015.
1228 Preprint at Seattle, USA.

1229 206. Zoonomia Consortium (2020). A comparative genomics multitool for scientific discovery and
1230 conservation. Nature *587*, 240–245. https://doi.org/10.1038/s41586-020-2876-6.

1231 207. Flynn, J.M., Hubley, R., Goubert, C., Rosen, J., Clark, A.G., Feschotte, C., and Smit, A.F.
1232 (2020). RepeatModeler2 for automated genomic discovery of transposable element
1233 families. Proc. Natl. Acad. Sci. U. S. A. *117*, 9451–9457.
1234 https://doi.org/10.1073/pnas.1921046117.

1235 208. Išerić, H., Alkan, C., Hach, F., and Numanagić, I. (2022). Fast characterization of
1236 segmental duplication structure in multiple genome assemblies. Algorithms Mol. Biol.

1237 209. Brown, M., González De la Rosa, P.M., and Mark, B. (2023). A Telomere Identification
1238 Toolkit https://doi.org/10.5281/zenodo.10091385.

1239 210. Li, H. (2021). New strategies to improve minimap2 alignment accuracy. Bioinformatics.

1240 211. Goel, M., and Schneeberger, K. (2022). plotsr: visualizing structural similarities and
1241 rearrangements between multiple genomes. Bioinformatics *38*, 2922–2926.
1242 https://doi.org/10.1093/bioinformatics/btac196.

1243 212. Palmer, J.M., and Stajich, J. (2020). Funannotate v1.8.1: Eukaryotic genome annotation
1244 (Zenodo) https://doi.org/10.5281/ZENODO.4054262.

1245 213. Leinonen, R., Diez, F.G., Binns, D., Fleischmann, W., Lopez, R., and Apweiler, R. (2004).
1246 UniProt archive. Bioinformatics *20*, 3236–3237.
1247 https://doi.org/10.1093/bioinformatics/bth191.

1248 214. Haas, B.J., Papanicolaou, A., Yassour, M., Grabherr, M., Blood, P.D., Bowden, J., and
1249 Others (2013). De novo transcript sequence reconstruction from RNA Seq: reference
1250 generation and analysis with Trinity. Nat Protol. 2013; 8 (8): 1494--512. Preprint.

1251 215. Korf, I. (2004). Gene finding in novel genomes. BMC Bioinformatics *5*, 59.
1252 https://doi.org/10.1186/1471-2105-5-59.

1253 216. Majoros, W.H., Pertea, M., and Salzberg, S.L. (2004). TigrScan and GlimmerHMM: two
1254 open source ab initio eukaryotic gene-finders. Bioinformatics *20*, 2878–2879.
1255 https://doi.org/10.1093/bioinformatics/bth315.

1256 217. Stanke, M., Keller, O., Gunduz, I., Hayes, A., Waack, S., and Morgenstern, B. (2006).
1257 AUGUSTUS: ab initio prediction of alternative transcripts. Nucleic Acids Res. *34*, W435–
1258 W439. https://doi.org/10.1093/nar/gkl200.

1259 218. Haas, B.J., Salzberg, S.L., Zhu, W., Pertea, M., and Allen, J.E. (2008). Automated
1260 eukaryotic gene structure annotation using EVidenceModeler and the Program to Assemble
1261 Spliced Alignments. Genome Biol.

1262 219. Quintaje, S.B., and Orchard, S. (2008). The annotation of both human and mouse kinomes
1263 in UniProtKB/Swiss-Prot: one small step in manual annotation, one giant leap for full
1264 comprehension of genomes. Mol. Cell. Proteomics.

1265 220. Buchfink, B., Reuter, K., and Drost, H.-G. (2021). Sensitive protein alignments at tree-of-life
1266 scale using DIAMOND. Nat. Methods *18*, 366–368. https://doi.org/10.1038/s41592-021-
1267 01101-x.

1268 221. Emms, D.M., and Kelly, S. (2019). OrthoFinder: phylogenetic orthology inference for
1269 comparative genomics. Genome Biol. *20*, 238. https://doi.org/10.1186/s13059-019-1832-y.

1270 222. Ranwez, V., Douzery, E.J.P., Cambon, C., Chantret, N., and Delsuc, F. (2018). MACSE v2:
1271 Toolkit for the Alignment of Coding Sequences Accounting for Frameshifts and Stop
1272 Codons. Mol. Biol. Evol. *35*, 2582–2584. https://doi.org/10.1093/molbev/msy159.

1273 223. Whelan, S., Irisarri, I., and Burki, F. (2018). PREQUAL: detecting non-homologous
1274 characters in sets of unaligned homologous sequences. Bioinformatics *34*, 3929–3930.
1275 https://doi.org/10.1093/bioinformatics/bty448.

1276 224. Bowman, J., Silva, N., Schüueftan, E., Almeida, J.M., Brattig-Correia, R., Oliveira, R.A.,
1277 Tüttelmann, F., Enard, D., Navarro-Costa, P., and Lynch, V.J. (2023). Pervasive relaxed
1278 selection on spermatogenesis genes coincident with the evolution of polygyny in gorillas.
1279 bioRxiv, 2023.10.27.564379. https://doi.org/10.1101/2023.10.27.564379.

1280 225. Scornavacca, C., Belkhir, K., Lopez, J., Dernat, R., Delsuc, F., Douzery, E.J.P., and
1281 Ranwez, V. (2019). OrthoMaM v10: Scaling-Up Orthologous Coding Sequence and Exon
1282 Alignments with More than One Hundred Mammalian Genomes. Mol. Biol. Evol. *36*, 861–
1283 862. https://doi.org/10.1093/molbev/msz015.

1284 226. Cunningham, F., Allen, J.E., Allen, J., Alvarez-Jarreta, J., Amode, M.R., Armean, I.M.,
1285 Austine-Orimoloye, O., Azov, A.G., Barnes, I., Bennett, R., et al. (2022). Ensembl 2022.
1286 Nucleic Acids Res. *50*, D988–D995. https://doi.org/10.1093/nar/gkab1049.

1287 227. Minh, B.Q., Schmidt, H.A., Chernomor, O., Schrempf, D., Woodhams, M.D., von Haeseler,
1288 A., and Lanfear, R. (2020). IQ-TREE 2: New Models and Efficient Methods for Phylogenetic
1289 Inference in the Genomic Era. Mol. Biol. Evol. *37*, 1530–1534.
1290 https://doi.org/10.1093/molbev/msaa015.

1291 228. Dos Reis, M., and Yang, Z. (2019). Bayesian Molecular Clock Dating Using Genome-Scale
1292 Datasets. Methods Mol. Biol. *1910*, 309–330. https://doi.org/10.1007/978-1-4939-9074-
1293 0_10.

1294 229. Yang, Z. (2007). PAML 4: phylogenetic analysis by maximum likelihood. Mol. Biol. Evol. *24*,
1295 1586–1591. https://doi.org/10.1093/molbev/msm088.

1296 230. Phillips, M.J. (2016). Geomolecular dating and the origin of placental mammals. Syst. Biol.
1297 *65*, 546–557. https://doi.org/10.1093/sysbio/syv115.

1298 231. Gunnell, G.F., and Simmons, N.B. (2005). Fossil evidence and the origin of bats. J. Mamm.
1299 Evol. *12*, 209–246. https://doi.org/10.1007/s10914-005-6945-2.

1300 232. Eiting, T.P., and Gunnell, G.F. (2009). Global Completeness of the Bat Fossil Record. J.
1301 Mamm. Evol. *16*, 151–173. https://doi.org/10.1007/s10914-009-9118-x.

1302 233. Storch, G., Sigé, B., and Habersetzer, J. (2002). Tachypteron franzeni n. gen., n. sp.,
1303 earliest emballonurid bat from the Middle Eocene of Messel (Mammalia, Chiroptera).
1304 Palaontol. Z. *76*, 189–199. https://doi.org/10.1007/bf02989856.

1305 234. Ravel, A., Marivaux, L., Tabuce, R., Ben Haj Ali, M., Essid, E.L.M., and Vianey-Liaud, M.
1306 (2012). A new large philisid (Mammalia, Chiroptera, Vespertilionoidea) from the late Early
1307 Eocene of Chambi, Tunisia: LARGE BAT FROM CHAMBI. Palaeontology *55*, 1035–1041.
1308 https://doi.org/10.1111/j.1475-4983.2012.01160.x.

1309 235. Lim, B.K. (2009). Review of the origins and biogeography of bats in South America.
1310 Chiroptera Neotropical *15*, 391–410.

1311 236. Morgan, G.S., and Czaplewski, N.J. (2003). A New Bat (Chiroptera: Natalidae) from the
1312 Early Miocene of Florida, with Comments on Natalid Phylogeny. J Mammal *84*, 729–752.
1313 https://doi.org/10.1644/1545-1542(2003)084<0729:ANBCNF>2.0.CO;2.

1314 237. Foley, N.M., Mason, V.C., Harris, A.J., Bredemeyer, K.R., Damas, J., Lewin, H.A., Eizirik,
1315 E., Gatesy, J., Karlsson, E.K., Lindblad-Toh, K., et al. (2023). A genomic timescale for
1316 placental mammal evolution. Science *380*, eabl8189.
1317 https://doi.org/10.1126/science.abl8189.

1318 238. Elliot, M.G., and Mooers, A.Ø. (2014). Inferring ancestral states without assuming neutrality
1319 or gradualism using a stable model of continuous character evolution. BMC Evol. Biol. *14*,
1320 226. https://doi.org/10.1186/s12862-014-0226-8.

1321 239. Kosakovsky Pond, S.L., Poon, A.F.Y., Velazquez, R., Weaver, S., Hepler, N.L., Murrell, B.,
1322 Shank, S.D., Magalis, B.R., Bouvier, D., Nekrutenko, A., et al. (2020). HyPhy 2.5-A
1323 customizable platform for evolutionary hypothesis testing using PHYlogenies. Mol. Biol.
1324 Evol. *37*, 295–299. https://doi.org/10.1093/molbev/msz197.

1325 240. Lucaci, A.G., Zehr, J.D., Enard, D., Thornton, J.W., and Kosakovsky Pond, S.L. (2023).
1326 Evolutionary Shortcuts via Multinucleotide Substitutions and Their Impact on Natural
1327 Selection Analyses. Mol. Biol. Evol. *40*. https://doi.org/10.1093/molbev/msad150.

1328 241. Wu, N., Nguyen, X.-N., Wang, L., Appourchaux, R., Zhang, C., Panthu, B., Gruffat, H.,
1329 Journo, C., Alais, S., Qin, J., et al. (2019). The interferon stimulated gene 20 protein

(ISG20) is an innate defense antiviral factor that discriminates self versus non-self translation. PLoS Pathog. *15*. https://doi.org/10.1371/journal.ppat.1008093.

242. GTEx Consortium (2020). The GTEx Consortium atlas of genetic regulatory effects across human tissues. Science *369*, 1318–1330. https://doi.org/10.1126/science.aaz1776.

243. Luisi, P., Alvarez-Ponce, D., Pybus, M., Fares, M.A., Bertranpetit, J., and Laayouni, H. (2015). Recent positive selection has acted on genes encoding proteins with more interactions within the whole human interactome. Genome Biol. Evol. *7*, 1141–1154. https://doi.org/10.1093/gbe/evv055.

244. Gene Ontology Consortium (2021). The Gene Ontology resource: enriching a GOld mine. Nucleic Acids Res. *49*, D325–D334. https://doi.org/10.1093/nar/gkaa1113.

245. Eisenberg, E., and Levanon, E.Y. (2013). Human housekeeping genes, revisited. Trends Genet. *29*, 569–574. https://doi.org/10.1016/j.tig.2013.05.010.

246. Kosakovsky Pond, S.L., Murrell, B., Fourment, M., Frost, S.D.W., Delport, W., and Scheffler, K. (2011). A random effects branch-site model for detecting episodic diversifying selection. Mol. Biol. Evol. *28*, 3033–3043. https://doi.org/10.1093/molbev/msr125.

247. Quinlan, A.R. (2014). BEDTools: The Swiss-Army Tool for Genome Feature Analysis. Curr. Protoc. Bioinformatics *47*, 11.12.1–34. https://doi.org/10.1002/0471250953.bi1112s47.

248. Dainat, J. AGAT: Another Gff Analysis Toolkit to handle annotations in any GTF/GFF format https://doi.org/10.5281/zenodo.3552717.

249. Legrand, A., Dahoui, C., De La Myre Mory, C., Noy, K., Guiguettaz, L., Versapuech, M., Loyer, C., Pillon, M., Wcislo, M., Guéguen, L., et al. (2024). SAMD9L acts as an antiviral factor against HIV-1 and primate lentiviruses by restricting viral and cellular translation. PLoS Biol. *22*, e3002696. https://doi.org/10.1371/journal.pbio.3002696.

Materials and Methods

Data availability

All sequencing data and genomes generated in this study are available on NCBI under Bioprojects PRJNA973719 and PRJNA1035541. Annotations generated in this study are available at https://github.com/docmanny/myotis-gene-annotations. All other code is available at https://github.com/sudmantlab/MyotisGenomeAssembly.

Sample collection and cell line derivation

All bats sampled for this study were wild caught under scientific collection permits for California and Arizona (see Supplemental Table 1). Bats were sampled using standard mist-netting procedures, including taking standard body measurements, following USGS recommendations for White-Nose Syndrome and COVID-19 prevention[189,190].

For *M. lucifugus*, the donor individual was field-caught in California and transported to the Genetics Laboratory of the California Department of Fish and Wildlife, where they were euthanized via isofluorane. The *M. velifer* individual was caught in Arizona and euthanized in the field via isoflurane. For both *M. lucifugus* and *M. velifer*, tissues were collected and preserved via flash-freezing in liquid nitrogen.

For *M. volans, M. occultus, M. auriculus,* and *M. californicus*, two 3-mm wing punch biopsies were taken from the left and right plagiopatagium of each donor individual and placed in a live cell collection media consisting of DMEM/F12 (Gibco) supplemented with 15mM HEPES (Gibco), 20% FBS (Gibco), and 0.2% Primocin (Invivogen) [@yohe2019; @curty2023; @capel2023]. Wing punches were then brought back to a cell culture facility in Berkeley, where they were used to generate cell lines as previously described[@yohe2019; @curty2023; @capel2023]. Additional cell lines for *M. lucifugus, M. velifer, M. yumanensis, M. evotis,* and *M. thysanodes* were similarly collected and generated.

Cell lines for the *M. evotis* and *M. thysanodes* genomes were generously provided by Richard Miller. Cell lines for functional work in *Rousettus langosus*, *Pteropus rodrigensis*, and *Eidolon helvum* were provided by the San Diego Frozen Zoo.

Sequencing and assembly

For 6 genomes (*M. evotis, M. thysanodes, M. volans, M. occultus, M. auriculus,* and *M. californicus*) DNA was extracted from primary cell lines expanded from 3M cells at Passage 2-4 to approximately 40M cells per line using a Circulomics BigDNA CCB kit following the UHMW protocol for cells. DNA from *M. lucifugus* was extracted from flash-frozen tissue by the Genetics Lab of the California Department of Fish and Wildlife. PacBio HiFi libraries were generated and sequenced on a Sequel II (PacBio) by the Functional Genomics Core at the University of California, Berkeley. For cell-line-derived genomes, Hi-C libraries for these genomes were generated from 1M cells at Passage 3 using the OmniC for Illumina kit (Dovetail genomics); libraries were submitted for quality control and sequencing on the Illumina NovaSeq platform (Novogene). For the *M. velifer* genomes, DNA was extracted from flash-frozen tissues, and all DNA extraction, library prep, and sequencing was completed by Dovetail Genomics following standard protocols. For *M. lucifugus*, a previously published Hi-C dataset from 4 pooled individuals was used for scaffolding[191,192].

The PacBio reads were processed using SMRTTools (v6.0.0-1, PacBio) to generate the circular consensus sequences using the settings --minPasses=3 --minRQ=0.99. Hi-C reads were processed using trimmomatic[193] (v0.35-6) to remove adapter sequences and low-quality bases using the settings ILLUMINACLIP:data/trimmomatic-adapters/TruSeq3-PE-2.fa:2:40:15 SLIDINGWINDOW:5:20. To generate the primary contig assemblies, we used hifiasm[194,195] (v0.14-hd174df1_0) in Hi-C mode, providing both the CCS reads and the trimmed Hi-C reads as input, and purging duplicates using the -l2 option. For our reference genomes, we proceeded with the primary contig assembly (*.asm.hic.p_ctg.gfa).

All reference genomes were scaffolded with YAHS[196] (v1.1a.1s) and the Hi-C datasets. Dovetail Omni-C data were processed and mapped to the genome following the manufacturer's instructions using bwa[197,198] (v0.7.17-h5bf99c6_8), pairtools[199] (v0.3.0-py37hb9c2fc3_5), and samtools[200] (v1.12-

1402 h9aed4be_1). YAHS was run using both default settings as well as with --no-contig-ec; after comparing
1403 the outputs, we proceeded with the --no-contig-ec version for our final assemblies.

1404 To finalize the assemblies, we performed manual curation using PreTextView[201] and the Rapid
1405 Curation toolkit[202] (version ff964069). The X chromosomes were identified based on size, synteny across
1406 genomes, and half-coverage observed in XY genomes; putative Y chromosomes were similarly identified
1407 in XY genomes. Mitochondrial genomes were identified and removed from the final assembly by running
1408 mitohifi[203] (v3.0) in contig mode on the assembly and removing all scaffolds identified as mitogenomes.
1409 The consensus mitogenome from mitohifi was designated as the representative mitogenome for the
1410 assembly after manual curation. Finally, to eliminate spurious duplicates, we used FunAnnotate[204]
1411 (v1.8.15) and the "clean" function to identify and remove any remaining scaffolds with 90% identical to a
1412 larger scaffold.

1413 Identification and annotation of repetitive elements

1414 We used RepeatMasker[205] (version 4.0.7-open) to annotate repetitive elements in our genomes.
1415 We first ran RepeatMasker using a curated database of transposable elements from 249 mammalian
1416 species[36,206] (David Ray, pers. comm.) and the settings "*-engine ncbi -s -noisy -xsmall*" followed by a
1417 second run using RepeatModeler[207] and RepeatMasker to identify *de novo* repeats missing from the
1418 curated database. All repeats were then soft-masked in all genomes. To assess the repeat landscape,
1419 we calculated the summary of divergence from the repeat alignments and created the repeat landscape
1420 using auxiliary RepeatMasker scripts (calcDivergenceFromAlign.pl & createRepeatLandscape.pl).

1421 Structural variation

1422 To understand the distribution of structural variants, including segmental duplication events, we
1423 used SyRI (Senteny and Rearrangement Identifier[125]) and BISER (Brisk Inference of Segmental
1424 duplication Evolutionary stRucture[208]). We first masked telomere regions using TIDK (Telomere
1425 Identification toolKit[209]), and mapped the primary 22 scaffolds of the nearctic *Myotis* genomes to each
1426 other with minimap2[210]. The scaffold corresponding to the X chromosome was omitted because there is
1427 no corresponding scaffold in the *M. yumanensis* assembly. To verify homologous chromosomes and fix
1428 strand orientation, we used *fixchr* from the SyRI package and manually renamed scaffolds accordingly,
1429 then re-mapped with minimap2. We ran SyRI on the resulting files and plotted the results with plotsr[211].
1430 We ran BISER on the primary 22 scaffolds of the nearctic *Myotis* genomes with –keep-contigs and default
1431 settings to generate bed files with the inferred segmental duplication regions.

1432 RNA-seq

1433 To assist our annotation efforts, we generated mRNA-seq for 7 of the species sequenced *de novo*
1434 in this study. For *M. velifer*, samples of heart, brain, kidneys, lungs, pancreas, and testis collected from
1435 the donor individual were provided to Dovetail Genomics (CA, USA) for mRNA-seq library preparation
1436 and sequencing. Using the same cell lines used for the genomes of *M. occultus, M. thysanodes, M.*

evotis, M. volans, M. auriculus, and *M. californicus*, we generated rRNA-depleted total RNA-seq libraries using the NEBNext rRNA Depletion Kit v2 and Ultra II Directional RNA Library Prep Kits. RNA and libraries were quality controlled on an Agillent Bioanalyzer using the RNA 6000 Nano and DNA High Sensitivity assays, respectively. Samples were sequenced on to 100M 150PE reads per sample using the Novoseq platform (Novogene). For *M. lucifugus*, we used the following published RNA-seq data on NCBI SRA generated using poly-A selection and paired-end sequencing: SRR6793287, SRR6793288, SRR6793289, SRR6793290, SRR6793291, SRR6793292, SRR6793293, SRR6793294, SRR6793295, SRR6793296, SRR6793297, SRR6793298, SRR6793299, SRR6793300, SRR6793301, SRR7064951, SRR10512805, SRR10512806, SRR10512807, SRR10512808, SRR10512809, SRR10512818, SRR10512829, SRR10512840, SRR10512845, SRR10512846, SRR10512847, SRR10512848, SRR10512849, SRR10512850, SRR10512851, SRR10512852, SRR10083333, SRR10083334, SRR10083335, SRR10083336, SRR10083337, SRR10083338, SRR10083339, SRR10083340, SRR10083351, SRR10083352, SRR1916825, SRR1916826, SRR1916827, SRR1916830, SRR1916832, SRR1916834, SRR1916836, SRR1916839, SRR1916841, SRR1916842, SRR18761564, SRR18761566, SRR18761568, SRR18761571, SRR18761573, SRR18761563, SRR18761565, SRR18761567, SRR18761569, SRR18761570, SRR18761572, SRR18761574, SRR1270869, SRR1270914, SRR1270919, SRR1270921, SRR1270922, SRR1270923, SRR4249979, SRR4249988, SRR5676382, SRR5676383, SRR5676395, SRR5676396, SRR5676402, SRR1869462, and SRR1013468.

Gene annotation and alignment

Gene predictions

To create optimal gene annotations, we combined *ab initio* gene predictions; orthology inferences; and transcriptomic evidence for a total-evidence dataset facilitated using FunAnnotate[204,212] with manual interventions. To generate high-quality orthology-based evidence, we downloaded the UNIPARC database[213] of genes present in all Chiropteran genomes and mapped these proteins to our genomes using miniprot[62] (v 0.6-r194-dirty). We assembled our transcriptome data into transcripts using TRINITY[214] (v 2.13.2), and mapped these transcripts to our genomes using minimap2[210] (v 2.24).

Next, we ran BUSCO[63,64] (version 5.4.3) using the “eutheria_odb10” database and AUGUSTUS[58] to identify BUSCO orthologs in our genomes. GFFs describing the gene structure of single-copy BUSCO orthologs was then used by FunAnnotate to train SNAP[215] and GlimmerHMM[216] (v 3.0.4) prior to gene prediction. GeneMark-ES[59] (v 4.72) was run using its self-trained model. AUGUSTUS[217] (v 3.4) was run using a previously-generated model jointly trained on 6 high-quality bat genome assemblies[36] and supplemented with protein and transcriptome hints generated by FunAnnotate from the UNIPARC and Trinity datasets.

To leverage high-quality annotations from other genomes, we used TOGA[61] (version 1.0.1) to generate gene annotations for each of our species, using inference from hg38 annotations. TOGA outputs a table of genes (“reg” genes) associated with the projected transcripts from the reference genomes, and a BED file describing the CDS structure of these projected transcripts. To generate a final

1475 GFF file summarizing these data, we converted the original BED file to a GFF file using [program];
1476 removed the erroneous "Gene" level attributes; and added in new "Gene" entries describing the TOGA-
1477 designated genes, modifying the "Parent" attributes of the mRNAs to refer to the correct parent gene.
1478 Transcript projections that were not associated with a TOGA gene designation were then dropped.

1479 Finally, we used LiftOff[60] (v1.6.3) to lift over annotations from the *Myotis myotis* genome
1480 (mMyoMyo1.0_primary[36]). Using BUSCO and manual curation, we assessed both the original GenBank
1481 (GCF_014108235.1) and NCBI RefSeq (GCA_014108235.1) annotations, and selected the NCBI
1482 RefSeq annotation, as it had slightly improved BUSCO scoring and less erroneous intron-exon junctions
1483 at select genes. We removed all non-protein-coding genes from the initial GFF file, then ran LiftOff using
1484 the settings " -exclude_partial -polish -cds".

1485 We evaluated each line of evidence by assessing their completeness using BUSCO and
1486 comparing the completeness score to the total number of predicted genes. We found that SNAP and
1487 GLIMMERHMM performed the poorest for gene annotations, with both the lowest BUSCO scores and
1488 the highest number of low-quality predictions. The miniprot-UniParc and TOGA-hg38 datasets generated
1489 the highest quality gene prediction datasets, with near-complete BUSCO scores and reduced low-quality
1490 protein predictions.

1491 Gene prediction curation

1492 We used EvidenceModeler[218] (version 2.0) to generate an initial consensus gene set using only
1493 the best lines of evidence (AUGUSTUS, weight 2; high quality AUGUSTUS, weight 5; TOGA-hg38,
1494 weight 12; miniprot-UniParc, weight 5; and LiftOff-mMyoMyo1, weight 5) with hints from protein orthology
1495 (miniprot-UniParc, weight 6) and RNA-seq (TRINITY, weight 5) for alternative splicing. By default,
1496 EvidenceModeler does not consider genes that are located within intronic regions of other genes. To
1497 restore these genes, we intersected the EvidenceModeler consensus gene GFF with the TOGA-hg38
1498 GFF to identify which genes were present in intronic regions and omitted from EvidenceModeler; these
1499 genes were then added back to the EvidenceModeler gene set.

1500 To eliminate remaining spurious predictions, we cross-referenced our gene annotations against
1501 the SwissProt[219] database using DIAMOND[220] (v. 2.1.4) with settings "*--ultra-sensitive --outfmt 6 qseqid*
1502 *bitscore sseqid pident length mismatch gapopen qlen qstart qend slen sstart send ppos evalue --max-*
1503 *target-seqs 1 --evalue 1e-10* ". We kept all genes that matched a protein on SwissProt with at least 80%
1504 identity, matched over 50% of the target sequence, and coded for at least 50 amino acids. Of the
1505 remaining genes, we kept them only if they contained both a start and stop codon with no internal stop
1506 codons.

1507 Finally, we further curated our annotations by putting the EVM and TOGA gene predictions in
1508 competition with each other when they both annotated the same locus, but with different overlapping or
1509 neighboring annotations. In such cases, one of the gene annotations is likely closer to the truth. To
1510 determine which, we compared EVM and TOGA gene models with their closest human gene BLAST hits.
1511 Only proteins with a BLAST match to a human Ensembl v99 annotation with the lowest E-values below
1512 0.001 were considered. These human homologs were used as a reference for curation as they are well-
1513 defined and characterized. We observed that occasionally, either the EVM or TOGA model predicted a

1514 transcript much longer than their human closest homolog. Closer inspection revealed that such cases
1515 represent artifactual mergers of neighboring genes during the annotation process, clearly visible from the
1516 fact that they map to two distinct human homologs in succession. Such cases were resolved by choosing
1517 the annotations (between EVM and TOGA) that were not affected by the artificial merger. We further
1518 observed a specific class of mergers between neighboring, segmentally duplicated genes, with the
1519 resulting annotations representing chimeric mixes of exons from the duplicates. In such cases we
1520 selected the annotations that clearly stayed within the boundaries of the separate duplicates, as identified
1521 by mapping to the closest human homolog. For the remaining annotations where both TOGA and EVM
1522 both mapped to a single human homolog throughout their entire length, we selected the most complete
1523 annotation that was closest in length to the human homolog.

1524 Orthologous Gene Alignments

1525 Phylogeny and selection analyses described in this manuscript rely on high-quality alignments of
1526 bat orthologous coding sequences. To first find and align orthologous *Myotis* genes to the greatest extent
1527 possible, we first complemented the gene annotations described above with likely missing annotations
1528 that could still be found through BLAT homology searches. Missing gene annotations are always
1529 expected in non-model species genomes and reflect a feature of annotation pipelines in general, not an
1530 artifactual issue. For example if the first coding exon of a gene falls into a small local assembly gap, the
1531 lack of a start codon may prevent the trigger of a CDS annotation, or may lead to the clearly incomplete
1532 CDS being subsequently filtered out. Similarly, erroneous indels representing sequencing errors may
1533 interrupt coding reading frames. Genes with missing annotations can still be detected in assemblies
1534 through classic BLAST or BLAT homology searches, and then aligned with their annotated orthologs
1535 from other species. To align orthologous *Myotis* genes from ten species (those sequenced here plus
1536 *Myotis myotis* and *M. yumanensis*), we first decided to use *Myotis velifer* as the *Myotis* species of
1537 reference, since the RNA-seq data we used was generated with *M. velifer* tissues.

1538 We first looked for missing homologs of *M. velifer* genes in the other *Myotis* genomes by blatting
1539 *M. velifer* CDS to the other *Myotis* assemblies (BLAT command line including non-default options -q=dnax
1540 -t=dnax -fine) to find matches outside of already annotated genomic segments. When multiple velifer
1541 CDS matched to the same locus with multiple overlapping homologous BLAT matches, we selected the
1542 match with the highest number of identical nucleotides. The remaining matching BLAT sequences were
1543 further considered if they spanned at least 50% of the velifer CDS, and included 100 codons or more.
1544 BLAT matches including stop codons were removed. This process added 1,837 putative CDS to consider
1545 for orthologous alignments for *M. auriculus*, 1,785 for *M. californicus*, 1,796 for *M. evotis*, 1,505 for *M.*
1546 *lucifugus*, 3,234 for *M. myotis*, 1,826 for *M. occultus*, 1,822 for *M. thysanodes*, 1,800 for *M. volans* and
1547 1,729 for *M. yumanensis*. The correct reading frames for these putative CDS were then determined by
1548 aligning to the velifer CDS that generated the initial match with MACSE v2. MACSE has the crucial
1549 advantage over other aligners of being able to repair broken reading frames due to sequencing indel
1550 errors or erroneous gene annotations. At this stage, we restricted any further analysis to those velifer
1551 CDS with human homologs (BLASTP E-value<0.001 with at least one human canonical protein-coding
1552 gene from Ensembl). One-to-one orthologs with the 23,030 remaining velifer CDS in other *Myotis* species
1553 were then determined using Orthofinder v2.5.4[221]. The sequences of each group of ortholog were then
1554 aligned with MACSE v2[222] with default settings. The resulting CDS with potentially repaired reading

1555 frames were then checked with PREQUAL[223] to exclude sequencing errors and erroneous inclusion of
1556 non-homologous segments in annotations. The remaining parts of orthologous sequences that passed
1557 PREQUAL filtering were then aligned again using MACSE v2 with default settings. The first round of
1558 alignment with MACSE ensures that we do not remove portions of CDS that look like they have no
1559 homology and would thus be removed by PREQUAL, just because of frameshifts that are easy to repair
1560 first with MACSE. The second round of MACSE is to align the remaining codons once PREQUAL has
1561 removed erroneous portions of CDS that could have otherwise disturbed the alignment process. We
1562 further masked (i.e. replaced with indels) codons near indels with putative alignment errors as described
1563 in Bowman et al.[224]. Of the 23,030 initial *M. velifer* CDSs, this process resulted in 21,756 alignments with
1564 at least one ortholog in another *Myotis* species.

1565 We also aligned pan-Chiroptera orthologs from 47 non-*Myotis* genomes publicly available on
1566 NCBI at the time of analysis, to test the generality of our observations to all bats. We used the same
1567 strategy described above to complement *Myotis* gene annotations with BLAT matches, but this time
1568 blatting velifer CDS on non-Myotis assemblies (with -q=dnax -t=dnax -fine again) to find all the potential
1569 orthologs in the non-Myotis assemblies. We previously found that because BLAT represents a first filter
1570 to include only portions of homologous CDS with good local similarity, using BLAT matches results in
1571 higher quality alignments of orthologs than using existing gene annotations of disparate qualities that too
1572 often include non-homologous portions of introns among other issues[224,225]. As before with only *Myotis*
1573 species, we recovered putative one-to-one orthologs with Orthofinder. This process resulted in the
1574 alignment (as previously described with two rounds of MACSE and PREQUAL in the middle) of 19,009
1575 orthologous CDS with at least one non-*Myotis* orthologous CDS.

1576 To test whether the patterns of virus-driven adaptation observed in bats are unique across
1577 mammals, we also prepared four more datasets of 70 primate orthologous CDS alignments, 138
1578 euungulate alignments, 127 glire alignments, and 82 carnivora alignments (see supplementary files XY
1579 for the species and their respective assemblies used). We used the same pipeline as the one used to
1580 align 47 pan-chiroptera species as described above, except that instead of starting from velifer CDS, we
1581 started from human Ensembl v109[226] CDS (the longest isoform available in each case) for primates, *Mus*
1582 *musculus* Ensembl v109 longest CDS for glires, *Canis familiaris* Ensembl v109 longest CDS for
1583 carnivores, and *Bos taurus* Ensembl v109 longest CDS for euungulates . These species were chosen for
1584 the very high quality of their gene annotations.

1585 Gene Trees & Phylogeny

1586 A phylogeny of all 536 mammals in our alignments was generated using IQTREE[227] (version
1587 2.3.1) using all gene alignments with the settings "-B 1000 -m GTR+F3x4+R6." To generate gene trees,
1588 we first filtered our gene alignments to exclude alignments with over 50% gaps in the sequence and less
1589 than 4 species. With the remaining alignments, we used IQTREE to find the best-fitting substitution model
1590 and tree using settings "--wbtl --bnni --alrt 1000 -B 1000 --safe". The best substitution models for each
1591 gene were saved as a NEXUS file. To generate the phylogeny of bats, we first concatenated all gene
1592 alignments using *catfasta2phyml* (https://github.com/nylander/catfasta2phyml) to concatenate our
1593 individual gene alignments into species-level alignments, filling in missing species in each sub-alignment

with gap symbols to preserve the alignment structure. Furthermore, we generated a partition file describing the region of each gene sub-alignment within the concatenated alignment.

Time-calibration of 59 bat genomes

Using our codon alignments of 59 bat genomes, we generated a time-calibrated phylogeny using mcmctree[228] and PAML[229] (v. 4.10.0) using an approximate likelihood method. Using the pan-bat codon alignments and our phylogeny as input, with fossil calibrations based on previously published work[4,36,230–237], we ran *mcmctree* twice to generate the Hessian matrix and confirm convergence. This was followed by 10 independent chains using the "out.BV" file from the first run. Finally, the output files of all 10 chains were combined to compute final divergence time estimates (see Table S2).

Ancestral Body Size, Lifespan, and Cancer Risk reconstruction

To explore how body size and lifespan have evolved over time in mammals, we used a super-phylogeny of mammal species[67] subsampled to only contain species with extant body size and lifespan data collected from AnAge[15] and PanTHERIA[16]. Ancestral body sizes and lifespans were simulated separately using StableTraits[238].

To estimate ancestral longevity quotients (AncLQs), we followed the method of Austad and Fisher[18] and used a linear model of lifespan given body size trained on non-flying mammals to predict the lifespans at each ancestral node given median estimates of body size. AncLQs were then estimated from the ratio of observed lifespan versus predicted lifespan for each node.

Relative Incidence of Cancer Risk (RICR) was calculated across our mammalian phylogeny following the method of Vazquez and Lynch (2021)[44]. The cancer risk *K* at a given node was calculated using the log of the median predicted body size and lifespan. An organism's lifetime risk of cancer *K* is proportional to Dt^6, where D is the body size and T is the maximum lifespan. RICR is then calculated as the $\log_2$ ratio of the cancer risk between a node and its direct ancestor.

Selection Scans & Evolutionary Rates

aBSREL

To conservatively test for branch-specific selection, we used aBSREL[95,239] (version 2.5.48) to test for selection at each branch within the Nearctic *Myotis* clade for 15,734 gene alignments spanning 536 mammals. These genes were identified as 1:1 orthologs across the full alignment, with no more than 50% sequence gaps and at least 4 species present in the alignment. We defined genes under selection as those with an FDR-corrected p-value of less than 0.05; genes were specifically identified as under positive selection if $\omega>1$.

BUSTED

To quantify the total amount of positive selection across the *Myotis* tree or the different species trees used in this manuscript, we used an improved version of the BUSTED[110,239] test called BUSTED-MH. The original BUSTED test estimates for a given gene the proportion of codons that have evolved under positive selection, with dN/dS>1, summed over all the branches of a given tree, regardless of the branch and regardless of the codons in a multi-species alignment. The version of BUSTED we used, BUSTED-MH, includes two crucial improvements over the original BUSTED that make it much less likely to generate false positive inferences of positive selection, albeit at the cost of becoming a very conservative test. First, BUSTED-MH takes synonymous substitution rate variation into account, which prevents mistaking cases where dN/dS is greater than one just because dS is low, with cases where dN/dS is greater than one because positive selection actually increased dN. Second, BUSTED-MH takes complex substitutions that simultaneously involve more than one nucleotide into account in its likelihood models. This prevents attributing positive selection to cases where dN/dS is greater than one where instead a complex substitution changed multiple amino acids in a single event. BUSTED-MH has been shown to strongly reduce the rate of false positives that typically plague dN/dS-based tests of positive selection[240].

We applied BUSTED-MH to 19,646 *Myotis* orthologous CDS alignments with at least five orthologs. These orthologs are cases where the Orthofinder gene trees coincide with the species tree. This effectively removes issues regarding whether we should use the gene or the species tree, at the cost of removing 2,110 genes from the *Myotis* selection analysis. Similarly, we applied BUSTED-MH to 17,469 non-*Myotis* bat alignments with at least five orthologs. This includes a subset of 14,091 alignments with orthologs in two thirds of the non-*Myotis* bat species that we specifically used to show that patterns of virus-driven adaptation are representative of all, and not just a limited subset of bats. We also tested 17,890 primate alignments with at least five orthologs with BUSTED-MH, as well as 19,311 glire, 18,000 carnivora and 18,504 ungulate alignments.

RERConverge

Between-species life history diversity may be undergirded by significant evolutionary rate shifts in important genes, where evolutionary change across the gene tree correlates either positively or negatively with changes in a particular life history trait across the trait tree. In *Myotis*, we were interested specifically in testing whether or not longevity-related metrics could be correlated with evolutionary rate shifts for particular genes, and if, among those, we could identify types of genes (gene ontologies) that were enriched.

To answer this question, we used RERconverge[106], an R package which uses gene trees to compute relative evolutionary rates (RERs), then tests for correlations between RERs and trait changes between species. 40 bat genomes were aligned to produce MSAs, which were then split into three groups to be tested independently: all bats (n=59), non-Myotis bats (n=29), and Myotis (n=11). Gene trees were constructed under the GTR+G model with the same topology as determined in our phylogenetic analysis, across all 39 available bat species. After concatenating the gene trees, RERs were calculated in RERconverge. Trait correlation analysis was performed by regressing these RERs against 4 distinct trait axes. Two of the axes were maximum longevity and size, which were obtained from AnAge[151] and PanTHERIA[16]; an additional two axes were obtained by plotting species along the first 2 principal

1666 components of size and maximum longevity. Since size generally correlates with longevity, even within
1667 Myotis, PCA allows us to describe species using orthogonal trait axes that roughly correspond to size-
1668 independent longevity and longevity-independent size. Using a Wilcoxon rank-sum test, we then tested
1669 for enrichment in correlation significance amongst different gene sets.

1670 RELAX

1671 The evolution of life history diversity across a clade may also manifest in differential selection
1672 regimes across relevant genes or types of genes. Specifically, the evolution of a particular life history
1673 may be driven by either relaxation or intensification of selection in different genes. In Myotis, we were
1674 again interested in whether we could identify genes and gene sets related to increased longevity within
1675 the clade.

1676 RELAX[99] is used to identify genes under either relaxation or intensification of selection across
1677 groups groups of species within a clade using MSAs and a labeled species tree. MSAs for 11 available
1678 Myotis species across ~19,000 shared genes were fit using the BS-REL framework to a branch-site
1679 model, using the species tree determined from our phylogenetic analysis. 4 longer-lived species, *Myotis*
1680 *lucifugus*, *M. occultus*, *M. evotis*, and *M. myotis* were set as the foreground class with the remaining
1681 species set as the background class. RELAX then used these branch classes to estimate a distribution
1682 of ω (dN/dS) for each branch class, constrained by the relaxation factor k. An LRT is performed for $k \neq 1$
1683 against $k = 1$, with $k > 1$ implying relaxation of selection and $k < 1$ implying intensification of selection.
1684 The results from this test were then used to perform a Wilcoxon rank-sum test to identify enrichment in
1685 the significance of the k-parameter amongst different gene sets.

1686 VIPs

1687 To determine if *Myotis* and other bats are enriched for adaptation at Virus Interacting Proteins
1688 (VIPs), we conducted a test comparing levels of adaptation, inferred by BUSTED, in sets of VIP genes
1689 compared to matched control genes. Sets of control genes were resampled in a bootstrap procedure
1690 (https://github.com/DavidPierreEnard/Gene_Set_Enrichment_Pipeline) to generate 95% confidence
1691 intervals for sets of genes at progressively smaller BUSTED p-value thresholds[109,111,113,152]. When VIPs
1692 are subject to greater levels of positive selection than expected relative to the sets of matched control
1693 genes, we expect a pattern in which the high p-value thresholds show weaker enrichment but smaller
1694 confidence intervals, because more genes are used in these calculations. As the p-value threshold gets
1695 smaller, the signal of enrichment is expected to get stronger but at the expense of larger confidence
1696 intervals.

1697 We generated five sets of VIP genes: A set of all VIP genes with aligned orthologs from at least
1698 five species in the tested clade (Nearctic *Myotis* or pan-Chiroptera without *Myotis*); a set of VIP genes
1699 with known pro- and/or anti-viral activity; a set of VIP genes with no known pro- and/or anti-viral activity;
1700 a set of VIP genes that interact only with DNA viruses; and a set of VIP genes that interact only with RNA
1701 viruses. Because both the number of species and genes included, as well as their level of homology,
1702 influences the power of these tests we also tested the influence of the stringency of gene choice by
1703 generating a separate set of genes for the pan-Chiroptera analyses that included only genes with aligned
1704 orthologs in at least two thirds of the non-*Myotis* species. Analyses using this more limited set of genes

1705 show the same result in terms of enrichment of adaptation in VIP genes and comparing DNA VIPs and
1706 RNA VIPs, showing that the observed patterns are valid across bats regardless of the stringency of
1707 homology.

1708 The bootstrap procedure matches a tested gene set of interest such as VIPs with sets of control
1709 genes (non-VIPs when testing VIPs) that have the same average values as the set of interest for multiple
1710 potential confounding factors that could explain differences in adaptation instead of interactions with
1711 viruses. For example, if the level of gene mRNA expression has an influence on the rate of adaptation,
1712 we then need to match VIPs with control sets of non-VIPs that collectively have the same average
1713 expression as VIPs. For each group of tested VIPs we build 1,000 control sets with randomly sampled
1714 non-VIPs according to a matching procedure described in Enard & Petrov 2020[152,241]. We match the 27
1715 following factors between VIPs and non-VIPs, for all tested groups of species:

1716 ● the length of the aligned CDS.
1717 ● the overall CDS GC content in each orthologous alignment.
1718 ● the GC content at aligned codons' position 1, 2 and 3 separately.
1719 ● the number of species with a onetoone ortholog out of all the species included in an alignment,
1720 where species with no ortholog are represented by gaps the whole length of the alignment.
1721 ● the number of species with an ortholog at least 90% of the length of the species of reference
1722 (Myotis velifer in bats, human in primates, etc; see above).
1723 ● the overall proportion of each orthologous alignment made of indels.
1724 ● the three synonymous rates of evolution estimated by the likelihood model of HYPHY Busted.
1725 ● the proportions of codons that fall in the three latter synonymous rates.
1726 ● average human mRNA expression in 53 GTEx v7 tissues[242], in $\log_2$ of Transcripts Per Million
1727 (TPM).
1728 ● lymphocyte human mRNA expression from GTEx v7, in $\log_2$ of TPM.
1729 ● testis human mRNA expression from GTEx v7, in $\log_2$ of TPM.
1730 ● mRNA expression in $\log_2$ of TPM for six separate *Myotis velifer* tissues: heart, brain, kidneys,
1731 lungs, pancreas, and testis.
1732 ● the number in $\log_2$ of protein-protein interactions (PPIs) in the human protein interaction
1733 network[243].
1734 ● the proportion of genes that are immune genes according to Gene Ontology annotations of
1735 the closest human homolog including Gene Ontology terms GO:0002376 (immune system
1736 process), GO:0006952 (defense response), and/or GO:0006955 (immune response) as of
1737 summer 2021[244].
1738 ● the proportion of housekeeping genes defined as genes with stable expression across many
1739 human tissues, listed in Eisenberg & Levanon[245].
1740 ● the overall dN/dS ratio estimated by Busted for the orthologous CDS alignments.

1741 We match the overall dN/dS between VIPs and control non-VIPs to account for an important
1742 issue of dN/dS tests: dN/dS-based tests tend to lose statistical power to detect positive selection
1743 in CDS alignments with higher selective constraint[246]. The amount of positively selected sites
1744 being equal, positive selection tests based on dN/dS tend to have lower statistical power and
1745 tend to generate more false negative results when the rest of the coding sequence is more highly
1746 constrained. VIPs tend to be much more strongly constrained than non-VIPs[109], which gives a

1747 strong, unfair statistical disadvantage to VIPs when testing positive selection with BUSTED or
1748 other HYPHY tests. We limit this issue by matching VIPs and control non-VIPs for dN/dS. Thus,
1749 VIPs have an excess of adaptation compared to non-VIPs when they have a balance of the same
1750 total amount of non-synonymous changes more tilted towards advantageous rather than neutral
1751 amino acid changes. In this case non-VIPs still have less constraint (more neutral changes) than
1752 VIPs, and thus still more power to detect positive selection, but not to an extent as severe and
1753 unfair as if we did not match the overall dN/dS[109]. In the case where VIPs do not have an excess
1754 of adaptation, then they have the same balance of advantageous and neutral amino acid changes
1755 resulting in the same overall dN/dS. This is the case of RNA VIPs in bats in this study; this internal
1756 negative control shows that the matching of dN/dS works as intended.

1757 Gene Duplications

1758 To quantify patterns of gene duplication and loss, we quantified the copy number of genes with
1759 human orthologs from our gene annotations for each nearctic *Myotis* genome. To calculate per-gene
1760 expansion and loss rates and their statistical significance, we ran CAFE[137] v5 on the previously described
1761 set of copy number counts using our time-calibrated species tree pruned to include only the nine nearctic
1762 *Myotis* species. *M. myotis* was excluded because of its lower quality assembly. We ran CAFE on the
1763 subset of genes with two or more copies in at least one species using a Poisson distribution for the root
1764 frequency (*-p*), first generating an error model to correct for genome assembly and annotation error (*-e*).
1765 We compared the base model (each gene family belongs to the same evolutionary rate category) to
1766 gamma models (each gene family can belong to one of *k* evolutionary rate categories) with different
1767 values of *k*. A final gamma model with *k*=9 was chosen to balance model log likelihood with the number
1768 of gene families for which the optimizer failed. The model was run three separate times to ensure
1769 convergence.

1770 To understand if genes in these pathways have higher birth rates or are more likely to have
1771 significant changes in gene copy number than expected relative to other genes, we compared the gene
1772 copy birth rate λ and number of genes that have significantly expanded or contracted in copy number on
1773 at least one branch within our nearctic *Myotis* phylogeny. Following Huang et al.[48], we tested if VIP genes
1774 in particular underwent significant copy number changes or had significantly different birth/death rates
1775 than non-VIP genes. For each category of VIP genes (all VIPs, DNA VIPs, DNA only VIPs, RNA VIPs,
1776 and RNA only VIPs), we generated 100 bootstrap sets of control non-VIP genes with the same number
1777 of genes as the corresponding VIP gene set. We ran CAFE on each set of VIP genes and the
1778 corresponding control non-VIP genes to infer per-gene birth-death rates and per-gene, per-branch
1779 expansion/loss events.

1780 Assessment of DNA Double-Strand Break Tolerance

1781 We assessed each species' tolerance to DNA double strand breaks using a by measuring viability,
1782 cytotoxicty, and apoptosis across a range of doses of Neocarzinostatin, a radiomimetic drug. We
1783 measured dose response curves in wing-derived primary dermal fibroblasts across 5 bat species (*Myotis*
1784 *lucifugus*, n=8; *Myotis evotis*, n=3; *Rousettus langosus*, n=2; *Eidolon helvum*, n=2; *Pteropus rodrigensis*,
1785 n=2) using the multiplexed ApoTox-Glo assay (Promega). Using 96-well plates, two individuals and 11

1786 doses were assessed simultaneously with four technical replicates. Results were normalized to treatment
1787 controls for each individual in R as previously described[42,43,46,50].

1788 Mapping PKR exons

1789 We further validated the annotations for the PKR locus by re-aligning the primary *M. velifer* coding
1790 sequence back to the nine nearctic *Myotis* reference genomes, as well as a non-*Myotis* outgroup,
1791 *Pipistrellus pygmaeus*, and the genome haplotypes for each of these species. Because the presence of
1792 two copies makes this task challenging for most aligners, we independently aligned the *M. velifer*
1793 reference PKR sequence to sequential sections of each genome in 50kb search regions surrounding the
1794 known loci in each genome. This alignment search was conducted for 5 regions upstream (250 kb) and
1795 5 regions downstream (250 kb) of the known loci. In species with two known copies, the location of each
1796 copy was included in a separate search region. This was to prevent erroneous merging or loss of exons.
1797 These regions were retrieved using bedtools getfasta[247] and alignment was performed using miniprot[62].
1798 Miniprot settings were optimized to retain secondary alignments (-p 0 -n 1 –outsc=0.0 –outc=0.0) and
1799 find known exons with accurate boundaries (-J 18 -F 21 -O 15 -L 10). The resulting gff file was converted
1800 to bed format using AGAT[248], sequences retrieved with bedtools getfasta, and a custom script used to
1801 remove identical duplicates. Finally, all sequences were aligned with MACSE v2.07[222]. We used
1802 BISER[125,208] to confirm the presence of segmental duplications in these regions.

1803 PKR cell lines and vectors

1804 All PKR experiments were performed using HeLa PKR-KO cells (kindly provided by A. Geballe,
1805 Fred Hutchinson Cancer Center, Seattle WA) that were plated either at densities of 5x10^4 cells/mL in
1806 24-well plates or at 1x10^5 cells/mL in 12-well plates. The cells were maintained at 37°C with 5% CO_2
1807 and cultured in DMEM supplemented with 5% fetal bovine serum (FBS), 1% penicillin/ streptomycin mix
1808 and 1 µg/mL puromycin (Sigma-Aldrich). All transfections were performed 24 hours after seeding, using
1809 3 µL of TransIT-LT1 Transfection Reagent (Mirus Bio) per 1 µg of DNA and Opti-MEM media. We used
1810 previously-generated pSG5-FLAGx2 vectors encoding either *M. myotis* PKR-1 (GenBank OP006550),
1811 *M. myotis* PKR-2 (GenBank OP006559), *M. velifer* PKR-1 (GenBank OP006558), or *M. velifer* PKR-2
1812 (GenBank OP006557)[28]. Plasmids encoding the interferon-stimulated gene ISG20[241] and a constitutively
1813 active variant of the sterile alpha motif domain-containing protein 9-like SAMD9L-F886Lfs*11 (here,
1814 SAMD9L[249]) were used as controls in viral infections and cell translation experiments, respectively.

1815 Western blot

1816 We assessed for the steady state protein expression of *M. myotis* Flag-PKRs after transfection
1817 of 350 ng and 700 ng of DNA plasmids encoding either PKR1 alone, PKR2 alone, or both PKR1 and
1818 PKR2 (175 ng of each and 350 ng of each, respectively). Briefly, cells were re-suspended and lysed in
1819 ice-cold RIPA buffer (50 mM Tris pH8, 150 mM NaCl, 2 mM EDTA, 0.5% NP40) with protease inhibitor
1820 cocktail (Roche) and sonicated. 20 µL of the clarified fraction was denatured with 5 µL of 6x Laemmli
1821 buffer at 95°C for 5 min and loaded into 4-20% BioRad Criterion TGX Stain-Free precast gel. The wet
1822 transfer into a PVDF membrane was executed overnight at 4°C. The membranes were blocked in a
1823 1xTBS-T buffer (Tris HCl 50 mM pH8, NaCl 30 mM, 0.05% of Tween 20) containing 10 % powder milk,

1824 and were incubated for 1h. The membranes were incubated with primary mouse anti-Flag (Sigma F3165)
1825 and anti-Tubulin (Sigma T5168) antibodies and secondary anti-Mouse IgG-Peroxidase conjugated
1826 (Sigma A9044). Detection was made using the Chemidoc Imagina System (BioRad) with SuperSignal
1827 West Pico Chemiluminescent Substrate (ThermoFisher Scientific).

1828 PKR co-immunoprecipitation

1829 Hela ΔPKR cells were transfected with 1.25µg plenti6 HA-tagged *M. myotis* PKR1 plasmid per million
1830 cells and 1.25µg of either plenti6 myc empty vector, myc-tagged *M. myotis* PKR1 or myc-tagged *M.*
1831 *myotis* PKR2 plasmid using TransIT-LTI transfection reagent (Mirus Bio). The next day, some wells were
1832 infected with Sindbis virus expressing GFP (SINV-GFP) at MOI 2 for 24 hours. Cells were then scraped
1833 with cold PBS and pelleted. For the IP, cells were lysed in 500µl IP buffer (50mM Tris HCl pH7.5, 140mM
1834 NaCl, 6 mM MgCl2, 0.1% NP40) supplemented with RNase (RiboLock, Fisher Scientific) and protease
1835 (cOmplete EDTA-free protease inhibitor cocktail, Sigma) inhibitors for 10 minutes on ice, then centrifuged
1836 at 12,000 *xg* for 10 min at 4°C. 5% of the volume was kept for input, while the rest was incubated with
1837 40µl µMACS anti-c-myc MicroBeads (Miltenyi Biotec) for 1h at 4°C with constant rotation. Samples were
1838 then loaded onto µMACS columns placed in the magnetic field of a µMACS Separator (Miltenyi Biotec),
1839 washed 4 times with cold IP buffer, and eluted with the µMACS denaturing elution buffer. Proteins were
1840 denatured in elution buffer for 5 min at 95°C, then loaded onto a 4-20% BioRad Criterion TGX Stain-Free
1841 precast gel and transferred onto an Amersham Protran nitrocellulose membrane (Sigma) for 1h.
1842 Membranes were blocked for 1h in 5% milk in PBS (Euromedex) supplemented with 0.2% tween (Fisher)
1843 and incubated with mouse anti-myc monoclonal antibodies (Abcam 9E10, cat# ab32) then secondary
1844 anti-mouse IgG antibodies conjugated with HRP (Sigma, cat# A4416), or with rat anti-HA antibodies
1845 conjugated with HRP (Roche, Sigma, cat# 12013819001). Images were taken on a Fusion FX imager
1846 (Vilber) with SuperSignal West Femto Chemiluminescent Substrate (ThermoFisher Scientific).

1847 Cell viability assay

1848 Hela PKR-KO cells were transfected 24h after plating in 96 well plates, with 100 or 200 ng of
1849 pSG5 plasmid: empty or coding for *M. myotis* or *M. velifer* PKR1, PKR2 or PKR1+2 equal mix (50%-
1850 50%). 24 hours post-transfection, positive control cells were treated with an apoptosis-inducing drug,
1851 Etoposide, at different doses (250, 200 or 100 µM). 48 hours post transfection, cells were harvested and
1852 lysed to quantify luminescent signal according to CellTiter-Glo® Luminescent Cell Viability Assay
1853 (Promega) kit protocol.

1854 VSV and SINV infections

1855 VSV infections. Cells were transfected 24 h after plating with 350 ng of pSG5 plasmid: empty, or
1856 encoding *M. myotis* or *M. velifer* PKR1, PKR2, or equal input of PKR1 and PKR2 (175 ng per plasmid),
1857 or a plasmid encoding interferon-stimulated exonuclease gene 20 (ISG20), due to its known antiviral
1858 activity against VSV as positive control[241]. Cells were infected 24 h post transfection with replicative VSV-
1859 GFP virus[142] at a MOI of 3. Cells were fixed with 4% paraformaldehyde 16-18 hours post infection. VSV
1860 infection was quantified by measuring the percentage of GFP positive cell populations with BD

1861 FACSCanto II Flow Cytometer (SFR BioSciences). Fold change results were normalized to the empty
1862 pSG5 condition across at least three independent experiments.

1863 SINV infections. Hela ΔPKR cells were transfected with 5µg pSG5 empty vector, *M. myotis* PKR1,
1864 *M. myotis* PKR2 or 2.5µg *M. myotis* PKR1 + 2.5µg *M. myotis* PKR2 per million cells using TransIT-LTI
1865 transfection reagent (Mirus Bio). The next day, some wells were infected with SINV-GFP at MOI 0.2.
1866 Cells were then placed into a CellCyte X live cell imaging system (Cytena) and pictures of every well
1867 were taken every 2h for 48h. The fraction of GFP+ cells over the total cell area was measured and
1868 averaged from six photos of 2 individual wells per condition, and repeated for a total of three independent
1869 experiments.

1870 Luciferase reporter assays

1871 Luciferase reporter assays were carried out to investigate whether the two PKR paralogs have
1872 synergistic, additive or dominant negative effect in translation shutdown. Transfection was performed as
1873 previously described with additional 50 ng of FFLuc firefly luciferase reporter plasmid per well. Sterile
1874 alpha motif domain-containing proteins 9L (SAMD9L gain-of-function mutant) was used as a positive
1875 control of translational repression[249]. 24 h post transfection, cells were briefly washed with PBS, lysed by
1876 a 5× reporter lysis buffer (Promega) and incubated overnight at -20°C. Cells were then collected and 100
1877 µl of the luciferase substrate (Promega) was added to 20 µl of the lysis supernatant. Alternatively, cells
1878 were lysed using BrightGlow Lysis Reagent (Promega E2620). The relative luminescence units (RLUs)
1879 were immediately quantified with LUMIstar Omega microplate reader optima (BMG Labtech). All
1880 luciferase assays were conducted in technical duplicates in at least five independent experiments. Fold
1881 change results were normalized to the empty pSG5 condition within each independent experiment.

1882 # Figures

1883 **Figure 1: 8 near-complete reference assemblies for North American (Nearctic) *Myotis*.**
1884 **Figure 2: Evolution of body size, lifespan, and cancer risk in bats and mammals.**
1885 **Figure 3: Selection in Nearctic *Myotis* is enriched for pleiotropic cancer resistance pathways.**
1886 **Figure 4: Adaptation to DNA viruses, but not RNA viruses, is enriched in *Myotis* and other bats.**
1887 **Figure 5: A varied structural variation landscape across 9 nearctic *Myotis* species.**
1888 **Figure 6: Evolutionary history and function of an actively segregating copy number polymorphism**
1889 **of *PKR* in *Myotis*.**

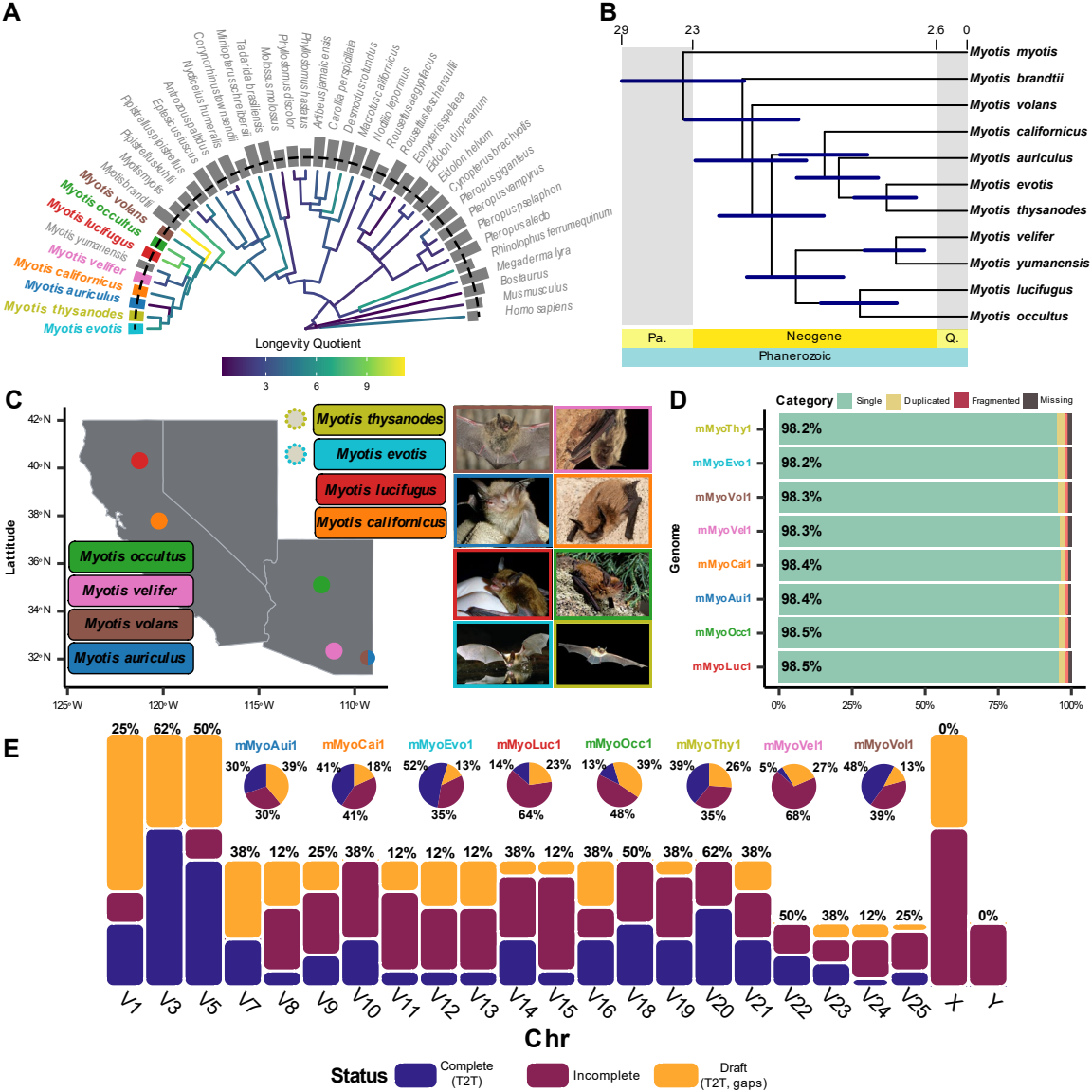
A
Longevity Quotient
3
6
9
Myotis volans
Myotis occultus
Myotis lucifugus
Myotis yumanensis
Myotis velifer
Myotis californicus
Myotis auriculus
Myotis thysanodes
Myotis evotis
Myotis brandtii
Myotis myotis
Pipistrellus pipistrellus
Pipistrellus kuhlii
Pipistrellus pipistrellus
Eptesicus fuscus
Antrozous pallidus
Nycticeius humeralis
Corynorhinus townsendii
Miniopterus schreibersii
Tadarida brasiliensis
Molossus molossus
Phyllostomus discolor
Phyllostomus hastatus
Artibeus jamaicensis
Carollia perspicillata
Desmodus rotundus
Macrotus californicus
Noctilio leporinus
Rousettus aegyptiacus
Rousettus leschenaulti
Eonycteris spelaea
Eidolon dupreanum
Eidolon helvum
Cynopterus brachyotis
Pteropus giganteus
Pteropus vampyrus
Pteropus pselaphon
Pteropus aledo
Rhinolophus ferrumequinum
Megaderma lyra
Bostaurus
Musmusculus
Homo sapiens
B
29
23
2.6
0
Myotis myotis
Myotis brandtii
Myotis volans
Myotis californicus
Myotis auriculus
Myotis evotis
Myotis thysanodes
Myotis velifer
Myotis yumanensis
Myotis lucifugus
Myotis occultus
Pa.
Neogene
Q.
Phanerozoic
C
Myotis thysanodes
Myotis evotis
Myotis lucifugus
Myotis californicus
Myotis occultus
Myotis velifer
Myotis volans
Myotis auriculus
Lattitude
42°N
40°N
38°N
36°N
34°N
32°N
125°W
120°W
115°W
110°W
D
Category
Single
Duplicated
Fragmented
Missing
Genome
mMyoThy1 98.2%
mMyoEvo1 98.2%
mMyoVol1 98.3%
mMyoVel1 98.3%
mMyoCai1 98.4%
mMyoAui1 98.4%
mMyoOcc1 98.5%
mMyoLuc1 98.5%
0%
25%
50%
75%
100%
E
mMyoAui1 30% 39% 30%
mMyoCai1 41% 18% 41%
mMyoEvo1 52% 13% 35%
mMyoLuc1 14% 23% 64%
mMyoOcc1 13% 39% 48%
mMyoThy1 39% 26% 35%
mMyoVel1 5% 27% 68%
mMyoVol1 48% 13% 39%
25% 62% 50% 38% 12% 25% 38% 12% 12% 12% 38% 12% 38% 50% 38% 62% 38% 50% 38% 12% 25% 0% 0%
V1 V3 V5 V7 V8 V9 V10 V11 V12 V13 V14 V15 V16 V18 V19 V20 V21 V22 V23 V24 V25 X Y
Chr
Status
Complete (T2T)
Incomplete
Draft (T2T, gaps)

1890 **Figure 1: 8 near-complete reference assemblies for North American (Nearctic) *Myotis*. A)** Phylogeny
1891 of 38 bat genomes with 3 outgroup species: cow *(bosTau9*), mouse (*mm39*); and human (*T2T-CHM13v2.0*).
1892 Bars at the tips of the phylogeny indicate the AuNG score of each genome (lower values equal more
1893 contiguous genomes); the dotted line represents the AuNG score for complete (T2T) genome assemblies
1894 as represented by T2T-CHM13v2.0. **B)** The time-calibrated phylogeny of 9 Nearctic and two representative
1895 Palaearctic *Myotis* species based on orthologous codon alignments. Blue bars represent age uncertainties.
1896 **C)** Map of capture sites with representative images (see "Acknowledgements" for attributions) for the
1897 individuals and species sequenced in this study; cell lines for *M. evotis* and *M. thysanodes* were provided
1898 by Richard Miller and were not collected for this study. **D)** Mammalian BUSCO scores for annotations
1899 generated for the 8 new *Myotis* genomes. **E)** Ideogram bar plot indicating completion status of each
1900 chromosome in assembly. Pie graphs indicate completion status of all chromosomes in assembly. All
1901 chromosomes were positively identified based on size, synteny, and homology to human chromosomes[57].
1902 "Complete (T2T)" status indicates that a chromosome is fully assembled telomere-to-telomere without gaps;
1903 "Draft (T2T, gaps)" status indicates that a chromosome is fully scaffolded with both telomeres, but has one
1904 or more gaps in the assembly; "Incomplete" status indicates that a chromosome was positively identified,
1905 but was not scaffolded from telomere to telomere (only contains one telomere).

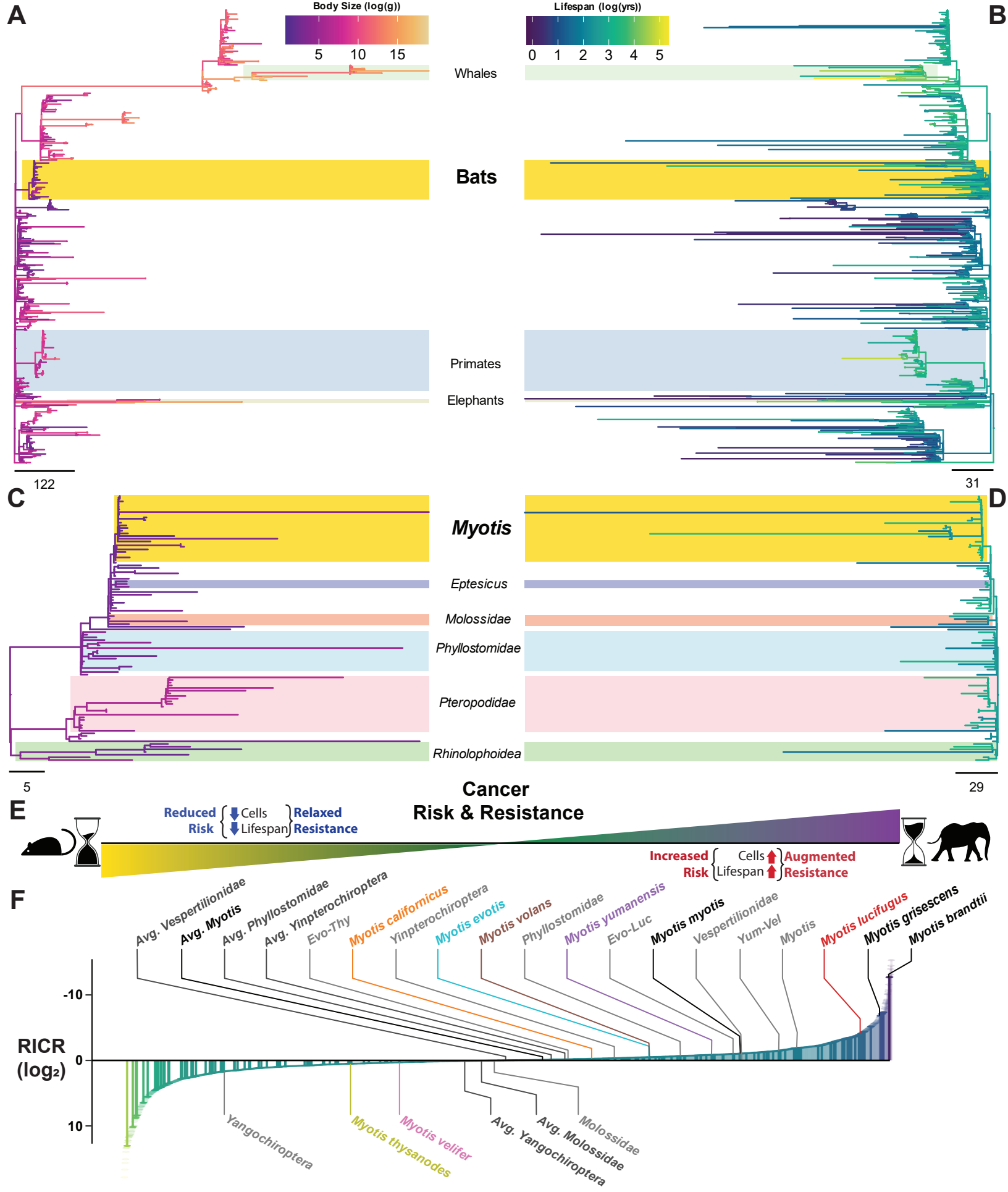
A
Body Size (log(g))
5
10
15
B
Lifespan (log(yrs))
0
1
2
3
4
5
Whales
Bats
Primates
Elephants
122
31
C
D
Myotis
Eptesicus
Molossidae
Phyllostomidae
Pteropodidae
Rhinolophoidea
5
29
Cancer
Risk & Resistance
E
Reduced Risk
Cells
Lifespan
Relaxed Resistance
Increased Risk
Cells
Lifespan
Augmented Resistance
F
Avg. Vespertilionidae
Avg. Myotis
Avg. Phyllostomidae
Avg. Yinpterochiroptera
Evo-Thy
Myotis californicus
Yinpterochiroptera
Myotis evotis
Myotis volans
Phyllostomidae
Myotis yumanensis
Evo-Luc
Myotis myotis
Vespertilionidae
Yum-Vel
Myotis
Myotis lucifugus
Myotis grisescens
Myotis brandtii
-10
RICR
(log2)
0
10
Yangochiroptera
Myotis thysanodes
Myotis velifer
Avg. Yangochiroptera
Avg. Molossidae
Molossidae

Supplemental Information

Document S1. Figures S1-S6
Table S1. Genome Statistics
Table S2. Phylogeny time calibration and evolutionary modeling data
Table S3. aBSREL significant gene lists and Reactome enrichments
Table S4. RERConverge and RELAX results and enrichments
Table S5. List of VIPs and VIP subclasses
Table S6. SyRI-identified structural variants (SVs)
Table S7. Experimental data for Neocarzinostatin and PKR experiments

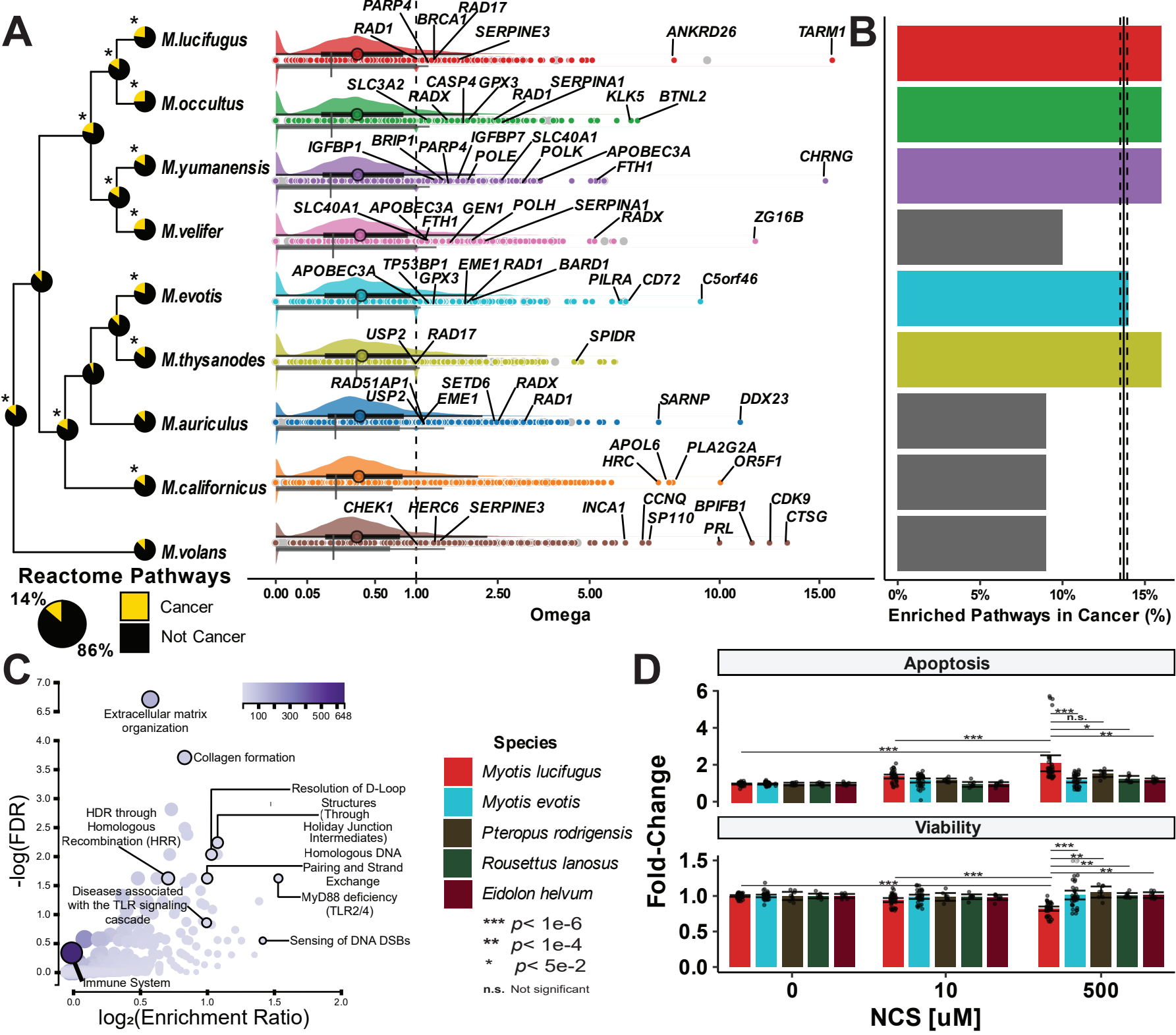
A
M.lucifugus
M.occultus
M.yumanensis
M.velifer
M.evotis
M.thysanodes
M.auriculus
M.californicus
M.volans
PARP4
BRCA1
RAD17
RAD1
SERPINE3
ANKRD26
TARM1
SLC3A2
CASP4
GPX3
SERPINA1
RADX
RAD1
KLK5
BTNL2
IGFBP1
BRIP1
PARP4
IGFBP7
SLC40A1
POLE
POLK
APOBEC3A
FTH1
CHRNG
SLC40A1
APOBEC3A
GEN1
POLH
SERPINA1
FTH1
RADX
ZG16B
APOBEC3A
TP53BP1
EME1
RAD1
BARD1
GPX3
PILRA
CD72
C5orf46
USP2
RAD17
SPIDR
RAD51AP1
SETD6
RADX
USP2
EME1
RAD1
SARNP
DDX23
APOL6
PLA2G2A
HRC
OR5F1
CHEK1
HERC6
SERPINE3
INCA1
CCNQ
SP110
BPIFB1
PRL
CDK9
CTSG
0.00 0.05 0.50 1.00 2.50 5.00 10.00 15.00
Omega
Reactome Pathways
14%
86%
Cancer
Not Cancer
B
0% 5% 10% 15%
Enriched Pathways in Cancer (%)
C
Extracellular matrix organization
Collagen formation
Resolution of D-Loop Structures (Through Holiday Junction Intermediates)
HDR through Homologous Recombination (HRR)
Homologous DNA Pairing and Strand Exchange
Diseases associated with the TLR signaling cascade
MyD88 deficiency (TLR2/4)
Sensing of DNA DSBs
Immune System
-log(FDR)
log2(Enrichment Ratio)
100 300 500 648
Species
Myotis lucifugus
Myotis evotis
Pteropus rodrigensis
Rousettus lanosus
Eidolon helvum
*** p< 1e-6
** p< 1e-4
* p< 5e-2
n.s. Not significant
D
Apoptosis
Viability
Fold-Change
0 10 500
NCS [uM]

1906 **Figure 2: Evolution of body size, lifespan, and cancer risk in bats and mammals. A, B)** Cophylo plot
1907 of the evolution of body size (**A**) and lifespan (**B**) across *Eutheria*. **C, D)** Cophylo plot of the evolution of
1908 body size (**C**) and lifespan (**D**) in bats. Branch lengths in **A-D** are scaled proportional to the rate of change
1909 of the trait over time, and tree scales are shown below their respective phylogenies. **E)** Diagram illustrating
1910 the relationship between changes in body size and lifespan with changes in cancer risk and resistance. **F)**
1911 Reduced Intrinsic Cancer Risk (RICR) for every node in *Eutheria*, ranked from greatest reduction in cancer
1912 risk to greatest increase in cancer risk. RICR relative to the most recent ancestor of select nodes are
1913 highlighted, as well as the average RICR across for all nodes within select clades.

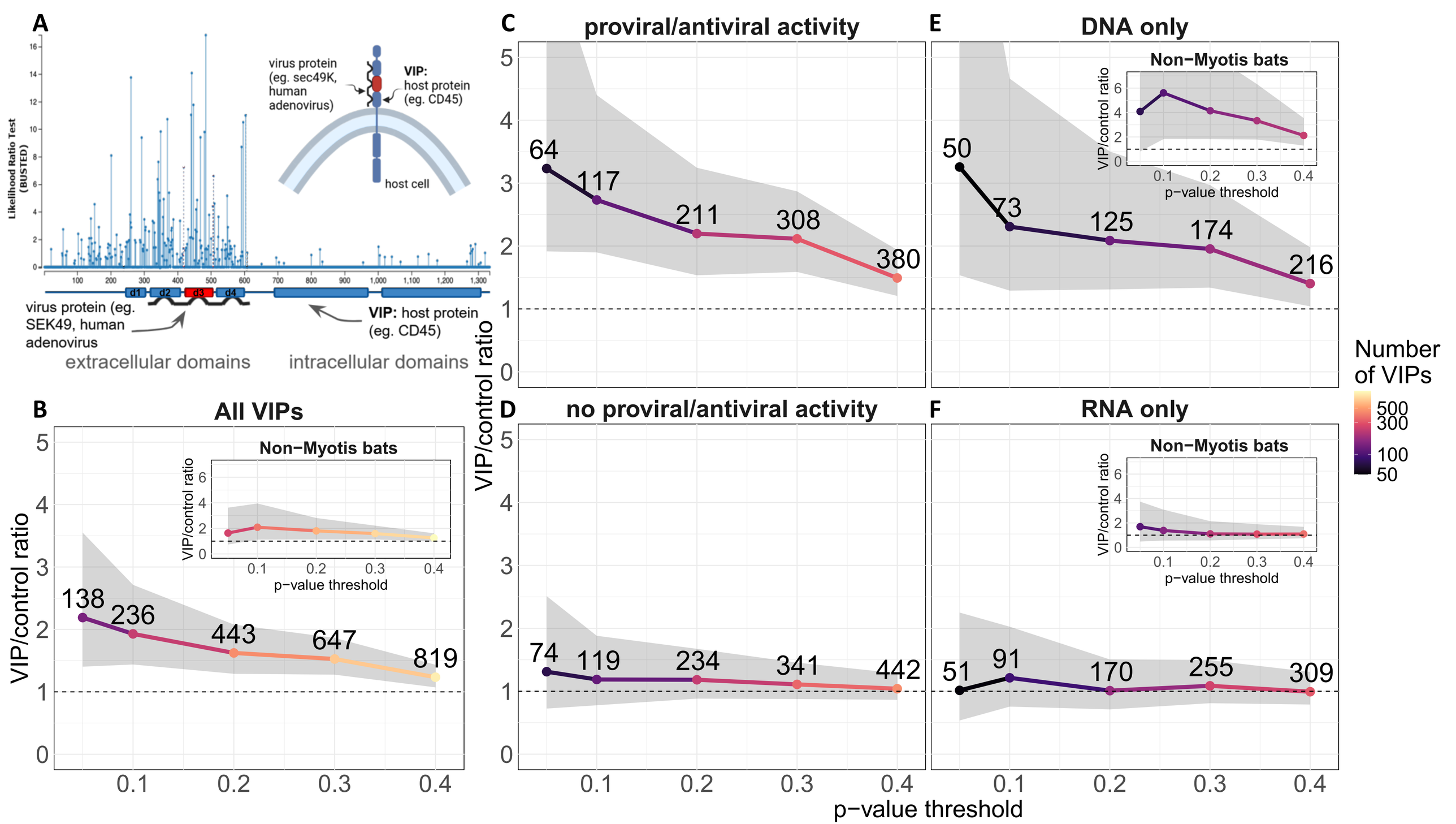
A
Likelihood Ratio Test (BUSTED)
virus protein (eg. sec49K, human adenovirus)
VIP: host protein (eg. CD45)
host cell
d1
d2
d3
d4
virus protein (eg. SEK49, human adenovirus
VIP: host protein (eg. CD45)
extracellular domains
intracellular domains
B
All VIPs
Non−Myotis bats
VIP/control ratio
p−value threshold
138
236
443
647
819
C
proviral/antiviral activity
64
117
211
308
380
D
no proviral/antiviral activity
74
119
234
341
442
E
DNA only
50
73
125
174
216
F
RNA only
51
91
170
255
309
Number of VIPs
500
300
100
50

1914 **Figure 3: Selection in Nearctic *Myotis* is enriched for pleiotropic cancer resistance pathways. A)**
1915 **Left**: phylogeny of Nearctic *Myotis*; **Right**: raincloud plot of omega values for all genes in each species
1916 since its most recent ancestor. The distribution of omega (**ω**) values for significant ($p \leq 0.05$ after multiple
1917 testing correction) genes and all genes is shown in color above the line. The 95% confidence interval and
1918 median for significant **ω**'s are represented by the black bar and circle, respectively; the overall 95%
1919 confidence interval and median are shown in grey below. Individual genes' **ω**'s are represented by colored
1920 points. Individual genes' omega values and grey, respectively. **Left inset**: Proportion of cancer-associated
1921 Reactome pathways among the top 100 pathways overrepresented among genes under selection at each
1922 node. Below, pie chart indicates expected proportion of pathways out of 100 that are cancer-associated
1923 after 1000 random samples. Nodes with proportions greater than the expected value with $p \leq 0.05$ using
1924 Fisher's exact test are indicated with an asterisk. **B)** Proportion of cancer-associated Reactome pathways
1925 among the top 100 pathways overrepresented among genes under selection across all nodes in a species'
1926 evolutionary history. **C)** Volcano plot of overrepresented pathways in Reactome among the union set of
1927 genes under selection across all nodes in the evolutionary history for *M. lucifugus*. **D)** Viability and
1928 Apoptosis fold-change in 5 bat species in response to different doses of neocarzinostatin, a potent inducer
1929 of DNA double-strand breaks. Points represent individual replicates normalized to each species' control,
1930 while bars represent mean ± 95% confidence intervals.

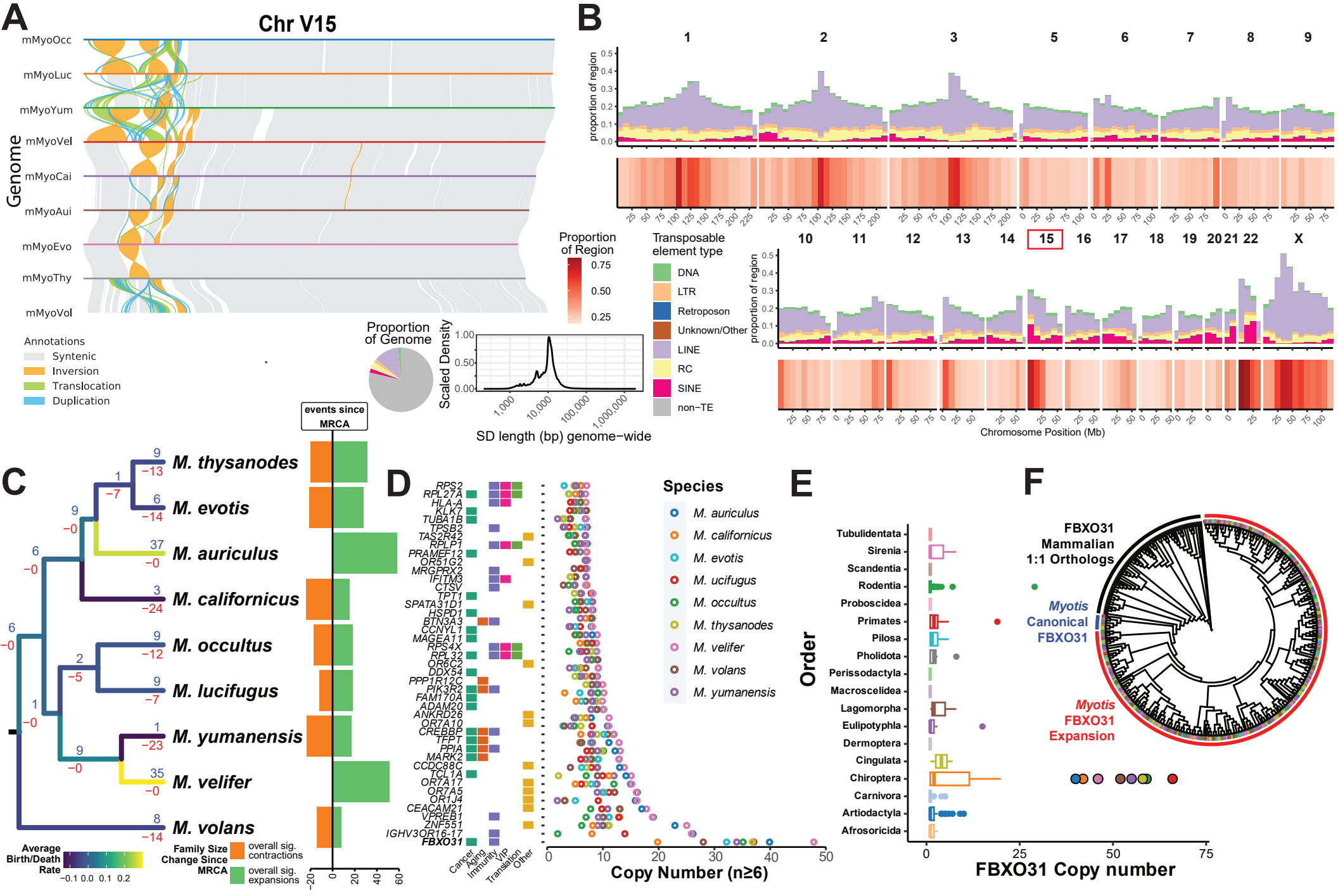
A
Chr V15
Genome
mMyoOcc
mMyoLuc
mMyoYum
mMyoVel
mMyoCai
mMyoAui
mMyoEvo
mMyoThy
mMyoVol
Annotations
Syntenic
Inversion
Translocation
Duplication
B
proportion of region
Proportion of Region
0.75
0.50
0.25
Transposable element type
DNA
LTR
Retroposon
Unknown/Other
LINE
RC
SINE
non−TE
Proportion of Genome
Scaled Density
SD length (bp) genome−wide
Chromosome Position (Mb)
C
events since MRCA
M. thysanodes
M. evotis
M. auriculus
M. californicus
M. occultus
M. lucifugus
M. yumanensis
M. velifer
M. volans
Average Birth/Death Rate
Family Size Change Since MRCA
overall sig. contractions
overall sig. expansions
D
Species
M. auriculus
M. californicus
M. evotis
M. ucifugus
M. occultus
M. thysanodes
M. velifer
M. volans
M. yumanensis
Cancer
Aging
Immunity
VIP
Translation
Other
Copy Number (n≥6)
E
Order
Tubulidentata
Sirenia
Scandentia
Rodentia
Proboscidea
Primates
Pilosa
Pholidota
Perissodactyla
Macroscelidea
Lagomorpha
Eulipotyphla
Dermoptera
Cingulata
Chiroptera
Carnivora
Artiodactyla
Afrosoricida
FBXO31 Copy number
F
FBXO31 Mammalian 1:1 Orthologs
Myotis Canonical FBXO31
Myotis FBXO31 Expansion

1931 **Figure 4: Adaptation to DNA viruses, but not RNA viruses, is enriched in *Myotis* and other bats. A)**
1932 Diagram of an example VIP, CD45: a host cell transmembrane receptor that interacts with the human
1933 adenovirus protein sec49K. Previous work has shown that the amino acids of CD45 that participate in this
1934 direct interaction are under strong positive selection, as indicated in the graph above the cartoon. **B-F)**
1935 Enrichment plots showing the ratio of positive selection in VIPs versus matched sets of control genes at
1936 different p-value thresholds. The solid line shows the median ratio; the color of the line, and the number
1937 above each point, represents the number of VIPs with significant BUSTED-MH p-values at the given
1938 threshold; the grey band represents the 95% confidence interval generated by bootstrapping sets of
1939 matched control genes. Inset plots show the same for all bats in this study excluding *Myotis*.

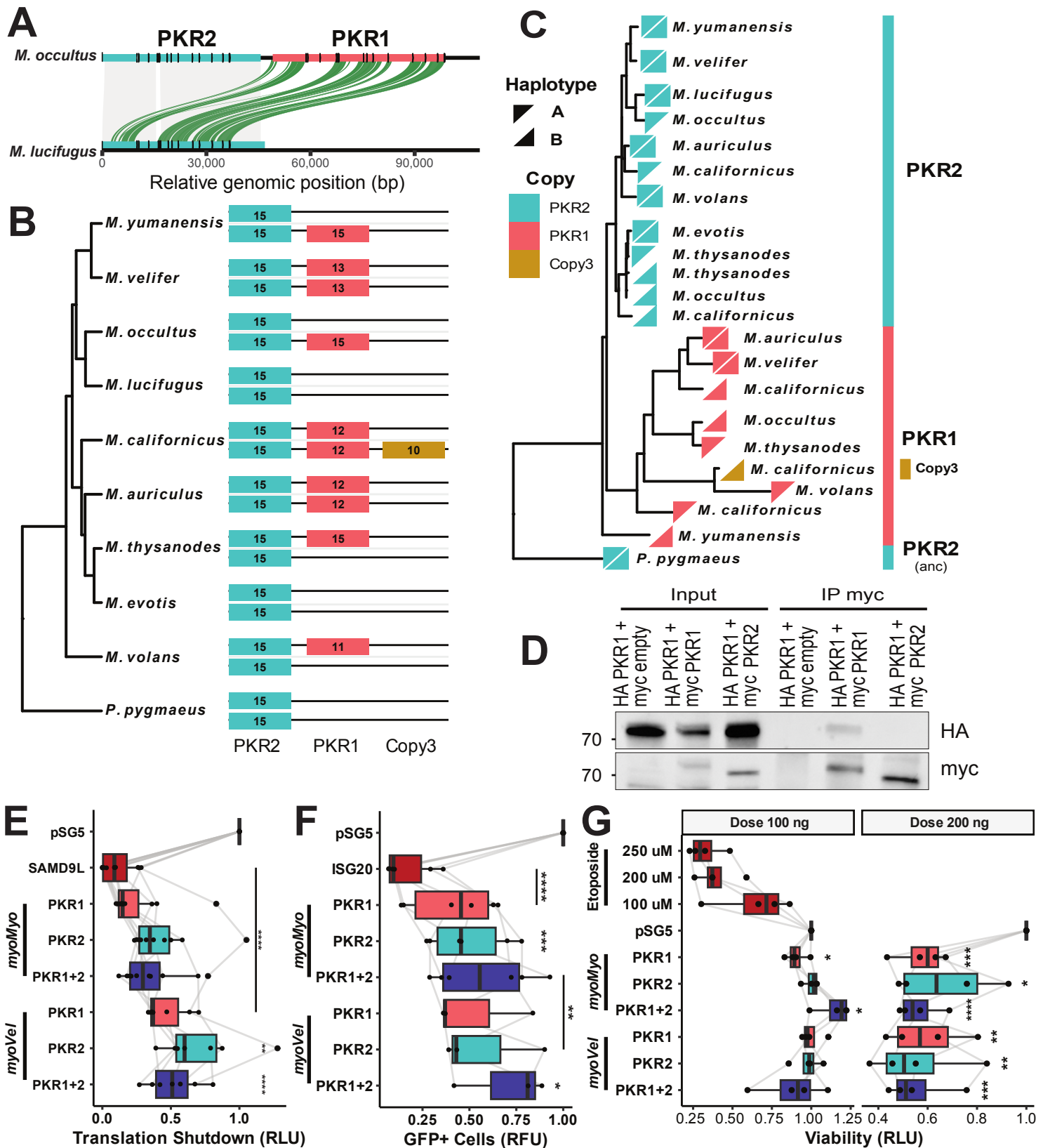
A
PKR2
PKR1
M. occultus
M. lucifugus
0
30,000
60,000
90,000
Relative genomic position (bp)
B
M. yumanensis
M. velifer
M. occultus
M. lucifugus
M. californicus
M. auriculus
M. thysanodes
M. evotis
M. volans
P. pygmaeus
PKR2
PKR1
Copy3
C
Haplotype
A
B
Copy
PKR2
PKR1
Copy3
M. yumanensis
M. velifer
M. lucifugus
M. occultus
M. auriculus
M. californicus
M. volans
M. evotis
M. thysanodes
M. thysanodes
M. occultus
M. californicus
M. auriculus
M. velifer
M. californicus
M. occultus
M. thysanodes
M. californicus
M. volans
M. californicus
M. yumanensis
P. pygmaeus
PKR2
PKR1
Copy3
PKR2
(anc)
D
Input
IP myc
HA PKR1 + myc empty
HA PKR1 + myc PKR1
HA PKR1 + myc PKR2
HA PKR1 + myc empty
HA PKR1 + myc PKR1
HA PKR1 + myc PKR2
70
70
HA
myc
E
pSG5
SAMD9L
PKR1
PKR2
PKR1+2
PKR1
PKR2
PKR1+2
myoMyo
myoVel
Translation Shutdown (RLU)
F
pSG5
ISG20
PKR1
PKR2
PKR1+2
PKR1
PKR2
PKR1+2
myoMyo
myoVel
GFP+ Cells (RFU)
G
Dose 100 ng
Dose 200 ng
Etoposide
250 uM
200 uM
100 uM
pSG5
PKR1
PKR2
PKR1+2
PKR1
PKR2
PKR1+2
myoMyo
myoVel
Viability (RLU)

1940 **Figure 5: A varied structural variation landscape across 9 nearctic *Myotis* species. A)** Synteny
1941 between *Myotis* species on chromosome V15, showing syntenic regions (grey), inversions (orange),
1942 translocations (green), and duplications (blue). Regions with high proportions of telomeric repeats were
1943 masked prior to alignment. **B)** Distribution of transposable elements and segmental duplications (red
1944 heatmap) in mMyoVel1. Pie chart indicates overall genome proportions of TEs; histogram represents the
1945 size distribution of segmental duplications genome-wide. **C)** CAFE results among our Nearctic *Myotis*
1946 relative to single-copy human orthologs. Phylogeny is colored by the estimated birth/death rate (λ) for all
1947 genes examined. Bar plot indicates the cumulative number of significant gain and loss events for each
1948 species. **D)** Per-genome copy numbers of all genes with over 6 copies in any Nearctic *Myotis* genome.
1949 Genes are classified into 5 categories (cancer, aging, immunity, VIP, translation, and "Other") based on
1950 literature reviews on PubMed. **E)** Copy number estimates of *FBXO31* across 536 mammalian genomes
1951 identified using Reciprocal Best-Hit BLAT. **F**) Gene-tree reconciliation of FBXO31 across mammals
1952 generated using GeneRax.

1953 **Figure 6: Evolutionary history and function of an actively segregating copy number polymorphism**
1954 **of *PKR* in *Myotis*. A)** Structural comparison of the main PKR haplotypes in two species. Orthologous
1955 regions between the two haplotypes are indicated by grey bands, while syntenic duplications are indicated
1956 in green. Exons are annotated with black marks. **B)** Cartoon of the PKR locus in the two phased haplotype
1957 assemblies of each species. While *PKR2* is present across all haplotypes, *PKR1* and *PKR copy 3* are
1958 polymorphic within and across species. Each number indicates the number of exons per gene. **C)**
1959 Reconciled gene tree for *PKRs* across all haplotypes and species shown in **B.** Haplotype corresponding to
1960 the reference (A) and alternate (B) haplotype for each species are represented by upper- and lower-
1961 diagonal triangles, respectively. **D)** Co-immunoprecipitation (IP) of PKR-KO HeLa cells transfected with *M.*
1962 *myotis* HA-PKR1 and either *M. myotis* myc-PKR1, *M. myotis* myc-PKR2 or a myc-empty vector control.
1963 Proteins were pulled down with anti-myc beads and lysates from 5% input or IP samples were run on a
1964 western blot and stained for HA and myc. Representative of 3 independent experiments. **E-G)** Effect of
1965 *Myotis* PKR copy numbers: **E)** On luciferase translation, measured in Relative Light Units (RLU) and
1966 normalized to the empty pSG5 control; xo-expression of PKR1 and PKR2 has an additive effect on cell
1967 translation shutdown (no synergy or dominant negative effects). Human SAMD9L-GoF is a positive control
1968 of translation inhibition[249]. **F)** On viral VSV infectivity, measured via flow cytometry as VSV-GFP-positive
1969 cells normalized to the control. Although all conditions restrict VSV, the expression of both PKR1 and PKR2
1970 is not beneficial against VSV. ISG20 is a positive control of VSV-GFP restriction[241]. **G)** On cell viability,
1971 normalized to the control. While no effect was observed at a low total dose of PKRs, at higher doses PKRs
1972 significantly reduce cell viability. Etoposide treatments are positive controls of cell death. For **E-G**, error
1973 bars indicate the means ± SEM for at least three independent experiments. Statistics, unpaired t-test of
1974 each condition versus control.